Solid State Material Systems for Light Emission and Light Detection

Ivan-Christophe Robin

Université Joseph Fourier – Grenoble I

HABILITATION A DIRIGER DES RECHERCHES

présentée par

Ivan-Christophe ROBIN

pour obtenir le titre de

HDR

Discipline: Physique

Solid State Material Systems for Light Emission and Light Detection

soutenue publiquement le lundi 6 juin 2011

Composition du jury:

Président :	**Henri MARIETTE**
Rapporteurs :	**Henning RICHERT**
	Chantal FONTAINE
	Jean-Yves DUBOZ
Membres du Jury :	**Yong ZHANG**
	Alain LUSSON

Laboratoire Matériaux et Substrats «Service Technologies et Moyens»
Département Optronique – CEA, LETI - MINATEC

Acknowledgments

During my previous work I came to work with many supportive people. I cannot name everyone here but I would still like to thank all my previous coworkers.

I especially would like to thank the people of Thomas Tiedje's group at UBC (and Thomas Tiedje himself of course) who welcomed me in Vancouver when I came to do my first post-doc. I would also like to thank the Carnot Eclairage team in which I had a very motivating experience. I especially thank Guy Feuillet who selected me to work on ZnO spectroscopy after I came back to France. I really enjoyed working with him and it is still a pleasure to interact with him on a large variety of projects. I would also like to thank the people of Alain Million's laboratory (and Alain Million himself also, of course) who welcomed me when I was hired on a permanent position, the MBE HgCdTe growers and especially Philippe Duvaut for his patience and cheerfulness when we started the Epineat machine.

Finally I would like to sincerely thank all the members of the jury for the time and effort they spent to evaluate my work.

Contents

Introduction

During my early research projects, I worked on a large variety of materials for light emission and detection. I studied semiconductor materials ranging from very small band gap semi- conductors for infrared (IR) detectors to wide band gap semiconductors for ultra violet (UV) emission and oxides for laser fabrication. I had the opportunity to tackle the growth and characterization aspects of those materials and I always studied the links between the growth procedure and the optical properties. Time resolved photoluminescence on an as- sembly of CdSe/ZnSe quantum dots allowed me to study the effect of the growth procedures on the confinement properties in the quantum dots [1]. Time resolved photoluminescence on single quantum dots placed in micropillars showed the exaltation of the spontaneous emission for quantum dots coupled with microcavity modes [2]. Time resolved photoluminescence on single quantum dots placed in micropillars showed the exaltation of the spontaneous emission for quantum dots coupled with microcavity modes [3]. In the case of ZnO nanowires, I could evidence the low density of non radiative defects using optical characterizations [4]. In particular it is seen that the substrate on which the nanowires are grown have a strong impact on the radiative and non radiative decay times. Recently infrared photoluminescence studies allowed us to find the optical signatures of arsenic site transfer during post-growth activation annealing of HgCdTe epi- layers [5] and we could visualize the double acceptor levels of Hg vacancies [6].

In the first chapter I will present my early work from the point of view of the relations between the growth procedures and the optical properties of the material systems. I will especially point out the informations that can be gained by the optical studies as well as their limitations: the optical studies have to be combined with other characterization techniques and have to be interpreted carefully as they often don't give quantitative information (like the carrier concentration in doped layers for instance).

In the second chapter, I will show how I plan to use the knowledge I gained in material systems to lead new projects. My main project is to circumvent the problems linked to the p-type doping of wide band gap semiconductors. This project, based on field effect hole injection addresses a major challenge which is the fabrication of efficient deep UV emitters.

Chapter 1

From Single Photon Emitters to Solid State Lasers, From Ultra-Violet Emission to Infra-Red Detection (My previous Work)

During my carrier I became interested in many different material systems. I did my PhD on CdSe/ZnSe quantum dots for single photon emitters, then I worked on Nd:Y_2O_3 layers for solid state lasers in Vancouver. When I came back to France I was is charge of ZnO material characterization in a project on the fabrication of ultra-violet (UV) light emitting diodes (LEDs) and I was then hired on a permanent position to work on the growth of HgCdTe layers for the fabrication of infra-red detectors. All of those material systems have in common that they are used for light emission or light detection.

As I will show I came to study many different aspects of those material systems. I did a lot of work concerning the growth of those materials and the optical characterization of those materials, which allowed me to understand the links between the growth procedures and the physical optical properties. I will try to outline in this chapter the relations between the growth procedures and the optical properties, what information can give the optical characterization and how to couple it with other techniques to understand the physical properties of a material system.

1.1 CdSe/ZnSe quantum dots for single photon emitters

In this section, I will do a very brief summary of my PhD work, that I did in the Nanophysics and Semiconductors group of the CEA Grenoble in France.

My research project during my PhD was to grow CdSe/ZnSe quantum dots (QDs) and to place them into microcavities in order to control their spontaneous emission. Indeed II-VI self assembled QDs as CdSe/ZnSe QDs are a promising system for single photon emission in the blue-green range [2, 7, 8, 9].

During my PhD work between 2002 and 2005, I developed a new growth process of CdSe/ZnSe QDs using amorphous selenium [10, 11, 12]. I studied their optical properties by time integrated and time resolved photoluminescence (PL) [1, 10] and placed them into microcavities to control their spontaneous emission [2, 13].

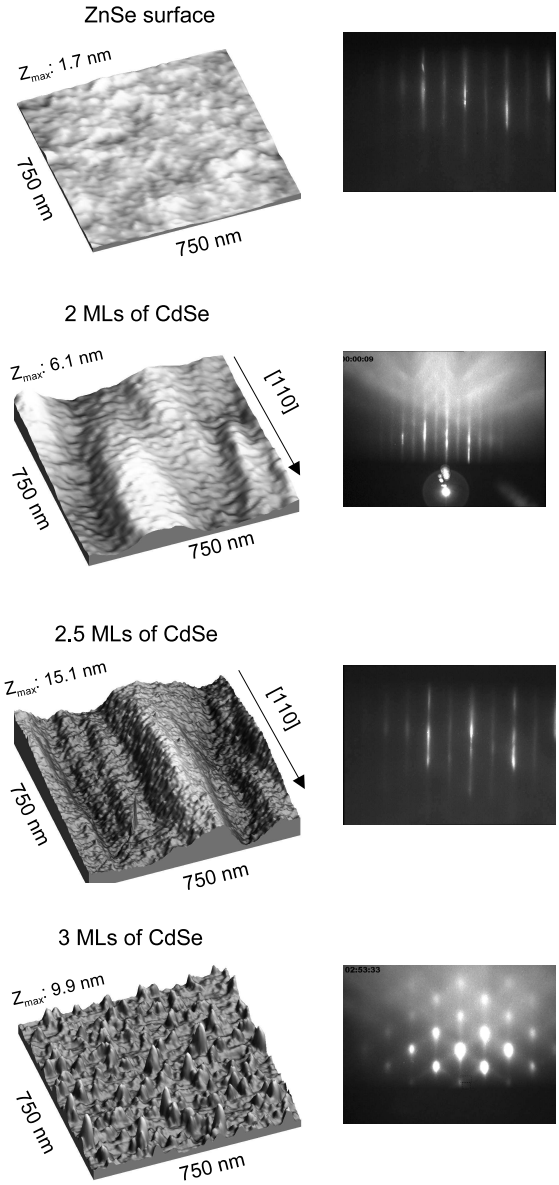

Figure 1.1: Ex-situ AFM images after amorphous selenium desorption for three different thicknesses of CdSe as well as for the initial ZnSe surface. The same z scale along the growth axis has been chosen for the four images. The right column shows the corresponding RHEED patterns of the surfaces.

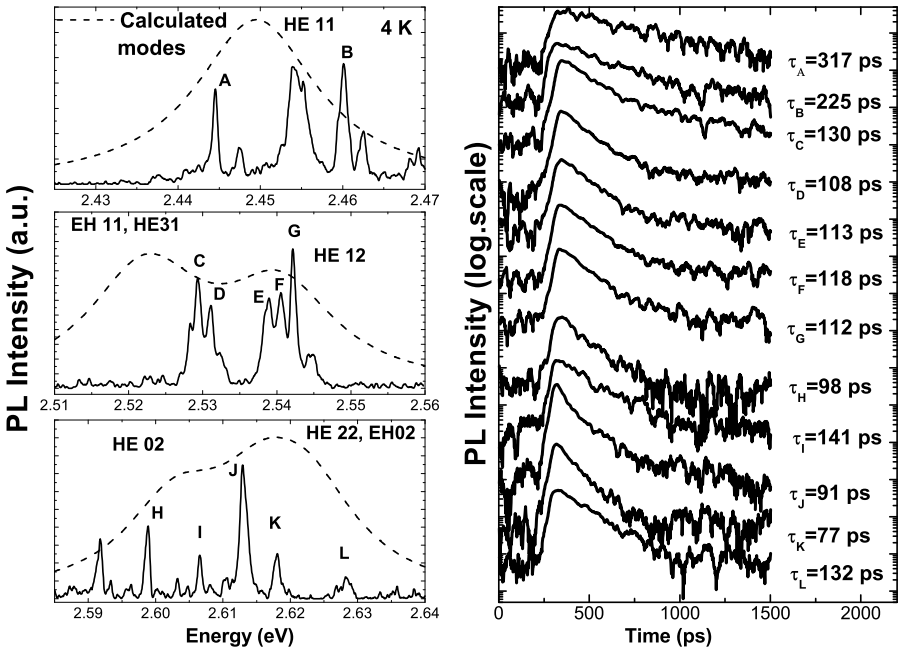

Figure 1.2: PL spectra of isolated QDs placed in a hybrid microcavity (left column) with the calculated positions of the micocavity modes [2]. The right column presents the measurements of the PL decay times for labeled emissions on sigle QDs.

In Figure 1.1, the effect of the change of surface energy via amorphous selenium deposition is seen for different thicknesses of strained CdSe layers on ZnSe. Indeed, AFM images after amorphous selenium desorption for three different thicknesses of CdSe as well as for the initial ZnSe surface on which the CdSe was deposited are shown(cf. [11]). The Reflective high energy electron diffraction (RHEED) patterns are also shown.

The amorphous selenium desorption process described in refecences [10, 11, 12] does not change the surface morphology of the ZnSe surface. The amorphous selenium desorption for thicknesses of 2 ML and 2.5 ML f CdSe lead to strong undulations on the surface. The RHEED patterns indicate a 2D surface, due to the presence of large terraces on the surface in comparison to the scale probed by the RHEED electron beam. The amorphous selenium desorption deposition on a 3 ML thick CdSe layer strained on ZnSe leads to a drastically different surface morphology: the formation of small circular islands clearly occurs on the surface. This shows the effect of the change of surface energy (here via amorphous selenium deposition) on 2D-3D transition.

The optical properties of those QDs using the amorphous selenium desorption process were studied by time integrated and time resolved photoluminescence (PL) [1, 10]. Then they were placed into microcavities to control their spontaneous emission [2, 13]. Time resolved photoluminescence allowed us to evidence an exaltation of the spontaneous emission, i.e. the Purcell effect, for QDs coupled with the cavity modes . The best results were obtained when the QDs were placed into a hybrid microcavity as described in reference [2].

The PL decay time τ for a series of twelve single QDs located in the same hybrid microcavity processed into a 1.1 μm diameter pillar were measured at 4K and under very low excitation condition ($\approx 1W/cm^2$). We observed the emission of single QDs from 2.445 eV to 2.62 eV and a large range of PL decay times from 75 ps to 307 ps were measured for

those QDs (Fig. 1.2).

The shortening of the PL decay times compared to the QDs outside the cavity were explained calculating the Purcell factors of the modes to which the QDs emissions were coupled [2]. At most, a clear shortening of the PL decay time, by a factor of 3.3 was obtained. As is developed in reference [2], the PL decay time changes are well explained by the calculation of the Purcell factors of the different modes involved in the emission process. This was the first evidence of the Purcell effect with II-VI QDs. In this case, the optical studies allowed to evidence the Purcell effect as well as a deep understanding of the coupling of the QDs emission with the cavity modes.

1.2 MBE grown Nd:Y_2O_3 films for solid state lasers

After my PhD, I moved to Vancouver Canada to work on the growth by MBE of oxide films at the MBE Lab of the University of British Columbia. This work was partly financed by Zecotek Medical Systems, a local company commercializing solid state lasers. This company wanted to explore the possibility of fabricating planar waveguide lasers (PWL) by MBE.

PWLs have several advantages over conventional bulk designs. PWLs offer a better overlap between the output laser light and the pump beam within the active layer. The geometry allows simpler heat removal because of a higher surface-area to volume ratio.

PWLs have been fabricated by several methods, including liquid phase epitaxy (LPE) [14] and pulsed laser deposition (PLD) [15]. PWLs grown by MBE should yield lower densities of thermodynamic defects due to lower growth temperatures compared with bulk crystals grown from a melt. In addition MBE presents a convenient way of controlling the rare earth dopant concentration simply by changing the flux ratios.

In parallel, yttrium oxide (Y_2O_3) had been investigated for a long time as an active host material for lanthanide ions due to its favorable properties [16]. Among these are its refractory nature, and optical clarity over a broad spectral region. In addition, the thermal conductivity of Y_2O_3 is about two times larger than that of yttrium aluminum garnet (YAG), and the thermal expansion coefficient is very similar [17]. It is very difficult to grow large-size high-quality Y_2O_3 single crystals by conventional methods because of the very high melting temperature ($\approx 2430^oC$) of Y_2O_3 and structural phase transitions at $\approx 2280^oC$. Instead, Lu *et al*. have pursued Nd^{3+}:Y_2O_3 in ceramic laser form [18]. MBE growth of Y_2O_3 thin films overcomes those difficulties because of the lower growth temperatures. In addition, unlike YAG, Y_2O_3 is a binary alloy, and thus is a simpler candidate for MBE growth.

Before, Y_2O_3 had been grown on silicon substrates using different approaches such as ion cluster beam [19] and electron beam evaporation [20, 21, 22]. In those works, the motivation was to utilize the high permittivity of Y_2O_3 (κ=18) as a dielectric in silicon integrated circuits. The growth of Y_2O_3 on silicon substrates is also interesting for the fabrication of PWLs because it offers the possibility of integration into silicon chips.

When I arrived in the group, a VG V80 MBE machine had just been bought to grow oxides. I did the first growths with this machine. I mainly grew Neodymium doped yttrium oxide. This material had almost never been grown before by MBE. Thus, during my one year post-doc position I explored different growth conditions of Y_2O_3 on Si(001) and sapphire(0001) substrates. Using sapphire as a substrate is useful for PWLs due to its lower refractive index ($n_{Al_2O_3}\approx$1.77 and $n_{Y_2O_3}\approx$ 1.85 at 1μm). In addition, our oxide MBE system was capable of fabricating symmetric waveguides by growing a sapphire cladding

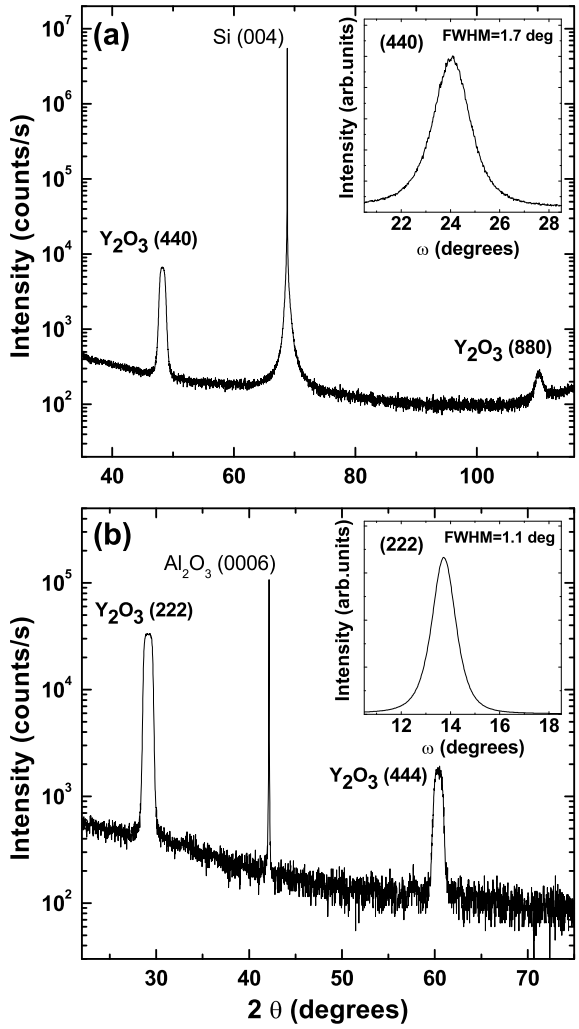

Figure 1.3: XRD patterns of Y_2O_3 films grown (a) on a Si(001) substrate at 800^{o}C and (b) on sapphire(0001) substrate at 1100^{o}C. The insets show omega scans of the (440) peak for the sample grown on silicon and the (222) peak of the sample grown on sapphire.

layer after the growth of Nd:Y_2O_3.

To grow Y_2O_3, we used an yttrium metal effusion cell heated between 1600^{o}C and 1750^{o}C to obtain yttrium fluxes between 5 X 10^{-8} and 5 X 10^{-7} Torr, measured with an ion gauge placed in front of the substrate. During growth, oxygen is introduced into the chamber through a leak valve, and the oxygen flux is inferred from the background pressure in the growth chamber. The oxygen partial pressure during Y_2O_3 growth is chosen to be typically equal to ten times the yttrium flux. The Y_2O_3 growth rate as measured with a quartz crystal is typically between 100 and 800 nm/h. To dope the Y_2O_3 with neodymium, a neodymium cell heated to about 1000^{o}C is used to obtain a neodymium flux of a few percent of the yttrium flux. We studied the influence of the growth temperature, the oxygen/yttrium flux ratio and Y/Nd flux ratio on the structural and photoluminescence (PL) properties of the neodymium doped samples.

For the growth on silicon substrates, the substrates were HF deoxidized in a clean environment before being introduced into the growth chamber and heated to 900^{o}C to

obtain a clean Si surface free of oxide. We deposited about 1 nm of yttrium metal before the growth of Y_2O_3 to avoid the reoxidation of the HF cleaned substrate and the formation of a SiO_2 interfacial layer. After the initial Y layer, the yttrium cell was closed and a partial oxygen pressure typically of 2.5 X 10^{-6} Torr was introduced in the growth chamber. The Y_2O_3 growth was started by reopening the yttrium cell when the pressure into the growth chamber was stabilized.

The growth temperature was controlled by a thermocouple and checked by a pyrometer. Under these conditions, single crystal orientation along the growth axis of Y_2O_3 was found for growth temperatures between 350 and 800^{o}C. For a growth temperature of 350^{o}C the heteroepitaxial relation $Y_2O_3(111) \parallel Si(001)$ was found. For a growth temperature of 650^{o}C the $Y_2O_3(001) \parallel Si(001)$ is the main growth direction of Y_2O_3. Figure 1.3(a) presents the X-ray diffraction (XRD) pattern of a Y_2O_3 sample grown at 800^{o}C. It shows the $Y_2O_3(110) \parallel Si(001)$ heteroepitaxial relation: the two strong peaks correspond to $Y_2O_3(440)$ and (880). This growth temperature gives the best structural quality in terms of the width of the Y_2O_3 peaks in rocking curve measurements. This width decreases with increasing Y_2O_3 layer thickness. In the inset of figure 1.3(a), we show the rocking curve on the (440) peak of a 60 nm thick Y_2O_3 sample grown at 800^{o}C. The width of 1.7 degrees is one of the best values reported in the literature [21, 22]. For a growth temperature of 1000^{o}C the XRD pattern does not present any Y_2O_3 peaks but only YSi_2 peaks. Those peaks were also observed at lower temperature, when an oxygen/yttrium flux ratio smaller than 10 was used at growth temperatures between 350 and 800^{o}C. They were also observed by Dimoulas *et al*. for a sample grown at 610^{o}C [20]. In our case, the growth of a thin yttrium metal layer before the Y_2O_3 growth seems to avoid the formation of YSi_2 up to a growth temperature of 800^{o}C. However, Cho *et al*. [19] also observed YSi_2 peaks when starting the growth with yttrium metal at 700^{o}C. In our growth procedure, we expose the surface to oxygen before starting the growth of Y_2O_3. During this step, the yttrium silicide is probably oxidized into Y_2O_3.

Figure 1.3(b) presents the θ-2θ XRD pattern of a Y_2O_3 sample grown on sapphire(0001) at 1100^{o}C. We investigated growth temperatures between 450 and 1100^0C for growths on sapphire. The heteroepitaxial relation found was always $Y_2O_3(111) \| Al_2O_3(0001)$. The smallest width of Y_2O_3 peaks in rocking curve measurements was found for growth temperatures of 1100^0C. Rocking curves on the (222) peak of Y_2O_3 exhibit widths as small as 1.1 degrees (inset of figure Figure 1.3(b)).

To study the in-plane orientation, we measured x-ray diffraction from off-axis peaks of the Y_2O_3 layer and the substrate. Figure 1.4(a) presents a Φ scan for the (840) peak of Y_2O_3 for a sample grown on Si(001). Φ is the rotation angle around the substrate surface normal. Four peaks separated by 90^o are visible on a 360^o Φ range although the (840) peak has 2-fold symmetry. The appearance of four peaks shows the existence of twin domains rotated by 90^o around the Si(001) azimuth. The existence of twin domains for Y_2O_3 films grown on silicon was also found by other groups [19, 20]. The Φ position of the (840) Y_2O_3 off-axis peak for one of the domains is aligned with the (311) peak of the silicon substrate within 4^o. From the projection of the (840) peak on the (110) plane for the Y_2O_3 and the projection of the (311) peak on the (001) plane for the silicon we conclude that the [1 $\bar{1}$ 0] in-plane direction of Y_2O_3 is parallel to the [110] direction of silicon within 4^o. For the other domain, the in-plane orientation is $[001]Y_2O_3//[110]Si$.

Figure 1.4(b) shows a Φ scan for the (662) peak of Y_2O_3 for a sample grown on sapphire(0001). A small mis alignment between the (111) direction of the crystal and the Φ

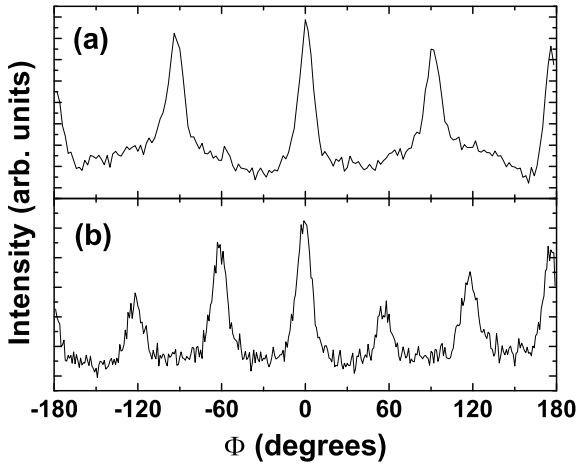

Figure 1.4: Φ scans of (a) the Y_2O_3 (840) peak and (b) (662) peak for samples grown on Si(001) and sapphire(0001) respectively.

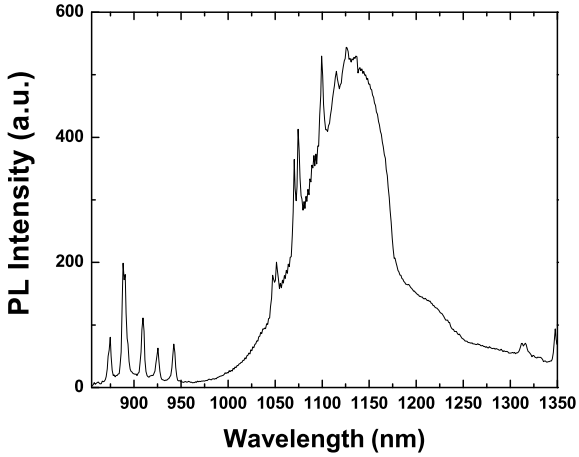

Figure 1.5: PL spectrum of a 260 nm thick 0.7% Nd:Y_2O_3 sample grown on Si (001).

rotation axis causes a variation in relative peak intensity in figure 1.4(b). Six peaks separated by 60^o are visible on a 360^o range although the (662) peak has a 3-fold symmetry. This shows the existence of twin domains rotated by 60^o around the sapphire(0001) azimuth. The Φ position of the (662) Y_2O_3 peak for one of the domains is aligned with the (1 0 $\bar{1}$ 10) peak of sapphire. From the projections of the (662) peak on the (111) plane for Y_2O_3 and of the (1 0 $\bar{1}$ 10) peak on the (0001) plane for sapphire we determined that the [1 1 $\bar{2}$] in-plane direction of Y_2O_3 is parallel to the [1 0 $\bar{1}$ 0]. For the other domain [1 1 $\bar{2}$]Y_2O_3//[1 $\bar{1}$ 0 0]sapphire.

Strong PL at room temperature was measured for neodymium doped samples grown on Si(001) and on sapphire(0001). A large oxygen/yttrium flux ratio (of about 10) is a precondition for strong luminescence.

In figure 1.5 the PL spectrum of a 260 nm thick 0.7% Nd:Y_2O_3 sample grown on Si (001) is shown. The PL excitation source is a semiconductor laser diode at 808 nm. The excitation density is about 2W/cm^2. Emission is analysed by a 15 cm focal length monochromator with a 600 lines/mm grating. This sample was grown with an oxygen pressure/yttrium flux

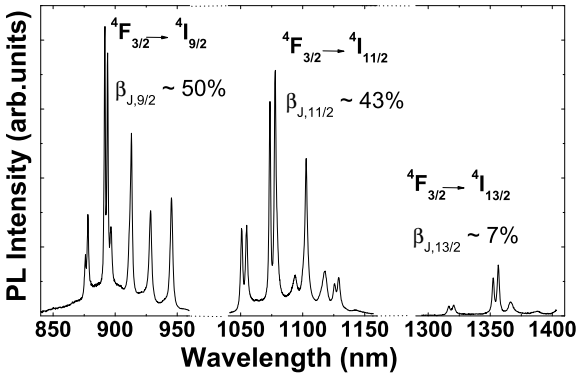

Figure 1.6: PL of a 1.35 at.% Nd:Y_2O_3 sample grown on sapphire(0001)

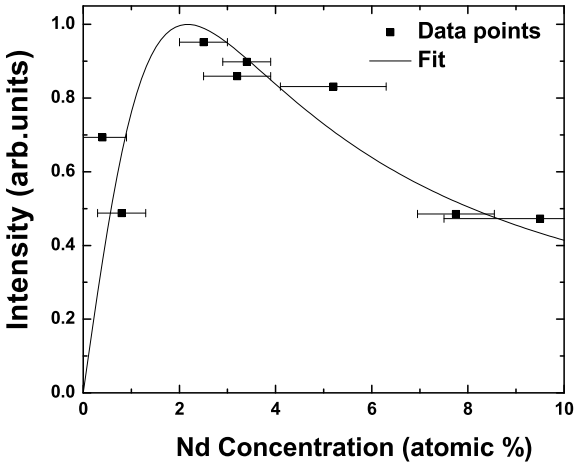

Figure 1.7: PL intensity of the $^4F_{3/2} \rightarrow {}^4I_{11/2}$ transitions for varying concentrations of Nd:Y_2O_3 grown on sapphire(0001).

ratio of 10. In the PL spectrum, the Neodymium emission lines are superimposed with the band edge emission of silicon. The band edge emission intensity of silicon is similar to the one measured on silicon substrates and on undoped Y_2O_3 layers grown on silicon in the same growth conditions. This shows that Y_2O_3 grown in these growth conditions is transparent. The intensity of the Nd lines increases when increasing the Nd:Y_2O_3 thickness. As will be shown later the maximum PL intensity is obtained for a Nd concentration of about 2%. For samples grown with an oxygen pressure/yttrium flux ratio smaller than 10, the band edge emission of silcon is not visible anymore and the PL intensity of the neodymium lines is much weaker. This shows that the Y_2O_3 films are not transparent anymore which could be due to the existence of a YSi_2 layer (YSi_2 lines are observed in the XRD spectrum when the oxygen pressure/yttrium flux ratio is smaller than 10).

Figure 1.5 shows the PL in three spectral regions of a 2.2μm thick 1.35 at.% Nd:Y_2O_3 sample grown on sapphire(0001). The three spectral regions correspond to the $^4F_{3/2} \rightarrow {}^4I_{9/2}$, $^4F_{3/2} \rightarrow {}^4I_{11/2}$ and $^4F_{3/2} \rightarrow {}^4I_{13/2}$ channels of Neodymium. The position of the emission lines are very similar to the ones reported for Nd:Y_2O_3 ceramic samples [18]. We calculated the branching ratio of each deexcitation channel. The strongest transitions correspond to the $^4F_{3/2} \rightarrow {}^4I_{9/2}$ channel as reported in litterature [23].

In Figure 1.7, the integrated PL intensity of the $^4F_{3/2} \rightarrow ^4I_{11/2}$ transitions *vs* Nd concentration is shown. For this study, we grew eight 430 nm thick samples of Nd:Y_2O_3 on sapphire using similar growth conditions with the exception of a varying Nd/Y flux ratio. The Nd concentration was deduced from this flux ratio assuming complete Nd incorporation. At low Nd concentrations the PL intensity increases with concentration to a peak value around 2 at.%, but decreases with further increases in concentration. This quenching effect is due to cross relaxation interactions between Nd ions. Assuming an N^2 dependence on the non-radiative relaxation rate [24], we can now express the fluorescence efficiency as $1/(1 + AN^2)$ where N is the Nd concentration. Factoring in absorption, the total PL emission can be fitted to the form $BN/(1 + AN^2)$, where A and B are fitting parameters. Using this model, we find an optimal dopant concentration of 2 at.%, similar to the concentration for maximum PL intensity in Nd:YAG [25].

Those results show that we were able to grow high quality Nd:Y_2O_3 films during this one year post-doc. Those resuls also show the high potentiality of Nd:Y_2O_3 for the fabrication of planar waveguide laser structures. This work led to a patent publication [26]. This work was continued when I left the laboratory [3, 27, 28, 29]. Neodymium-doped yttrium aluminum perovskite was grown [27]. The quality of the Nd:Y2O3 films was improved [29] by growing on R-plane sapphire. X-ray peaks as low as 7 arc sec could then be measured. Then optical wave propagation in Nd:Y2O3 films grown on R-plane sapphire substrates has been studied [28].

1.3 Optical properties of ZnO nanowires and 2D layers

After my experience in Canada I came back in France in december 2006 at the CEA-Grenoble to work on ZnO material optical properties. A 15 M€ Carnot project involving 20 researchers had just started to study the possibility of developing a French industrial sector in the field of solid state lighting. It had been decided to study the possibility of using ZnO material and Semiconductor nanowires (NWs) to fabricate Light Emitting Diodes (LEDs). Effectively, ZnO growth and properties had been investigated due to its potential for the realization of novel light emitting devices [30]. One of the reasons for considering ZnO to be a promising material for light emitters in the ultraviolet (UV) spectral region is the large exciton binding energy of $\approx$ 60 meV which is larger than the thermal energy $k_BT \approx 25$ meV at room temperature. However one has to keep in mind that the exciton-LO phonon coupling constant in ZnO is nearly four times stronger than that of GaN and about eight times stronger than the one of ZnSe [31]. As it will be seen, at room temperature the main recombination processes in ZnO involves the emission of one or more phonons. This represents a crucial point which has to be taken into account when discussing potential applications of ZnO for optoelectronic devices.

In order to fully take advantage of the exciton strength one has to master the growth of defect-free material. In this perspective, ZnO nanowires (NWs) growth is interesting because strain can be efficiently relieved by elastic relaxation at the free lateral surfaces of the NWs rather than through plastic relaxation. During this post-doc I intensively studied ZnO NWs optical properties and time-resolved PL measurements allowed to show the interest of this material system for optoelectronic devices as a very low density of non-radiative defects could be evidenced in our NWs. The optical properties of ZnO NWs grown on sapphire were compared to the ones of NWs grown on p-type GaN. The growth on GaN seems to present an advantage and increases the radiative quantum efficiency. ZnO 2D layers grown

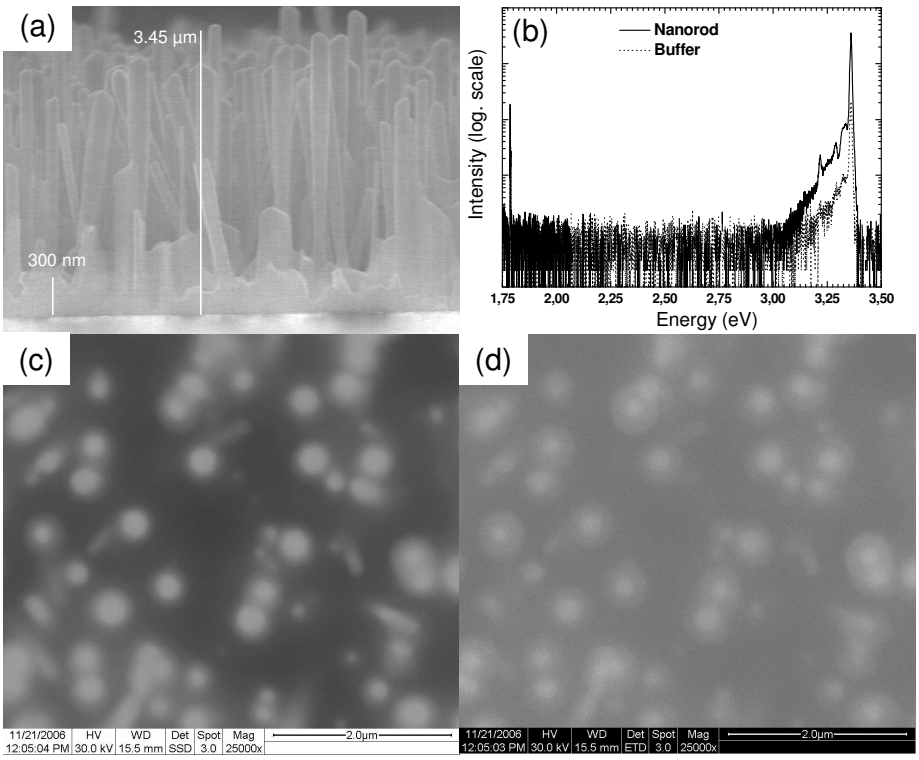

Figure 1.8: (a) SEM image of the ZnO NW arrays. (b) Comparison of two CL spectra obtained at 4K by focusing the e-beam on a single NW or on the underlying ZnO wetting layer. (c) Low temperature (4K) CL image obtained using the emission at 3.36 eV (corresponding to the maximum intensity of luminescence) (d) SEM image of the same area than the CL image shown in figure (c).

by metal organic vapor phase epitaxy (MOVPE) or molecular beam epitaxy (MBE) on bulk substrates were also studied. Indeed homoepitaxial growth allows limiting the density of dislocations. It is seen in this study that the growth conditions can also be optimized to lower the residual doping level in homoepitaxially grown ZnO layers.

1.3.1 ZnO nanowires grown on sapphire substrates

In most published articles a green luminescence band corresponding to deep level defects is observed in as-grown NWs [32, 33, 34, 35]. In this section I will present cathodoluminescence (CL), time integrated and time resolved photoluminescence (PL) temperature dependence measurements done on ZnO NWs grown by metal organic vapor phase epitaxy (MOVPE). Those measurements evidence that we were able to grow ZnO NWs with very low density of defects and nonradiative channels.

The ZnO NWs were grown by MOVPE on (0001) Al_2O_3 substrates. The typical growth temperature is 800^oC and the oxygen precursor is N_2O. Under these growth conditions the ZnO layer consists of a 300 nm thick irregular two dimensional (2D) layer above which 3.5 μm long NWs with a diameter of 150 nm are obtained (cf. figure 1.8(a)).

CL measurements are carried out using a scanning electron microscope (SEM) system with a variable temperature (4K - 300K) sample holder. The electrons energy is 30 kV and the spot size of about 10 nm. On the detection side, a secondary electron detector is used

to image the surface and the luminescence is collected by a parabolic mirror and dispersed with a 0.55 m monochromator equipped with a 600 mm^{-1} grating. A CCD camera is used to measure spectra or a single channel photomultiplier tube to obtain CL images. Because of the relatively low density of the NWs ($\approx 2.10^8/cm^2$) under the excitation conditions, CL allows a very local characterization of the sample. A single NW or the 2D layer can be selectively studied. In figure 1.8(b) two CL spectra obtained at 4K for a single NW and for the underlying 2D layer are compared. In both, 2D layer and the NW, CL emission is only observed in the UV band edge (BE) spectral region and the green luminescence band which is commonly measured at low temperature in as-grown bulk crystals [36, 37], thin films [38, 39] or NWs [32, 33, 34] is not observed here. This result indicates that the density of extended defects, oxygen and zinc vacancies is very low.

The main contribution to the BE emission is the neutral donor bound exciton (D^oX) emission at 3.36 eV probably due to aluminum dopants coming from the sapphire substrate. When focusing the electron beam on a single NW, the measured intensity is about four times larger than when focusing on the 2D layer. The CL image (figure 1.8(c)) obtained by setting the detector at 3.36 eV confirms a stronger CL intensity for all NWs. This effect is not due to a difference of Al concentration because a stronger intensity for the NWs is also found at room temperature where the excitons are no more localized on donor impurities (see figure 1.9). It is neither due to a better light extraction: the stronger intensity for the NWs is also observed when the NWs are detached and dispersed on the 2D layer and when the luminescence is collected perpendicularly to the NWs axis. So the stronger luminescence for the NWs is consistent with a better crystalline quality of the NWs compared to the 2D layer possibly due to strain relaxation through surface deformation.

In figure 1.9(a), we show the PL temperature dependence of the BE emission, studied using a frequency-doubled 244 nm *cw* Ar laser coupled with a 0.55 m monochromator equipped with a 600 mm^{-1} grating. The incidence angle of the laser beam with the surface is about 45^o. Because of the NWs density ($\approx 2.10^8/cm^2$) and their length to diameter ratio(≈ 35), the NWs (and not the 2D layer) are selectively excited. At low temperature the D^oX exciton at 3.36 eV and its phonon replica dominate the spectrum and the free exciton (FX) is not observed, probably because of a high aluminum dopant concentration coming from the sapphire substrate ($\geq 10^{18}$, obtained by Hall measurement on the 2D layer using Van der Pauw geometry). The full width at half maximum (FWHM) of the D^oX emission is 1 meV, showing the high structural quality of the material. The A free exciton (FX_A) emission, together with its phonon replica appear when increasing temperature above 90K. At room temperature the first phonon replica of the FX dominates the spectrum [36]. Figure 1.9(b) shows the BE PL intensity integrated over the whole BE emission *vs* the inverse of temperature between 4K and 90K. In this temperature range the band edge emission is dominated by the D^oX exciton. An activation energy of 13 meV is found, corresponding to the localization energy of the D^oX exciton (see reference [40]). In this temperature range the decrease of the PL intensity with temperature is due to the detrapping of the D^oX exciton, in agreement with the modification of the PL spectrum observed in figure 1.9(a).

Time resolved PL was measured using a frequency-tripled sapphire:Ti 266 nm laser emitting at 266nm with a 150fs pulse width and a 80 MHz repetition rate. The angle of incidence of the laser beam is as previously about 45^o. In this setup the luminescence signal is dispersed by a 0.3 m monochromator equipped with a 300 mm^{-1} grating and time resolved by a streak camera. The spectral resolution is about 1 meV and the time resolution is 5 ps. The measurements were done under weak excitation conditions (3 W/cm^2).

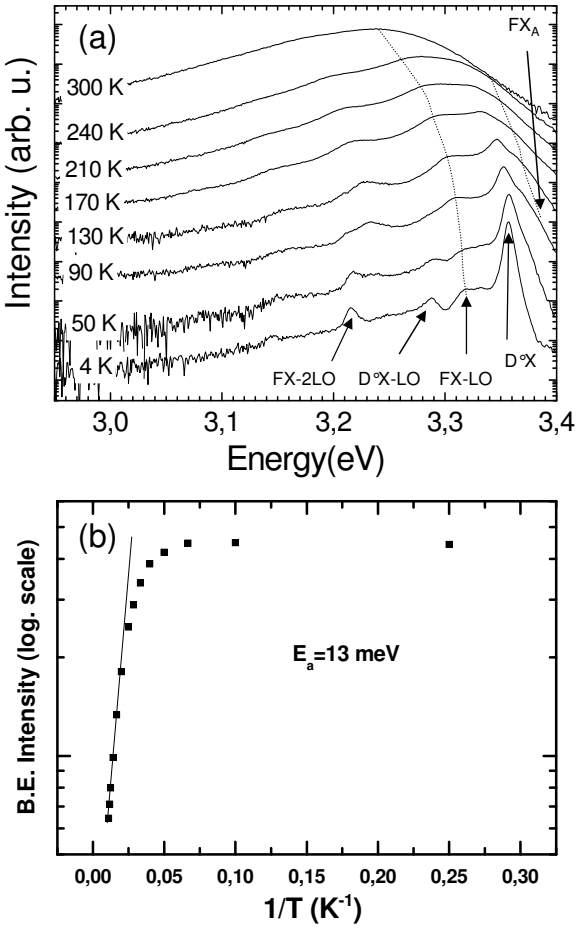

Figure 1.9: (a) PL spectra of ZnO NWs at selected temperatures. (b) BE PL intensity *vs* the inverse of temperature between 4K and 100K.

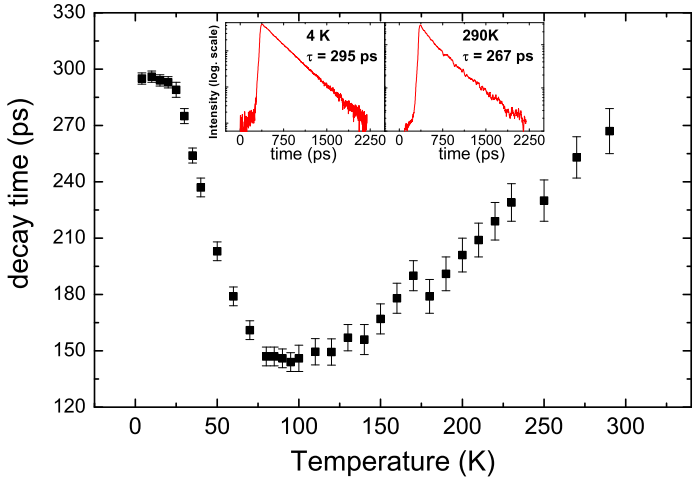

Figure 1.10: PL decay times versus temperature. The insets show the PL decay at 4 K and 290 K.

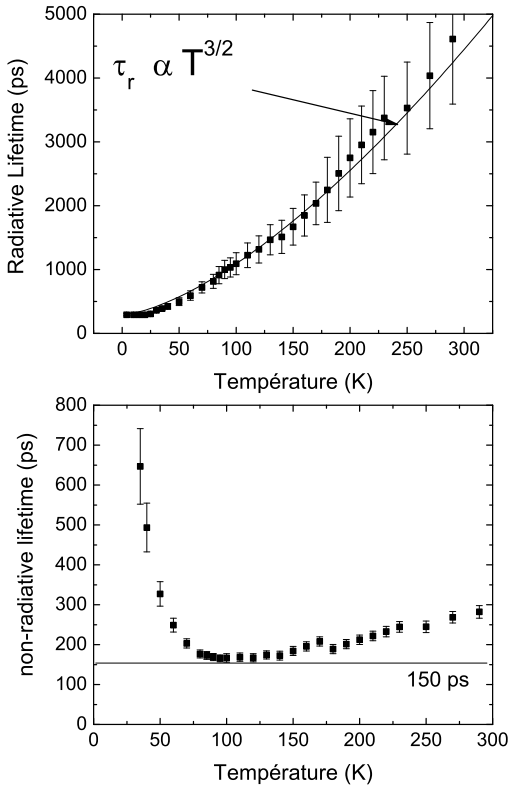

Figure 1.11: Radiative (top) and non-radiative (bottom) lifetimes of the ZnO NWs.

The decay time temperature dependence is presented in figure 1.10. At a given temperature, the luminescence decay after an excitation pulse is monoexponential (see insets of figure 1.10b)) and constant over the whole BE spectral range. A monoexponential decay is a signature of an excitonic behavior up to room temperature (an electron-hole pair plasma would follow a bimolecular law with a non exponential decay). A constant decay time over the whole spectral range in particular at intermediate temperatures for which the FX_A and the D^oX contributions are equivalent means that the system is thermalized and that an equilibrium between the discreet donor states and the exciton band is reached. It is supposed that the capture processes are much faster than the emission processes over the whole temperature range.

At 4 K a decay time of 295 ps is measured. This decay time is constant up to 30 K because the exciton is bound to a discrete donor state and the measured decay time is the D^oX life time. When increasing the temperature from 40 K to 100 K, the PL decay time decreases. From 40K, the D^oX exciton is thermally activated into a FX and non-radiative channels are activated. However, unlike in other systems as GaAs/GaAlAs quantum wells [41] or CdSe/ZnSe quantum dots [1], when increasing the temperature further, the decay time does not continue to decrease but even increases again.

To quantitatively understand this behavior, the radiative τ_r and the non-radiative τ_{nr} decay times from the data of figure 1.10 are calculated [41] (see figure 1.11). Noting τ and I the measured decay time and intensity, $1/\tau = 1/\tau_r + 1/\tau_{nr}$ and $I = I_0 \frac{1/\tau_r}{1/\tau_r + 1/\tau_{nr}}$ where

I_0 is the low temperature intensity, assuming that at 4K, the quantum efficiency is 1 so the non radiative decay time τ_{nr} is infinite. Note that this calculation makes sense over the whole temperature range because at a given temperature, the constant decay time over the whole spectral range shows that a thermal equilibrium between the discreet donor states and the exciton band is reached. Using the previous expressions, $\tau_r = \frac{I_0}{I}\tau$ and $\tau_{nr} = \frac{I_0\tau}{I_0-I}$. In figure 1.11, we see that the radiative life time is constant at low temperature up to 40 K because of the localization on a discrete donor state and then increases because of the thermal activation of the donor bound exciton into a FX. At higher temperature, the increase of the radiative life time is due to the thermalisation of the FX toward states with $k_{\|} \neq 0$. Indeed as it will be detailed later, the exciton evolves in a 3D density of states giving a rise of the decay times in $T^{3/2}$ at higher temperatures.

At low temperature, the non radiative decay time decreases with temperature and saturates to a value of about 150 ps at 100K and increases between 100K and 300K up to a value of 260 ps. This is an original behavior that can be explained by a thermal quenching of the non-radiative recombinations due to a limited number of non radiative defects: the thermal redistribution between the limited number of non radiative defect states and the exciton band reduces the occupation probability of the non radiative states and increases the non-radiative decay time.

I am now going to come back to the radiative decay time evolutions to understand in details the measured temperature dependence and get a maximum of informations from it. For a photogenerated exciton, the sum over all the level occupation probabilities must be unity:

$$\int_0^\infty dE.D_X(E).p_X(E) = 1 \tag{1.1}$$

D_X(E) is the exciton density of states and $p_X(E) = \frac{1}{Z}.exp(-E/k_BT)$ the canonical occupation probability. Z is the partition function. In our case , the radius of the NWs ($\approx$ 200 nm) is much larger than the exciton Bohr radius ($\approx$ 10 nm). Thus when the exciton is delocalized in the excitonic band, a 3D density of states has to be considered (there is no confinement effect of the exciton due to the NWs geometry). The 3D density of states of the excitonic band can be written:

$$D_X^{3D}(E) = \frac{1}{2\pi^2}(\frac{2M}{\hbar^2})^{3/2}\sqrt{E} \tag{1.2}$$

Where M is the mass of the exciton.

First, let us treat the case of an exciton delocalized in a 3D excitonic band. From equation 1.1 we get:

$$Z(T) = \int_0^\infty dE.D_X(E).exp(-E/k_BT) = \frac{1}{4}(\frac{2M}{\pi\hbar^2})^{3/2}(k_BT)^{3/2} \tag{1.3}$$

Then the decay time τ for an exciton delocalized in a 3D excitonic band reads:

$$\frac{1}{\tau} = \int_0^{E^X_{cinmax}} dE.\frac{1}{\tau_0}\frac{D(E)}{Z(T)}.exp(-E/k_BT) \tag{1.4}$$

Where τ_0 is the radiative life-time for $k_{\|} = 0$. This radiative life-time is linked the FWHM of the zero-phonon excitonic line by the Heisenberg uncertainty relation $\Delta E.\tau_0 = \hbar$.

E^X_{cinmax} is the maximal kinetic energy of the excitons that recombine radiatively:

$$E^X_{cinmax} = \frac{\hbar^2 k^2_{\parallel max}}{2M} \tag{1.5}$$

where M is the exciton mass and $k_{\parallel max}$ the maximum in-plane wavevector of the excitons that recombine radiatively. $k_{\parallel max}$ is linked to the emission energy by the equation:

$$\hbar k_{\parallel max} = n\frac{E_{PL}}{C} \tag{1.6}$$

where n is the ZnO index of refraction and E_{PL} is the exciton emission energy. Then the maximal kinetic energy of the exciton E^X_{cinmax} reads:

$$E^X_{cinmax} = \frac{n^2 E^2_{PL}}{2MC^2} \approx 6.10^{-2} meV \tag{1.7}$$

Thus for all temperatures, $E^X_{cinmax} << k_B T$ and in equation 1.4 $exp(-E/k_B T) \approx 1$
Finally we find:

$$\tau = \tau_0 * \frac{3}{4}\sqrt{\pi}(\frac{C}{nE_{PL}})^3.(2Mk_B T)^{3/2} \tag{1.8}$$

Indeed at high temperatures a dependence in $T^{3/2}$ is found for the radiative decay time in figure 1.11. From the this temperature dependence, we find $\tau_0 = 0.5$ ps which corresponds to a zero-phonon FWHM line $\Gamma_0 = 1.3$ meV. In reference [42] Γ_0 values of about 250 μeV are measured by four wave mixing experiments in ZnO bulck material. Our value of Γ_0 is in the same order of magnitude. We also have to keep in mind the very indirect way Γ_0 is measured in our case. The fact that we find a much larger zero-phonon FWHM line is also certainly due to the NW geometry. Indeed, the τ_0 radiative time related to the zero phonon line is much larger in bulk material where the coupling between the exciton and the photon (strong coupling) leads to the formation of a polariton. In this case, a photon can be emitted only when the polariton state is broken by a defect, a fluctuation...In the case of NWs, the overlap between the photon electric field and the exciton wave function is not enough to reach the strong coupling regime. Thus the zero phonon line radiative time will be much shorter than in high quality bulk material.

To correctly fit the radiative life time in figure 1.11 we have to consider the localization on donor states at low temperature. Taking the donor states energy as origin E^{3D}_X as the bottom of the excitonic band, if we consider a n_D density of donor states the excitonic density of states reads:

$$D_X(E) = n_D\delta(0) + D^{3D}_X\Theta(E - E^{3D}_X) \tag{1.9}$$

Θ being the Heaviside function. Then the partition function Z versus temperature reads:

$$Z(T) = \int_0^\infty dE.D_X(E).exp(-E/k_B T) = n_D + \frac{1}{4}(\frac{2M}{\pi\hbar^2})^{3/2}.exp(-E^{3D}_X/k_B T).(k_B T)^{3/2} \tag{1.10}$$

If τ_D is the donor radiative life time (here τ_D= 295 ps given by our 0K radiative time), we find:

$$\frac{1}{\tau} = \frac{n_D}{Z\tau_D} + \int_{E_X^{3D}}^{E_{cinmax}^X} dE.\frac{1}{\tau_0}\frac{D_X^{3D}}{Z(T)}.exp(-E/k_BT) \tag{1.11}$$

Finally:

$$\begin{aligned}\tau &= Z.[\tfrac{n_D}{\tau_D} + \tfrac{1}{3\pi^2\tau_0}(\tfrac{nE_{PL}}{\hbar C})^3]^{-1} \\ &= [n_D + \tfrac{1}{4}(\tfrac{2M}{\pi\hbar^2})^{3/2}.exp(-E_X^{3D}/k_BT).(k_BT)^{3/2}].[\tfrac{n_D}{\tau_D} + \tfrac{1}{3\pi^2\tau_0}(\tfrac{nE_{PL}}{\hbar C})^3.exp(-E_X^{3D}/k_BT)]^{-1}\end{aligned} \tag{1.12}$$

We can verify that $\tau \to \tau_D$ when $T \to 0$ and the expression of equation 1.8 is found when $T \to \infty$.

The data of figure 1.11 were fitted using the expression of equation 1.12 with E_X^{3D}=15 meV, τ_D=295 ps and by adjusting n_D and τ_0.

A donor concentration n_D of $10^{20}cm^{-3}$ and a τ_0 value of 0.5 ps (as said before) are found.

The high donor concentration found is coherent with the fact that we don't observe the free exciton at low temperature and that the band edge emission peaks are relatively large (see Fig. 1.12 for a comparison with NWs grown on GaN certainly presenting a much lower doping level). The high donor concentration is certainly due to the aluminum coming from the substrate in the case of growth on sapphire.

It is seen in this study that a detailed study of the temperature dependent decay time can provide many informations. An interesting point here is that we could explain the temperature dependence of the radiative lifetime simply considering the delocalization of a donor bound exciton into an excitonic band. The non radiative lifetime behavior indicates a very low non radiative defects density. In the following paragraph we compare those results with the ones obtained for ZnO NWs grown on p-type GaN. The optical properties of those NWs are very different possibly because of the type-II ZnO GaN interface or to a band bending effect at the surface due to a lower donor concentration.

1.3.2 Compared opical properties between ZnO nanowires grown on sapphire and ZnO nanowires grown on p-type GaN

In order to fabricate electroluminescent devices made from ZnO NWs, one has first to master doping issues in these structures. Since p doping of ZnO has not been achieved yet in a reproducible manner, as shown in references [43, 44], a possible way to circumvent this problem is to resort to heterojunctions with a p type material as GaN, for which p-type doping is already mastered [45]. In this paragraph, the optical properties of ZnO NWs grown on p-type GaN are investigated and compared to the optical properties of ZnO NWs grown on sapphire using similar growth conditions. We are going to see that the temperature dependent decay time drastically changes. This could be due to a different doping level or to the type II ZnO-GaN interface. The results obtained with those heterojunctions studies will be very useful for the project presented in paragraph 2.2.

For this study, a 0.89 μm thick Mg-doped GaN layer was grown by MOVPE at 1020^{o}C on top of a 1.5 μm thick unintentionally doped GaN buffer layer grown at 1040^{o}C on c-plane sapphire. This was followed by a 30 minutes annealing at 800^{o}C under N2 to activate the dopants. The effective doping level of the p-GaN layer, measured by a van der Pauw method was of 4.4 x $10^{17}/cm^3$ for a mobility of 9.3 cm^2/Vs. The sample was then transferred into a ZnO MOVPE reactor chamber for the NWs growth. The ZnO NWs growth conditions on

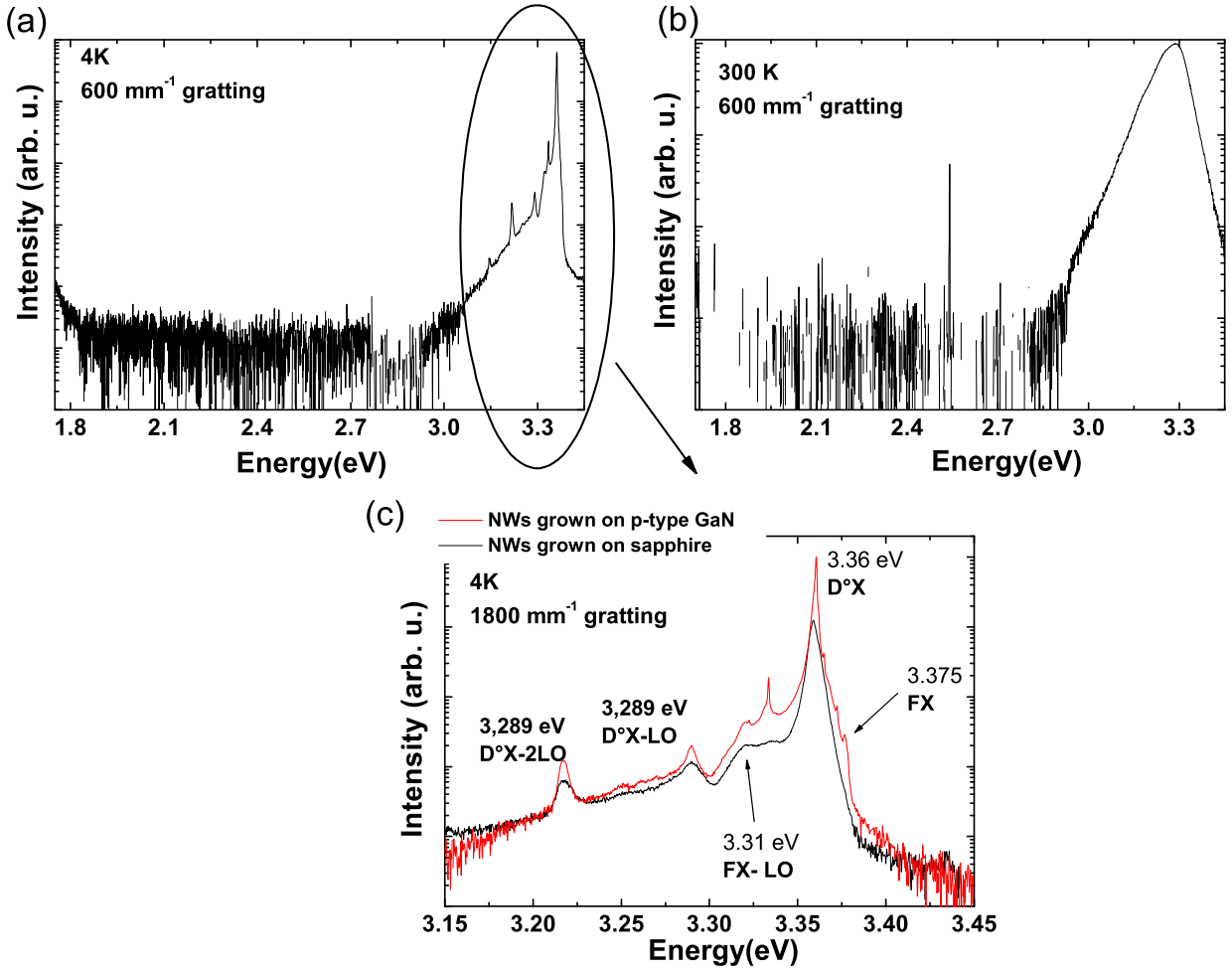

Figure 1.12: (a), (b) PL spectra at 4K and 300K of the ZnO NWs grown on p-type GaN measured with the 600 mm-1 grating. (c) Comparison between the PL spectra of the ZnO NWs grown on GaN and on sapphire. Spectra were measured at 4K with a 1800 mm-1 grating.

GaN are similar to the ones for the growth on sapphire [4]: the ZnO NWs were grown using a catalyst-free MOVPE with a commercial horizontal hot-wall reactor. Diethylzinc (DEZn) and N_2O were used as Zn and oxygen precursors, and argon was used as a carrier gas for the DEZn source. The ZnO NWs were grown at 750-850^oC while the total pressure in the deposition chamber was maintained at 100-150 mbar. The morphology of the samples was investigated by SEM. The NWs grow on top of a 40 nm thick ZnO nucleation layer. The morphology of NWs grown on p-type GaN is different from the one of the NWs grown on sapphire. For the same deposition time, the NWs grown on GaN are shorter: 2.5 μm long vs. 3.5 μm for the NWs grown on sapphire. They are also larger in diameter: 300-450 nm in diameter vs. 150 nm in diameter in the case of growth on sapphire. Their density is smaller: about $5.10^7/cm^2$ vs. $2.10^8/cm^2$ in the case of growth on sapphire.

The PL spectra obtained at 4K and 300K using a 600 mm^{-1} grating between 1.7 and 3.45 eV are presented in Fig. 1.12 (a) and (b). The typical excitation density used for those

measurements is of 5 W/cm^2. The PL spectra between 4K and 300K correspond to ZnO emission, the GaN emission being absent. As in the case of ZnO NWs grown on sapphire [4], no green or yellow luminescence bands are observed, neither at low temperature nor at 300K. This indicates a low density of point defects or extended defects in the ZnO NWs. A close-up of the 4K band edge (BE) emission between 3.15 and 3.45 eV, with the 1800 mm^{-1} grating, is shown in Fig. 1.12 (c) and compared with the PL spectrum obtained for NWs directly grown on sapphire, as detailed in reference [43] and in the paragraph 1.3.1.

In the case of the NWs grown on GaN, the main emission at 4K is a donor bound exciton (D^oX) emission at 3.36 eV. This emission could be due to Ga doping [46, 37] because of gallium diffusion from the GaN layer. Another D^oX emission is also observed at 3.364 eV. The typical full width at half maximum (FWHM) of those D^oX emissions is of 0.5 meV. D^oX emissions at about the same energies are observed in the case of the ZnO NWs grown on sapphire. In the cas of NWs grown on sapphire, the FWHM of the D^oX is of about 1 meV much larger than in the case of NWs grown on GaN. In this case, the D^oX emission at 3.36 eV, although at the same energy, certainly corresponds to Al doping coming from the substrate [37].

It is important to point out here that the free exciton (FX) emission is clearly seen at 3.375 eV only in the case of NWs grown on GaN. This indicates a lower residual doping level. The smaller FWHM of the D^oX emissions in the case of NWs grown on GaN could also be a consequence of the lower residual doping level.

Fig. 1.13 gives the temperature dependence of the BE PL intensity integrated over the whole BE emission versus the inverse of temperature between 4 K and 300 K for NWs grown on p-type GaN and, for comparison, for NWs grown on sapphire. For the two types of NWs, the BE intensity decrease between 35 K and 120 K gives an activation energy of about 13 meV, corresponding to the localization energy of the D^oX exciton [4, 47]. It is remarkable that in the case of the ZnO NWs grown on GaN, the BE intensity remains constant between 120 K and 300 K, whereas in the case of the ZnO NWs grown on sapphire the BE intensity continues to decrease with a higher activation energy of about 50 meV which is, within the experimental error, close to the exciton binding energy (as shown in paragraph 1.3.1). The 4K-300K temperature dependence of the ZnO BE intensity has been studied in many other ZnO based epitaxial layers [47, 48, 49, 50, 51]: a similar behavior whereby PL intensity remains constant for the higher temperatures was never observed. The temperature independent BE intensity above 120K could be a signature of a lower non-radiative defect density in the case of ZnO NWs grown on p-type GaN. The other alternative is is that in the case of NWs grown on GaN, because of the low residual doping level, the surface states induce the formation of a large depletion layer which localize the charges on surface states. This point will be detailed in the next paragraph when discussing about the decay time temperature dependence.

Time resolved PL of the ZnO NWs grown on GaN was also studied. As in paragraph 1.3.1 the measurements were done under weak excitation (3 W/cm^2) and the luminescence decay was measured following the maximum emission between 4K and 300K. The luminescence decay after an excitation pulse is biexponential, whatever the temperature, whereas it is monoexponential (and of the order of 300ps) for ZnO NWs grown on sapphire (cf. ref[4] and paragraph 1.3.1). The first measured decay time, of the order of 150 ps, is constant over the whole temperature range. This decay time is probably a transfer time from the excitation energy to the emitting states. The temperature dependence of the second decay time which varies between 300 and 800 ps is presented in Fig. 1.14. This decay time probably

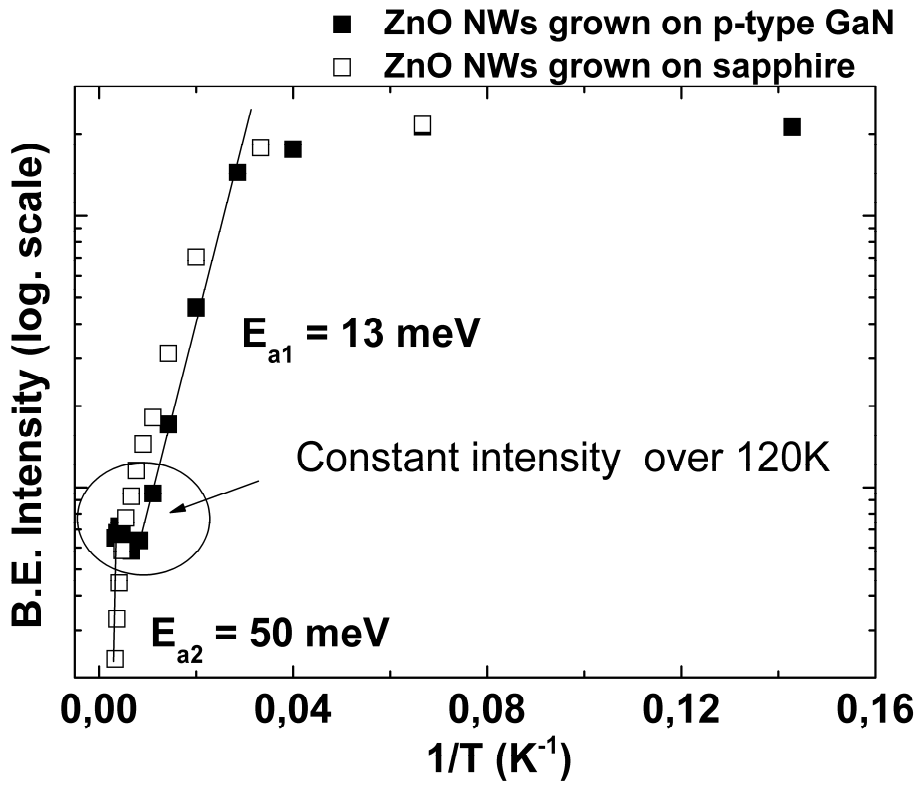

Figure 1.13: BE PL intensity vs. the inverse of temperature of the ZnO NWs grown on p-type GaN measured between 4K and 300K.

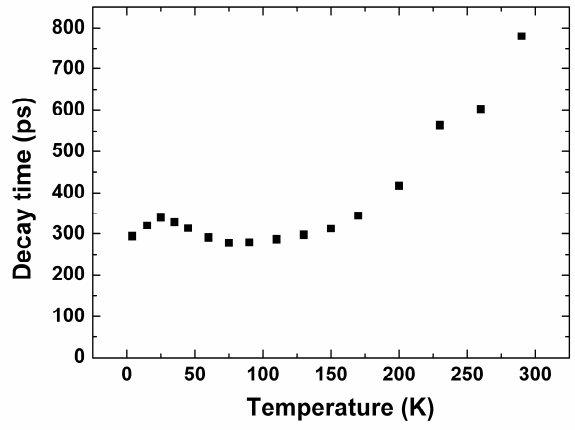

Figure 1.14: Decay time temperature dependence of the ZnO NWs grown on p-type GaN.

corresponds to the emission process in ZnO. It increases between 4K and 30K because the radiative processes are dominant in this temperature range. For higher temperatures the decay time slightly decreases because of the activation of residual non-radiative channels. However, this decrease is much less important than in the case of ZnO NWs grown on sapphire because of a quenching of the non-radiative channels. An increase of the decay time is observed over 120K. The observed quenching of the non radiative channels is possibly due to the type II interface between ZnO and GaN or to a band bending effect due to the surface states as detailed further down.

Figure 1.15 presents the comparison of (a) the temperature dependent decay time (b) the radiative lifetime and (c) the non-radiative lifetime between ZnO NWs grown on sapphire and ZnO NWs grown on p-type GaN. The radiative and the non radiative lifetimes were obtained with the same method presented in paragraph 1.3.1 using the temperature dependent PL intensity and the temperature dependent decay time. It is clearly seen in figure 1.15(a) that even if at 4K the same decay time is measured, much longer decay times are measured in the case of ZnO NWs grown on GaN. In figure 1.15(b), the radiative decay times of ZnO NWs grown on GaN are similar to those measured for ZnO NWs grown on sapphire up to about 40K, when the excitons are still loacalized on donors. For higher temperatures, the radiative decay time greatly increases compared to the radiative lifetime in NWs grown on sapphire. The non-radiative lifetime follows a similar behavior compared to the NWs grown on sapphire, indicating a low density of non-radiative defects.

If we come back to the radiative life time in NWs grown on GaN, at high temperatures, the radiative life time does not follow a low in $T^{3/2}$. Thus the temperature dependence is not governed by the excitonic band filling via thermal activation. The increase of the radiative lifetime could be due to a separation of the electron and the hole either at the type-II interface (Fig. 1.15(d)) or by a band bending effect at the surface of the NWs (Fig. 1.15(e)). Indeed, the GaN/ZnO interface is a type II interface [52] and the electron an the hole of the exciton could be separated if they reach it which would slow down their radiative recombination. However, it supposes that the exciton can diffuse on a length of a few micrometers. The other option is that a band bending effect at the surface of the NWs as represented in Fig. 1.15(e) would separate the electron and the hole and localize the holes on the surface and the electrons in the middle of the NW. This effect has been evoked by many groups in the case of ZnO NWs and powder [53, 54]. The band bending effect is doping level dependent [53]. The width of the depletion region which is also the typical width of the band bending reads [53]:

$$W = \sqrt{\frac{2\epsilon_0 \epsilon_{ZnO} V_{bi}}{eN_D}} \tag{1.13}$$

where V_{bi} is the potential at the surface, e the electronic charge, N_D the donor density and ϵ_{ZnO} the dielectric constant of ZnO. In our case if we consider that $V_{bi} \approx 1$ V (this is the potential difference between the surface states and the vacuum level) we find $W \approx 100$ nm for $N_D = 10^{17}$, $W \approx 3$ nm for $N_D = 10^{20}$

In the case of NWs grown on sapphire, the Al concentration is certainly high and of the order of $10^{20}.cm^{-3}$ (as found with the temperature dependence of the radiative decay time in the previous paragraph). So the band bending effect is not seen in the case of NWs grown on sapphire and this is why a clear dependence in $T^{3/2}$ of the radiative decay time could be measured for those NWs, whereas for NWs grown on GaN, the doping level being certainly much lower (as seen from the comparison of the PL band edge emissions in Fig.

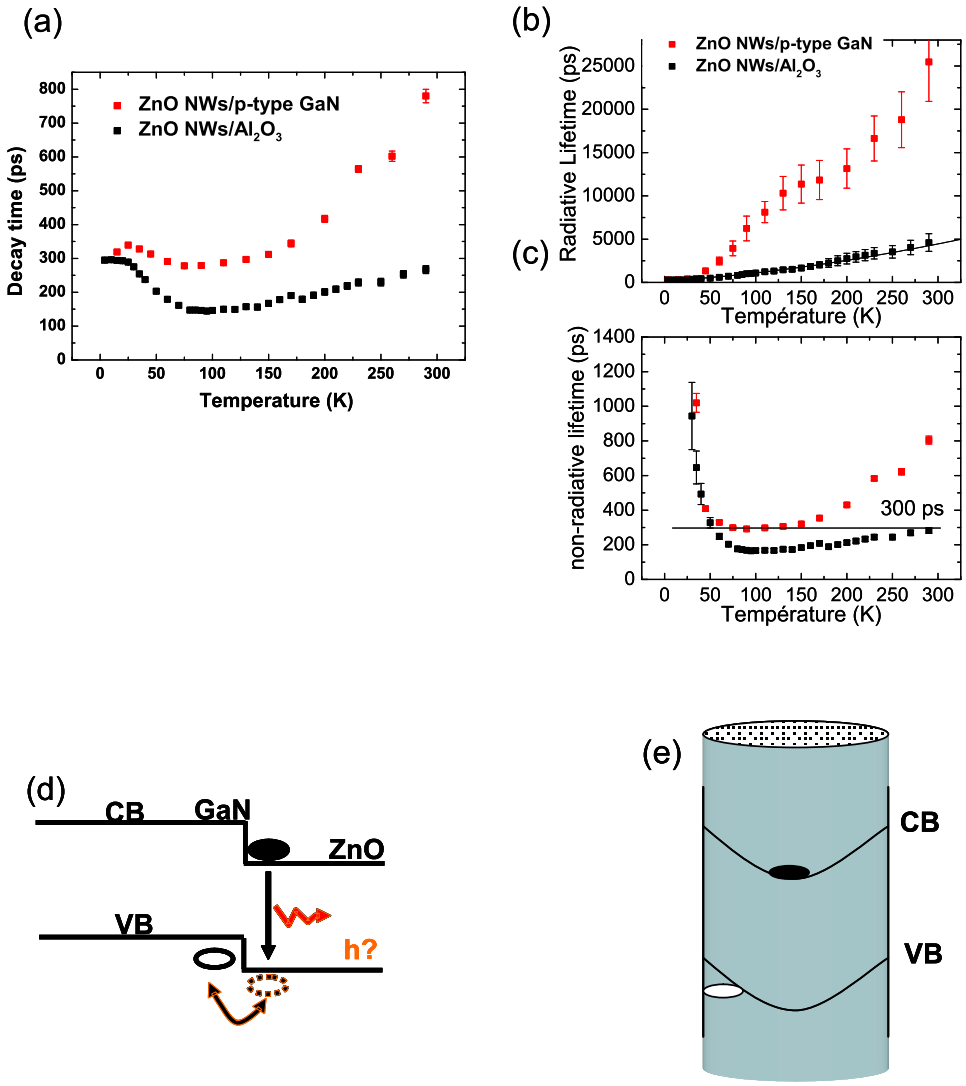

Figure 1.15: Comparison of (a) the temperature dependent decay time (b) the radiative lifetime and (c) the non-radiative lifetime between ZnO NWs grown on sapphire and ZnO NWs grown on p-type GaN. (d) electron-hole separation at the GaN-ZnO type II interface. CB abd VB are the conduction and valence band respectively. (e) electron-hole separation in a ZnO NW due to a band-bending effect at the surface.

1.12), the width of the depletion region due to surface states is much larger and the charges can be separated in this depletion region leading to a rise of the radiative decay time.

In conclusion, ZnO NWs grown on p-type GaN show that the residual doping level is much lower than for ZnO NWs grown on sapphire. The activation of non-radiative channels is more limited than in the case of ZnO NWs grown on sapphire. Compared to NWs grown on sapphire, in ZnO NWs grown on GaN, the radiative recombination time is greatly increased probably to an electron-hole separation. This effect seems to quench the non-radiative channels as the PL intensity is constant above 120K. Thus ZnO NWs grown on GaN show very interesting properties for room temperature emission. Similar material systems with NWs heterojuctions will be used in the project presented in paragraph 2.2 in order to obtain efficient UV electroluminescence.

1.3.3 Compared optical properties of ZnO 2D layers

In this section the optical properties of ZnO 2D layers grown by MOVPE, MBE or liquid phase epitaxy (LPE) are compared. In particular, ZnO homoepitaxial growth is shown to change the luminescent properties of ZnO in a substantial way. Temperature dependent (4K-300K) PL properties of the films grown by MOVPE or by LPE are compared to those of the hydrothermal ZnO substrate used for the growth. The intensity ratio between the free exciton and the donor bound exciton strongly increases following homoepitaxial growth. The activation energy of the band edge emission intensity also increases from 13 meV which corresponds to the donor bound exciton localization energy, up to a value of 60 meV, corresponding to the free exciton binding energy. This indicates that homoepitaxial growth favors free exciton emission instead of donor bound exciton emission and certainly lowers the residual doping level.

The spectroscopic properties of ZnO epilayers grown by MBE are also investigated. Three samples are compared: an homoepitaxial layer grown on a Crystec substrate, a sample directly grown on c-sapphire and a layer grown on c-sappire using a MgO buffer. In the latter case, in spite of the high dislocation density, temperature-dependent photoluminescence measurements show only a small decrease of the luminescence intensity between 4K and 300K, with an activation energy of 108 meV. Cathodoluminescence presents an inhomogeneous emission on the micrometric scale: a stronger emission is measured in small nanometric areas. A tentative explanation of this behavior is proposed.

Low residual doping level in homoepitaxially grown ZnO layers

Since ZnO substrates are already commercially available [55], homoepitaxial growth allows limiting the density of dislocations that would thread through the active layers. In previous reports, the preparation of ZnO substrates by thermal annealing was investigated, homoepitaxial growth of ZnO on ZnO has been performed and the growth conditions for two dimensional growth have been established, mainly using structural characterizations (X-ray diffraction and atomic force microscopy) [56, 57, 55, 38, 58, 59, 60]. For instance, the growth temperature range has been determined in order to obtain smooth surfaces after growth on Zn-polar (0001) or O-polar ($000\overline{1}$) surfaces by plasma assisted molecular beam epitaxy [57]. It was also shown that a crystal quality better than the ZnO substrate one can be obtained for a ZnO layer homoepitaxially grown by metal organic vapor phase epitaxy (MOVPE) [38, 58]. However only a few contributions report on the optical properties of homoepitaxial layer [38, 59, 61, 62, 60]. In references [61, 62], the homoepitaxial layers

photoluminescence (PL) emission was found to be broader than for the substrates. We study in this section the band edge emission of samples grown by MOVPE or liquid phase epitaxy (LPE) and their optical properties are compared to those of the substrates used for the growth. In references [38, 60] the low temperature spectra of homoepitaxial layers were found to be dominated by donor bound excitons. Our PL temperature dependence (4K-300K) of LPE and MOVPE homoepitaxially grown samples is presented in this section. It is shown that homoepitaxial growth allows to significantly reduce the donor bound exciton (D°X) emissions relatively to the free exciton (FX) emissions.

The MOVPE samples were grown on hydrothermal substrates from Crystech and the LPE sample was grown on an hydrothermal substrate from Tokyo Denpa. Prior to growth, the substrates were annealed in oxygen-rich atmosphere at 1100°C for four to five hours [63]. For MOVPE growth, the typical growth temperature is 850°C, with N_2O as oxygen precursor and diethylzinc (DEZn) as group II precursor. Argon is used as the carrier gas and the reactor pressure is set to 100 mbar. Two samples were grown with a N_2O:DEZn flux ratio (VI/II flux ratio) of 6000 and 25000 respectively. Note that this flux ratio is much higher than the one used to grow NWs. Under these growth conditions, ZnO layers about 1 μm thick are obtained. For LPE growth, the growth temperature is 640°C and the growth is done under ambient atmosphere. The details of the growth method used for the LPE grown sample are described in reference [63]. The PL spectra were obtained using an excitation density of $3W/cm^2$. The low temperature PL band edge (BE) emission of the MOVPE samples and an annealed Crystech substrate are compared in Fig. 1.16(a). In order to compare the layer with the substrate it is grown onto, we studied a substrate annealed in the same conditions as for MOVPE growth. The PL spectra were not normalized so that the PL intensities of the different emissions can directly be compared on the figure. For the annealed substrate, the donor bound exciton (D°X) emitting at 3.361 eV dominates the BE emission of the substrate. The intensity of the A-free exciton (FX_A) emission at 3.375 eV is 600 times less intense than the D°X one (cf. Table 1.1). Two LO phonon replica D°X-LO and D°X-2LO of the D°X emission emitting at 3.289 eV and 3.217 eV are also seen in the spectrum. Those donor related emissions are certainly due to Aluminum [37, 55] and other impurity incorporation during hydrothermal growth. Indeed, Hall measurements reveal a n-type conductivity with a mobility of 150 cm^2/Vs at 300K for this substrate and a carrier concentration $3.7.10^{12}/cm^2$ (the surface conduction channel usually measured on such substrate unables the estimation of the volume carrier concentration, because of the unknown value of the thickness of the surface conduction channel). The donor doping concentration obtained by C(V) measurements is $2.10^{16}/cm^{-3}$ at 300K. Only a weak emission of the FX_A-LO phonon replica is observed on the 4K spectrum.

In the PL spectrum of the MOVPE sample grown with a VI/II flux ratio of 6000, the same D°X and FX_A emissions as for the annealed substrate are observed. However, the D°X intensity is 5 times lower and the FX_A intensity 4 times higher than in the case of the hydrothermal substrate. An intensity ratio of 30 between the D°X and the FX_A emission is measured which is 20 times lower than in the case of the substrate (cf. Table 1.1). The D°X LO phonon replica are weaker whereas the FX_A LO phonon replica are stronger than in the case of the substrates: two of them are clearly observed for this sample. Those observations indicate a lower donor concentration in this sample. However, Hall measurements are difficult for homoepitaxially grown samples, because homoepitaxial growth make it difficult to discriminate the conduction through the substrate and the conduction through the layer. In this layer, the emission at 3.331 eV comes from excitons bound to defects and is known

Sample	$\frac{I_{D^\circ X}}{I_{FX_A}}$(4K)	$I_{D^\circ X}$(4K) (arb. units)	I_{FX_A}(4K) (arb. units)	$\frac{I_{BE}(4K)}{I_{BE}(300K)}$
Crystech substrate	600	27000	45	390
Tokyo Denpa substrate	150	50000	350	340
MOVPE sample VI/II flux ratio of 6000	30	5200	170	128
MOVPE sample VI/II flux ratio of 25000	0.8	850	1050	70
LPE sample	0.25	400	1400	60

Table 1.1: Comparison between the different samples of the D°X to FX_A intensity ratio at 4K, the D°X and FX_A intensities at 4K as well as the band edge intensity ratio between 4K and 300 K.

as the Y line [37]. The presence of the defects revealed by the Y line is certainly due to non optimum growth conditions with a too low VI/II flux ratio.

In the case of the MOVPE grown sample with a VI/II flux ratio of 25000, the D°X and the FX_A emissions have about the same intensity (cf. Table 1.1), the D°X intensity being 30 times lower and the FX_A intensity 25 times higher than in the case of the hydrothermal substrate. In addition, the D°X LO phonon replica are not observed anymore, instead three LO phonon replica of the free exciton are observed. Thus, for optimized growth conditions MOVPE homoepitaxial growth drastically changes the low temperature BE emission properties, the excitons being no more localized on donor centers. Note that no significant difference is found in terms of structural properties as obtained by X-ray diffraction for the MOVPE grown samples. In rocking-curve measurements a full width at half maximum (FWHM) of 18 arcsec is measured on the ZnO (002) diffraction for both samples with a value of about 30 arcsec for the hydrothermal substrate. Thus the VI/II flux ratio mainly affects the optical properties and the residual doping level into the layers. However, for the optimized growth conditions with a VI/II flux ratio of 25000, the Y line, attributed to the presence of extended defects [37] is not anymore present in the PL spectrum.

In Fig. 1.16(b), the 4K spectrum of a Tokyo Denpa substrate annealed in the same conditions as for LPE growth is compared to the LPE grown layer. The Tokyo Denpa substrate spectrum is very similar to that of the Crystech substrate (Fig. 1.16(a)), with a D°X emission at 3.361 eV dominating the spectrum. For this substrate, the ratio between the D°X and FX_A intensities is of 150 (cf. Table 1.1). Temperature dependent Hall measurements reveal a carrier concentration of $2.6.10^{14}$ cm^{-3} and a mobility of 200 cm^2/Vs at 300K. No surface conduction channel was measured. Using the neutrality equation the donor concentration level at $2.10^{15}/cm^3$ is measured. The PL spectrum of the LPE grown sample is also very similar to that of the layer grown by MOVPE with optimum VI/II flux ratio: compared to the hydrothermal substrate, the D°X intensity is 125 times weaker and the FX_A intensity 4 times stronger (cf. Table 1.1). Thus, for this sample, the FX_A emission is 4 times stronger than the D°X emission, no LO phonon replica of the D°X emission are seen whereas three LO phonon replica of the FX_A emission are present indicating a low residual doping level in the layer. Similar structural properties are measured by X-ray

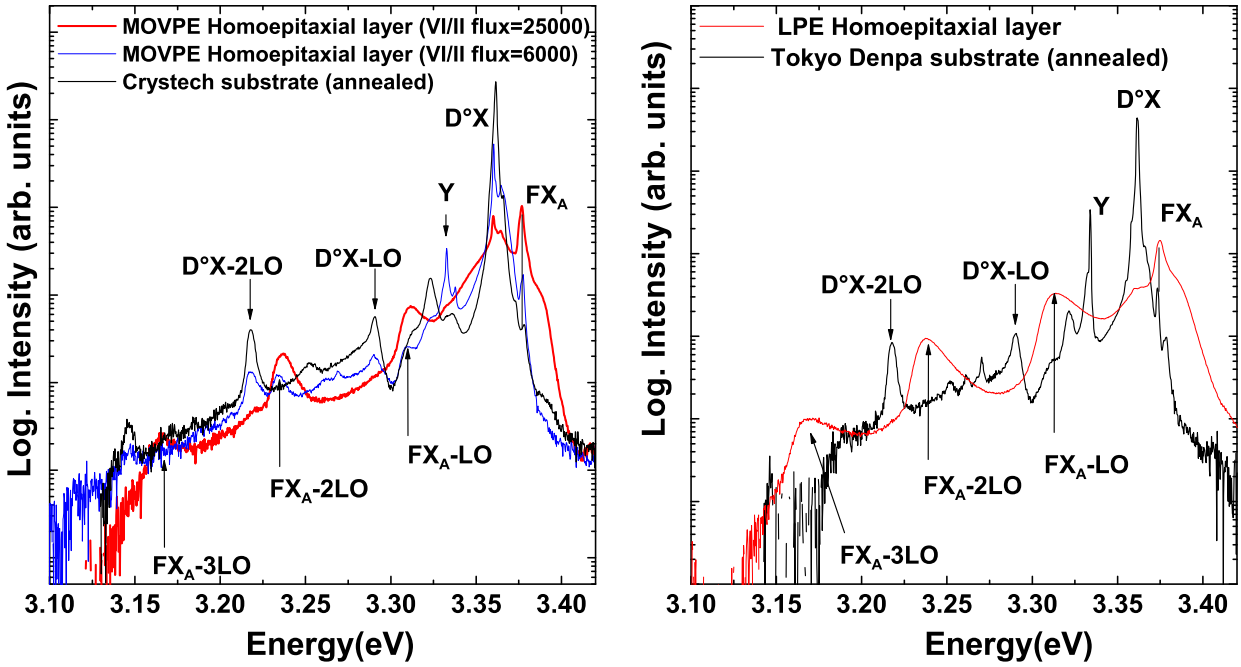

Figure 1.16: (a) Comparison of the low temperature (4K) PL spectra between an annealed Crystech substrate and the MOVPE homoepitaxially grown samples. (b) Comparison of the low temperature (4K) PL spectra between an annealed Tokyo Denpa substrate and the LPE homoepitaxially grown sample.

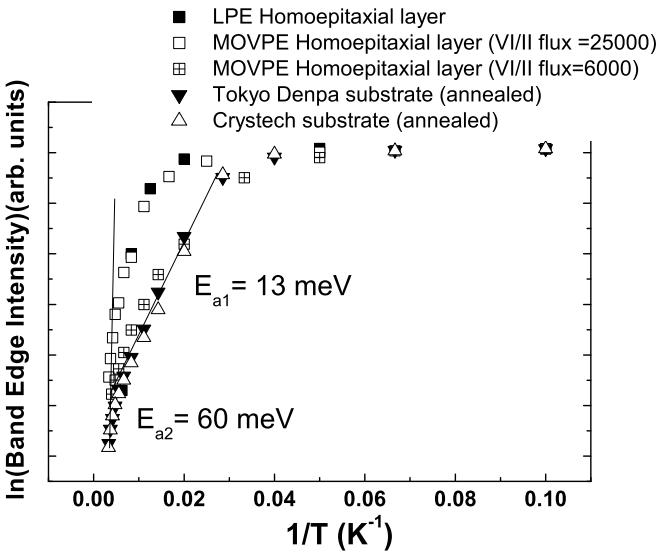

Figure 1.17: Arrhenius plots (logarithm of the BE emission integrated intensity *vs* the inverse of temperature) for the annealed substrates and the different samples.

diffraction on the LPE grown layer and the hydrothermal substrate with a FWHM of the ZnO (002) diffraction of about 30 arcsec measured for both samples. However, the Y line seen in the PL spectrum of the hydrothermal substrate used for the LPE growth is not visible anymore in the PL spectrum of the LPE layer, indicating a lower concentration of extended defects in the layer.

In Fig. 1.17, Arrhenius plots (logarithm of the intensity *vs* 1/T) of the BE emission intensity of a Tokyo Denpa substrate and a Crystech substrate annealed in the same conditions as before are presented with those of the MOVPE and the LPE grown layers. The PL intensity was integrated over the whole BE spectral range. For the substrates and for the MOVPE sample grown with a 6000 VI/II flux ratio, two activation energies of 13 meV typically between 10 K and 100 K and of 60 meV above 120 K are measured. As in the case of ZnO NWs, the 13 meV activation energy corresponds to a donor localization energy. This is in agreement with the PL spectra temperature dependence (not shown): for those samples, at low temperature the D°X exciton at 3.361 eV and its LO phonon replica dominate the spectrum, the FX emission intensity being about 100 times lower (cf. Fig. 1.16). When increasing the temperature, the FX_A emission increases relatively to the D°X emission, together with its LO phonon replica. Around 100 K the FX_A contribution is equivalent to the D°X one and at room temperature the 1-LO phonon replica of the FX dominates the spectrum as observed by other groups [36, 33]. Indeed, the 60 meV activation energy measured above 120 K corresponds to the exciton binding energy. In the case of the LPE grown sample and the MOVPE grown sample with optimum VI/II flux ratio, only one activation energy of 60 meV, corresponding to the exciton binding energy is measured. This is in agreement with the PL spectra measured on those samples, dominated, from low temperatures, by free exciton emissions.

This comparative study of the PL spectra obtained on ZnO substrates and on homoepitaxial layers grown onto these substrates reveal that homoepitaxial growth favors FX emissions indicating a lower residual doping level in homoepitaxially grown layers. Those properties presented by the optimized MOVPE and LPE grown layers are promising for controlled p-type doping or field effect hole injection into ZnO (as described in the project presented in paragraph 2.2).

MBE grown ZnO layers

In this section, we compare the optical properties of three two-dimensional (2D) ZnO layers grown by MBE. Similar growth conditions were used. The main difference between these samples is represented by their substrates: the first sample was homoepitaxially grown on a ZnO hydrothermal substrate, the second one was grown on c-sapphire substrate and the third on a MgO buffer layer. Then, the optical properties of the homoepitaxial MBE layer are compared to those of the 2D homoepitaxial layers grown by MOVPE.

The three MBE grown samples studied were grown using a modified Varian Gen II MBE system that was pumped down to a base pressure of 10^{-8} torr. Pure Zn (6N) was supplied by means of a solid source double-zone effusion cell. Zn deposition rates were measured by a quartz thickness monitor at the substrate position prior to and after the growth. 6N oxygen gas is injected into an Addon RF-plasma source through a mass flow controller (MFC) system to produce reactive oxygen radicals. The first sample was grown on a ZnO substrate from Crystec, the second one was directly grown on a cleaned c-sapphire substrate and the third one was grown on a MgO layer grown on a clean c-sapphire substrate at 800°C before the ZnO growth. The growth conditions of the ZnO layers for the three samples are

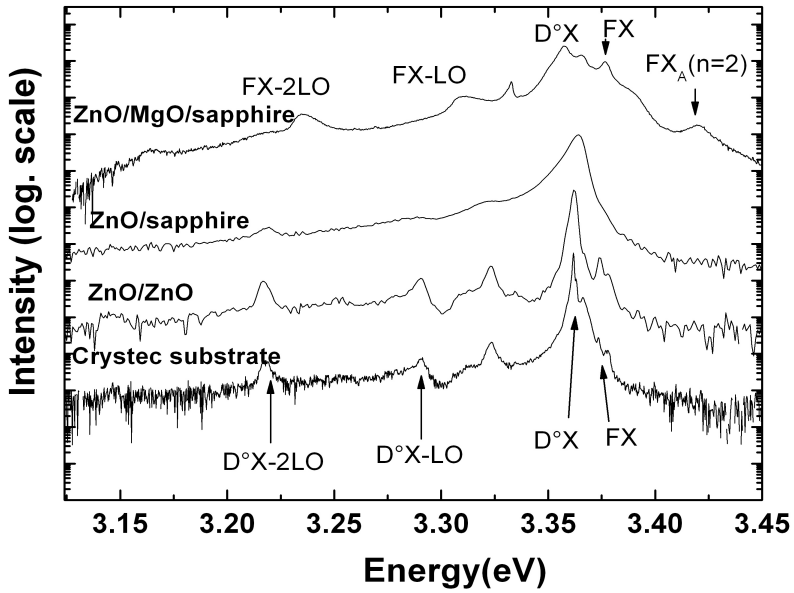

Figure 1.18: Low temperature (4K) BE PL spectra of (from bottom to top) a Crystec substrate, the homoepitaxially grown MBE sample, the MBE sample directly grown on sapphire, the MBE sample grown on a MgO buffer layer.

then similar with the growth around 300°C of a 10 nm low temperature buffer layer, the rest of the growth having been carried out at 500°C. The thicknesses of the MBE grown ZnO layers are of the order of 500 nm. The growths were carried out under oxygen-rich conditions with a VI/II flux ratio of about 1.25. The growths were done at the Institute of Semiconductor Technology in the Technical University of Braunschweig, Germany and details are described elsewhere [64, 65]. Fig. 1.18 compares the low temperature (4K) band edge (BE) PL spectra of the three MBE grown layers and a Crystec substrate, similar to the one used for the homoepitaxial growth. The PL spectra were obtained in the same experimental conditions using a low excitation density of about 10 W/cm^2. In the case of the Crystec substrate, the homoepitaxially grown sample and the sample directly grown on sapphire, the BE PL spectra are dominated by the D°X emission at 3.36 eV, corresponding to Al incorporation [37]. The free exciton (FX) emissions are observed for all samples except for the sample directly grown on sapphire. For this sample, the D°X emission is very broad with a full width at half maximum (FWHM) of 7 meV. For the other samples the FWHM of the D°X emissions is of about 1 meV. Thus a poorer crystal quality is obtained in the case of growth directly on sapphire. The FX to the D°X intensity ratio significantly changes between the samples: the FX to the D°X intensity ratio is higher in the case of the homoepitaxially grown sample compared to the Crystec substrate. As in paragraph 1.3.3 this probably corresponds to a lower unintentional doping level and a good crystalinity in the case of homoepitaxial growth. The PL of the ZnO layer grown on a MgO buffer layer presents many singularities: first of all the main D°X emission is at 3.357 eV instead of 3.36 eV for the other samples. Thus the emission attributed to Al incorporation is not found. The MgO buffer probably stopped the Al diffusion from the substrate. In addition, for this sample, the FX and the D°X emission intensities are of the same order of magnitude, showing a very good crystal quality and a low unintentional doping level. For this sample,

the D°X phonon replica are not seen: only the FX phonon replica are observed.

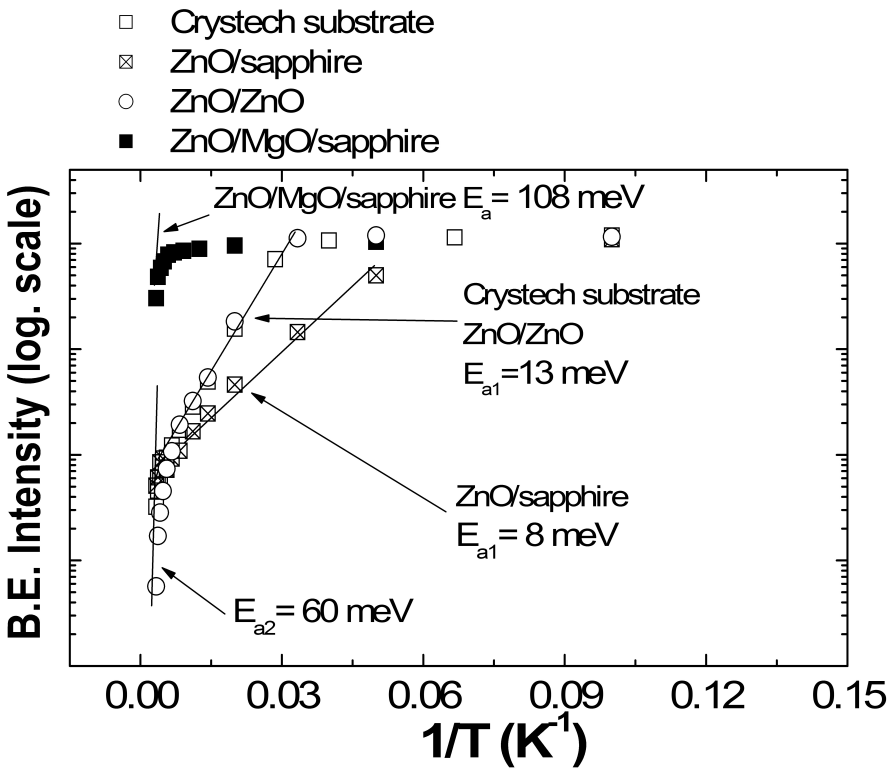

Figure 1.19: BE PL intensity v.s. the inverse of temperature of a Crystec substrate, the homoepitaxially grown MBE sample, the MBE sample directly grown on sapphire, the MBE sample grown on a MgO buffer layer.

Fig. 1.19 gives the temperature dependence of the BE PL intensity integrated over the whole BE emission versus the inverse of temperature between 4K and 300 K for the MBE grown samples as well as for the Crystec substrate. Different activation energies can be measured. In the case of the sample directly grown on sapphire, an activation energy of 8 meV is measured between 30 K and 100 K. This low activation energy probably corresponds to the activation of non-radiative channels because of the poor crystal quality of the ZnO layer. For the homoepitaxially grown sample and the Crystec substrate, two activation energies of 13 meV between 50 K and 120 K and of 60 meV between 130 K and room temperature are measured. The first one corresponds to the donor localization energy [47] and the second one to the FX binding energy. The two activation energies found correspond to a transfer from the bound exciton to the FX. For the sample grown on a MgO buffer layer, only one activation energy of 108 meV is measured for temperatures above 200 K. This is surprising: the estimated dislocation density is of the order of $10^{10}/\mathrm{cm}^2$ [65] and one would expect a much more efficient activation of the non-radiative channels. To try and understand this behavior, CL characterizations were performed.

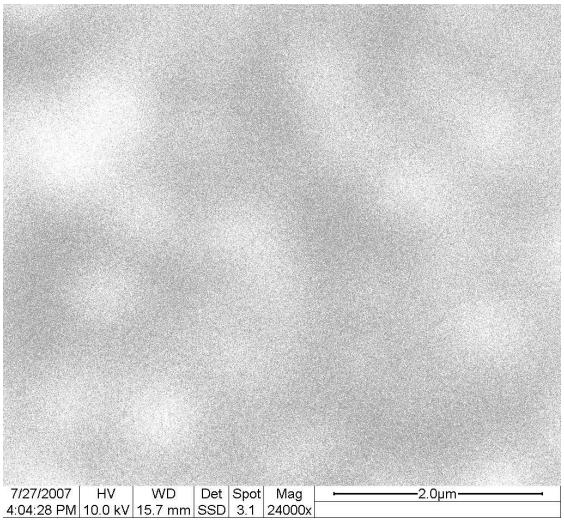

Figure 1.20: Low temperature (4K) CL image obtained using the emission at 3.357 eV (corresponding to the maximum intensity of luminescence).

Fig. 1.20 gives a CL image obtained at 4K using a SEM system with a variable temperature (4K-300K) sample holder. The electron energy is 10 kV and the spot size 10 nm. The interaction volume in those excitation conditions has a lateral size of the order of 100 nm. The emission energy used for the CL image is 3.357 eV, corresponding to the maximum intensity of the 4K spectrum. It is found that the CL image is not spatially uniform: the bright zones of micrometric size display a much higher intensity, typically a factor of three higher than the dark areas. Note that the micrometric sizes of the bright and dark zones are much larger than the lateral size of the interaction volume. Higher intensity areas have a density of $2.10^8/\text{cm}^2$ i.e. two orders of magnitude lower than the dislocation density [65]. A possible explanation relies on the columnar structure of the ZnO epilayer when grown on heterosubstrate [66]. The sub-grain boundaries between columns are composed of threading dislocations. These threading dislocations may be diffusion paths for Mg atoms coming from the MgO buffer. This would lead to Mg-enriched zones around sub-grain boundaries, leading to potential fluctuations and localization potentials for excitons within the sub-grains. Furthermore, Mg diffusion in the core of the dislocations may lead to dangling bound passivation, explaining the high activation energy measured in the temperature dependence PL measurements.

Comparison with MOVPE homoepitaxially grown ZnO layers In paragraph 1.3.3, we saw that MOVPE homoepitaxal growth allows reducing the D°X emissions relatively to the FX emissions. It was found that the FX to D°X intensity increases when increasing the VI/II flux ratio. For a VI/II flux ratio of 25000, the D°X emission intensity is similar to the one of the FX emission. In addition, for this MOVPE sample, only one activation energy of 60 meV, corresponding to the FX binding energy is measured in temperature-dependent PL measurements (cf. paragraph 1.3.3). So it seems that increasing the VI/II ratio allows one to reduce the unintentional doping level. In the case of MBE growth, the VI/II flux ratio used for homoepitaxial growth seems to be too low to prevent high unintentional doping levels. The growth using MgO buffer layer appears therefore to be more promising and

could also be used for growth on ZnO substrates.

1.3.4 Conclusion on ZnO optical studies

The optical characterizations of different ZnO material systems allowed us to outline the evolution of non radiative defects and dopant concentration with the growth procedures.

In the case of ZnO NWs, our temperature dependent decay time measurements show that the activation of the non-radiative channels is more limited in the case of NWs grown on p-type GaN than in the case of ZnO NWs grown on sapphire. In the case of NWs grown on sapphire, the temperature dependence of the radiative decay time follows a low in $T^{3/2}$, consistent with a delocalization of the exctions at high temperatures in a 3D excitonic band. From the temperature dependence of the radiative decay time a FWHM of the zero-phonon line of 1.3 meV and a high residual doping level of $10^{20}.cm^{-3}$ are measured. The FWHM of the zero phonon line is larger than what was measured by other groups in bulk material (typically 250 μeV [42]). This could be due to the NW geometry leading to a poor overlap between the exciton wave function and the photon electric field. The high residual doping level is certainly due to the diffusion of aluminum form the sapphire substrate.

In the case of NWs grown on GaN, the residual doping level is certainly much lower than in the case of NWs grown on sapphire. Indeed, the FX emission is seen at 4K and the D^oX emissions are much thiner than in the case of NWs grown on sapphire. In addition, the temperature dependence of the radiative decay time is not governed by the filling of an excitonic band via thermal activation. Compared to NWs grown on sapphire, the radiative decay time is much longer probably because of a band bending effect that separates the electron and the hole. This band bending effect depends on the residual doping level and is not seen in the case of NWs grown on sapphire probably because of a very high residual doping level.

MOVPE and MBE grown layers were then studied by temperature dependent PL measurements. The increase of the VI/II flux ratio seems to decrease the unintentional doping level. For MBE grown samples, the unintentional doping level in the case of homoepitaxially grown sample seems to be higher than in the case of MOVPE homoepitaxial growth with a high VI/II ratio. The use of a MgO buffer layer for MBE growth on sapphire is a promising growth method to take full advantage ofdf the ZnO exciton strength. However I would like to point out here that the optical studies have there limits: the PL measurements only give us an indication about the unintentional doping level. To really access to the carrier concentrations, Hall measurements or other transport measurements are needed. In the case of homoepitaxially grown samples, Hall measurements are often difficult to interpret because the conduction channels of the epilayer and the substrate are measured simultaneously. Other techniques as maximum entropy mobility-spectrum analysis (MEMSA) using Hall measurements at different magnetic fields could be used to try to differentiate the different conduction channels in Hall measurements.

The temperature dependent time resolved photoluminescence would also be very interesting to perform on the high quality 2D layers. In particular it would be very interesting to compare the radiative decay time to what is found in the case of NWs. In the case of a 2D layer, the FWHM of the zero-phonon line measured from the temperature dependence of the radiative decay time should be much smaller than in the case of NWs because of the formation of a polariton by the exciton-photon interaction. The dependence of the measured FWHM of the zero-phonon line with the doping level would also be very interesting to study: the FWHM of the zero-phonon line should increase with the doping level because

the polariton is more likely to emit radiatively when the doping level increases. However, very good quality 2D layers are needed because if the non-radiative channels are dominant, the radiative decay times calculated from the PL intensity and decay time temperature dependence is not very accurate.

During my one year post-doctorate I did bot have enough time to do those studies but it would be very interesting to continue it. They might be continued by PhD students in the project presented in paragraph 2.2, as all those results will be useful for the choice of the correct material system to optimize field effect LEDs structures.

1.4 Growth and Optical Characterization of HgCdTe Epilayers

1.4.1 MBE Growth of 4 Inch MCT Epilayers

After my second post-doc, I was hired on a permanent position to work on the growth of 4 inch mercury cadmium telluride (MCT) layers by MBE. MCT is extensively used for infrared detection applications and MBE is a growth technique that offers many advantages for dopant incorporation, multispectral layer growth and growth on large area substrates [67, 68]. The main problem for MBE growth of MCT is the control of the surface temperature during growth [69, 70]. The temperature window in which the MBE growth occurs in good conditions is of about 5^oC large and the growth occurs at low temperature (around 170^oC) which increases the difficulty of controlling the growth temperature [70, 71].

The Optronics Department where I was hired already had a good experience in MBE growth and a robust growth process already existed with Riber 32P and 2300 machines. However the sample size on those machines is limited to 3 inches. To decrease the fabrication cost of infra-red detectors, it is interesting to grow on large area substrates. This is why a Riber Epineat machines has been bought, allowing the growth on 4 inches substrates. My work consisted in optimizing the growth conditions on a Riber Epineat machine. The main difficulty for MCT growth in those machines is the control of the temperature homogeneity and stability during the growth on large area substrates.

The MCT growth is done on 4 inches CdTe/Ge pseudo substrates. Those pseudo substrates are grown in the same machine by the deposition of a 7 μm thick CdTe layer on a (211) Ge substrate. Then, the MCT growth takes place under a vaccum pressure of 10^6 torr. The growth temperature is typically 170^oC. Hg, Cd and Te materials are evaporated by Knudsen effusion cells heated around 350^oC for Cd and Te and 170^o for Hg. The growth temperature is controlled by a thermocouple at the back of the substrate holder. The growth can also be monitored by in-situ ellipsometry.

To control the temperature homogeneity, specific 4 inch substrate holders had been developed. For confidentiality reasons, the geometry of those substrate holders can not be detailed here. With those substrate holders, a temperature homogeneity of $\pm 1.5^oC$ can be obtained. With those substrate holders, epilayers with a good crystalline quality could be grown but with a surface defect density too high for the fabrication of good quality IR detectors. The type of defects found on the epilayer tells us if the growth temperature was too high or too low [69, 70]. If the growth temperature is too low microvoids defects as shown in figure 1.21(a) are found. If the growth temperature is too high tellurium precipitates as shown in figure 1.21(b) are found.

With the high uniformity substrate holders, the defect density was of the order of 10^4 to

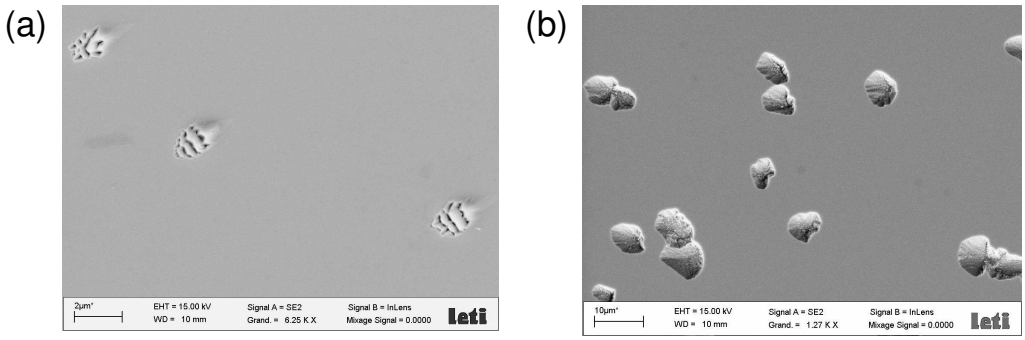

Figure 1.21: (a) Microvoid defect on MBE grown MCT epilayers found when the growth temperature is too low. (b) Tellurium precipitate on MBE grown MCT epilayers found when the growth temperature is too low.

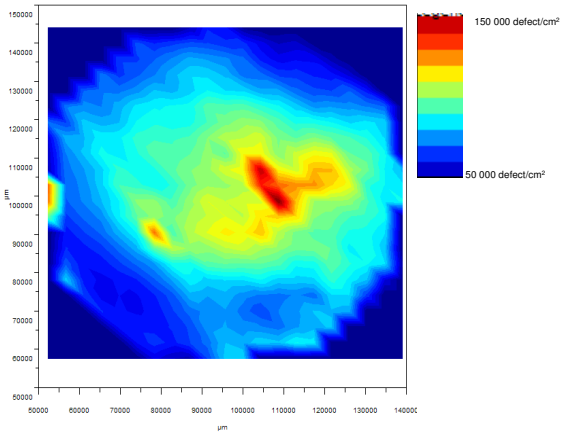

Figure 1.22: Cartography of the defects density measured on a 4 inch MCT epilayer MBE grown using a standard process.

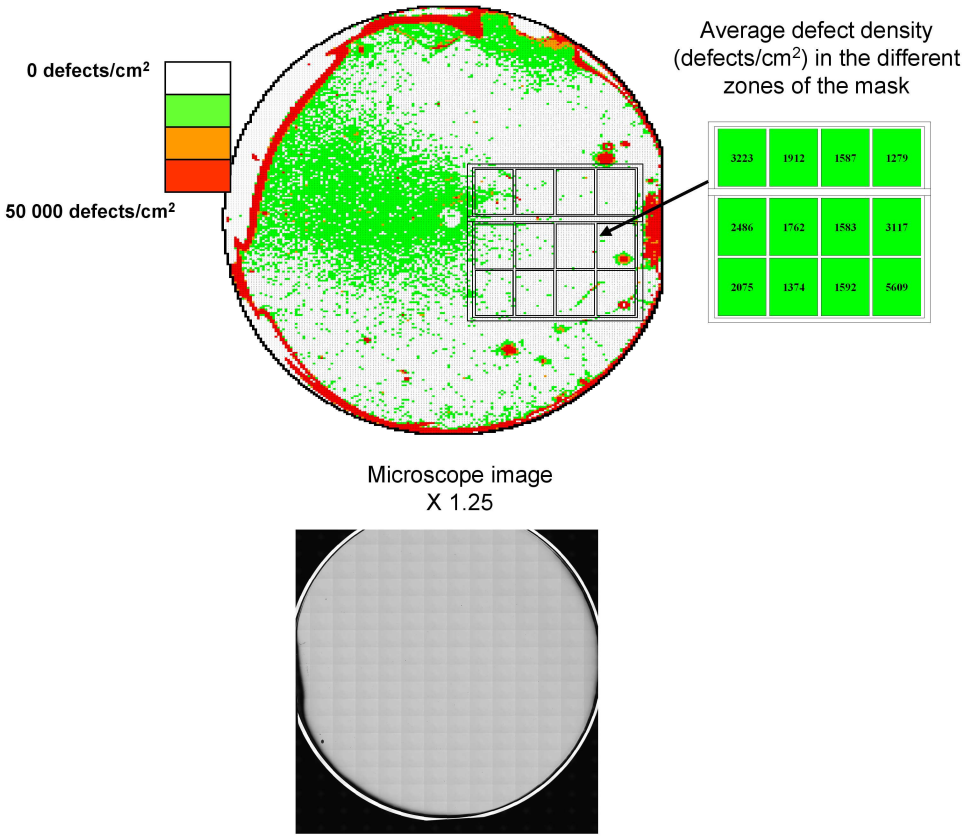

Figure 1.23: Cartography of the defects density measured on a 4 inch MCT epilayer MBE grown using the optimized process. The average defect density was measured in the different zones of the mask drawn on the cartography image. A microscope image obtained with a magnification of 1.25 is also shown at the bottom.

10^5 defects per cm^2. In figure 1.22 a cartography of the defects density measured on a 4 inch MCT epilayer grown using a standard process is shown. The defect density is measured using an optical microscope. The defect density varies between 50000 and 150000defects /cm2. Both type of defects: microvoids and tellurium precipitates were found which suggested that this high defect density was due to temperature instabilities during growth.

My work in MBE growth consisted in decreasing this defect density. Using in-situ ellipsometry measurements, I developed a specific growth procedure which allowed to decrease the defect density to 2000 defect/cm^2 as shown on figure 1.23. This process stabilized the surface temperature during the growth. However for confidentiality reasons I can not detail the growth process that was developed. I will thus focus now on the optical properties of MCT epilayers that were studied by PL measurements.

1.4.2 Photoluminescence of HgCdTe Epilayers

In parallel with my growth activity, I studied the photoluminescence of $Hg_{1-x}Cd_xTe$ ($0.3 \leq x \leq 0.7$) layers grown by MBE or liquid phase epitaxy on CdZnTe or CdTe/Ge substrates. The in-

vestigations were carried out on unintentionally doped, indium doped and arsenic doped samples, and the effects of different annealing procedures were examined. Thus a large variety of samples were studied. Most of the MBE samples were grown in a Riber 32P and 2300 machines at the laboratory for which robust growth process already existed.

When I arrived at the laboratory there was no infra-read PL setup operating at 4K at the laboratory. Thus the measurements were done at the GEMAC CNRS laboratory in Meudon and most of the presented data were measured in Meudon with a modulated PL setup using a continuous-scan Fourier transform infrared spectrometer (FTIR). I proposed a PhD subject on the PL studies of HgCdTe in 2009. A PhD student, Frédérique Gemain was hired in november 2009. An infra-red PL setup opetating at 4K was developed during the first months of this PhD thesis and is now available at the laboratory.

In this section I will focus on As-doped MBE samples. For this series of samples, the optical signature of arsenic site transfer upon activation annealings could be well understood because the PL measurements could be compared with extended x-ray absorption fine structure (EXAFS) measurements [5].

As we will see in the next chapter much work is still being done on the PL characterization of the optical signatures of the different dopants in HgCdTe. This work is done and will be continued within the PhD thesis of Frédérique Gemain.

Photoluminescence studies of arsenic-doped $Hg_{1-x}Cd_xTe$ epilayers

In this study, arsenic incorporation in HgCdTe epilayers has been achieved with a non-conventional radiofrequency plasma source during MBE growth and photoluminescence studies were carried out on those HgCdTe arsenic-doped samples. Measurements were done on the as-grown sample, after a n-type annealing to fill the Hg vacancies (as described in section 2.1.1) and after a 400^oC activation annealing under Hg pressure. A comparison with extended x-ray absorption fine structure (EXAFS) results allows us to assign the observed optical transitions to the Hg vacancies, As_2Te_3 glass and AsHg dopants. An optical signature of the arsenic site transfer upon activation annealing is found.

In-situ p-Type doping during MBE growth has been widely studied, because it is the key toward the realization of complex infrared detector heterostructures such as dual band sensors, hot detectors and p-on-n-devices [72, 73, 74, 75]. Arsenic is the most used impurity, because it has demonstrated very low diffusion properties into HgCdTe and also because the available purity and associated effusion technology meet today's requirements for MBE. Arsenic can thus be incorporated in levels ranging from 1.0 10^{16} at/cm^3 to 1.0 10^{19} at/cm^3, [76, 77] but the acceptor behavior can only be achieved after high temperature thermal activation. The activation ratio, usually deduced from secondary ion mass spectroscopy (SIMS) and Hall effect measurements, is generally found to be above 50% for a doping concentration below 1.0 10^{18} at/cm^3 and drops to a few percents when the doping level is increased above this limit [76, 77]. Despite all these efforts and progress, there are still many unknown aspects regarding this kind of doping. Two of the major uncertainties are the knowledge of the As incorporation site before and after thermal activation and the exact mechanism of activation. The commonly admitted scenario proposed by Berding and Sher [78] and Vydyanath [79] and refined by Schaake [80] Chandra et al. [81], and Shaw [82], assumes that arsenic is incorporated into the mercury lattice site during MBE growth under tellurium-rich conditions and that the high-temperature annealing enables a site transfer of the arsenic atoms, that would replace tellurium atoms. Photoluminescence (PL) measurements were interpreted using this model [83]. Recently, EXAFS investigations

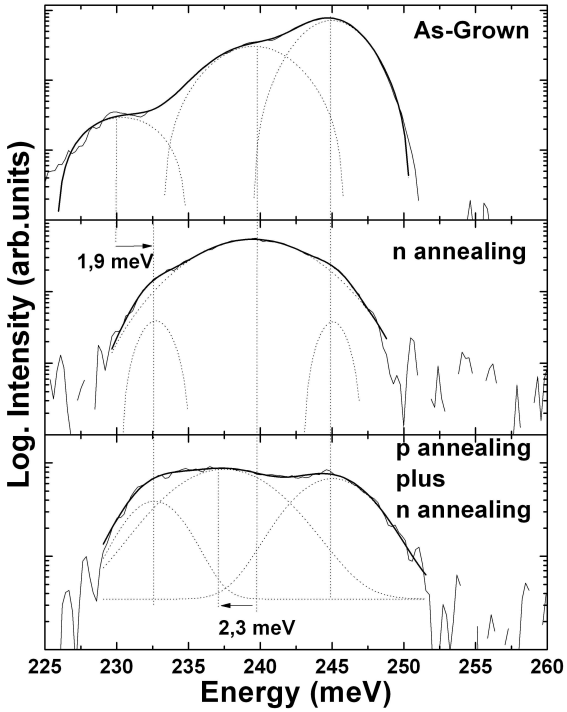

Figure 1.24: PL spectra at 2 K of the as-grown sample, after n-type annealing and after the p-type plus n-type annealing. The spectra were measured with a laser excitation power density of 20 W/cm^2.

reported by P. Ballet et al. [84] gave new insight on As site transfer upon thermal activation. It was shown that before p-type activation annealing, As incorporated atoms are shared between two structures: the donor complex As_2Te_3 and an acceptor complex: AsHg. The proportion between the two phases is approximately equal before thermal activation. After p-type annealing, the As_2Te_3 donor is dissociated. Part of the As from the As_2Te_3 glass enforces the active AsHg acceptor, the remainder occupies Hg sites: AsHg. The ratio of arsenic incorporated as AsHg acceptors to the arsenic substituting a mercury atom after thermal activation is 75/25, favouring p-type conduction. In this paragraph, the effect of As incorporation and post growth treatment is investigated by PL measurements. Excitation power and temperature dependent measurements allow us to identify the PL peaks and an optical signature of the site transfer found by EXAFS measurements is evidenced. The ionization energies of the dopant levels involved are determined.

The studied MCT layer was grown by MBE at the laboratory in the Riber 2300 chamber on a 20 mm X 25 mm CdZnTe (211) B single crystal substrate. The active layer is 7 μm thick with a cadmium content x of 0.3 confined between two wider-gap layers on a width of $\approx$0.3 μm. It is As doped with a level of 8.10^{16} at/cm^3 from secondary ion mass spectroscopy (SIMS) measurements [84]. After growth, in order to fill the Hg vacancies responsible of uncontrolled p-type doping, a low temperature (200^{o}C) annealing under saturating mercury pressure for 120 h was performed as described in paragraph 2.1.1. This treatment is called n-type annealing. As mentioned before, in order to control p-type doping, a high temperature annealing cycle is needed to transfer the incorporated As onto the proper sites [84]. In our case, after MBE growth, annealing at 400^{o}C for 1 h under saturated Hg pressure in a

Treatement	HE (meV)	ME (meV)	BE (meV)
As-grown	245	239	230.2
n-type annealing	245	239.5	232.1
p-type plus n-type annealing	245	237.2	232.3

Table 1.2: PL peak positions fir the As-doped sample as-grown, after n-type annealing and after p-type plus n-type annealing.

closed-space quartz ampoule is performed [78]. We call this treatment "p-type annealing". SIMS measurements were used to verify that the arsenic and cadmium profiles are similar for samples as-grown and annealed.

Fig. 1.24 shows the PL spectra, at low excitation density (20 W/cm^2) of the As doped MCT layer, as-grown, after n-type annealing and after p-type plus n-type annealing. The spectra were fitted using Gaussian curves to identify the different contributions. The different emission peaks identified are confirmed by excitation power and temperature-dependent measurements (cf. Fig 1.25 and Fig. 3). The positions of the PL peaks are summarized in Table 1.2. At low temperature, for the as-grown sample or after the annealing, the PL spectra are composed of three emission peaks: a high energy (HE), a middle energy (ME) and a low energy (LE) peak. The center energies and the relative intensities of the peaks change upon annealing. The as-grown PL spectrum is comprised of three emission peaks at 245 meV 239 meV and 230.2 meV respectively. The HE peak at 245 meV is also seen after n-type or after p-type plus n-type annealing. However, its relative intensity is strongly reduced after annealing. The position of the ME peak does not change (within the experimental uncertainty): it remains at 239 meV. However it dominates the spectrum. The LE peak shifts by 1.9 meV towards higher energy. After p annealing plus n annealing, the LE peak position is the same as after n annealing. However, the relative intensities of the LE peak strongly increases and the ME peak is shifted by 2.3 meV towards lower energies (CF. Fig. 1.24 and Table 1.2).

Fig. 1.25 presents the low temperature (2K) excitation power dependence of the PL spectra as well as the peak energies versus the excitation density. While the PL spectrum of the as-grown sample is dominated by the HE peak for all excitation densities, that of the n-type annealed sample is clearly dominated by the ME peak at 239.5 meV at low excitation density. After p-type plus n-type annealing, the spectrum is dominated by the LE peak (as seen in Fig. 1.24). In all cases, the HE peak corresponds to the band to band transition. This is confirmed by the temperature dependent measurements (cf. Fig. 1.26): For the as-grown sample, the peak energy increases with excitation density because of a band-filling effect. This band filling effect is less visible after annealing, probably because of the activation of dopants leading to a higher dopant-related density of states. After annealing, the ME peak and the LE peak clearly exhibit impurity related behaviours: they dominate the spectra at low excitation densities. Their relative intensity saturates at higher excitation densities when the band to band transition becomes more visible. Based on the EXAFS results by P. Ballet et al. [84] we are going to explain the evolution of peak positions observed in Fig. 1.24 upon annealing. Indeed, before p-type annealing, the As is distributed between As_2Te_3 donor complex and the AsHg acceptor. Before n-type annealing, the sample contains also a high density of Hg vacancies acceptors. Thus, for

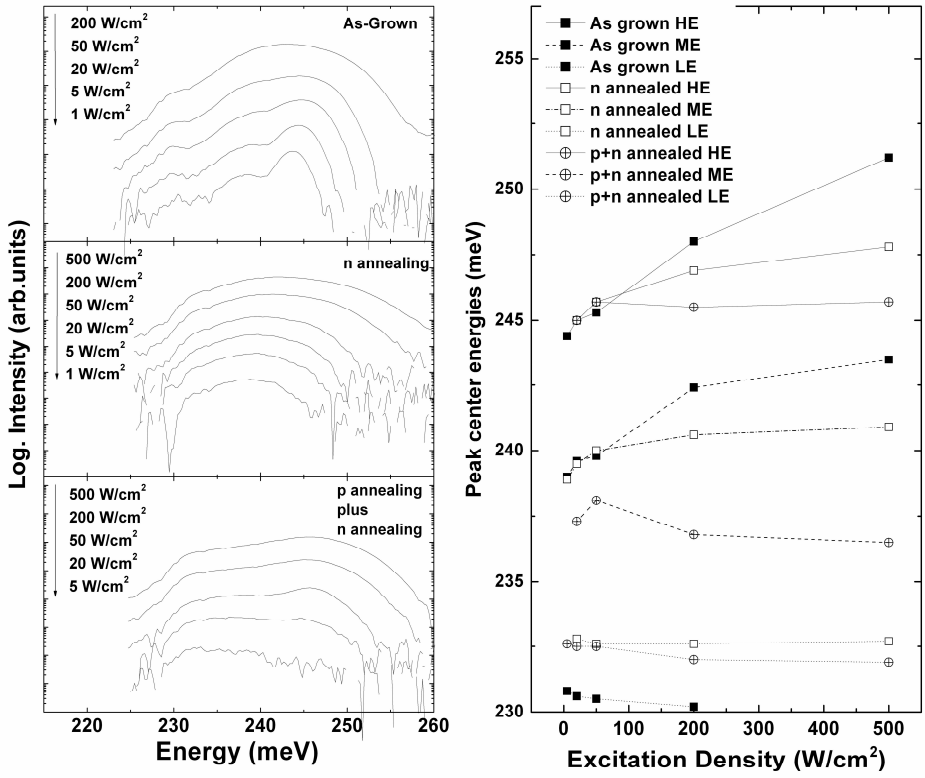

Figure 1.25: Excitation power dependence of the PL spectra at 2K of the sample as-grown sample, after n-annealing and after p-annealing plus n-annealing (left column). The excitation densities are given in the upper left corner of each graph.

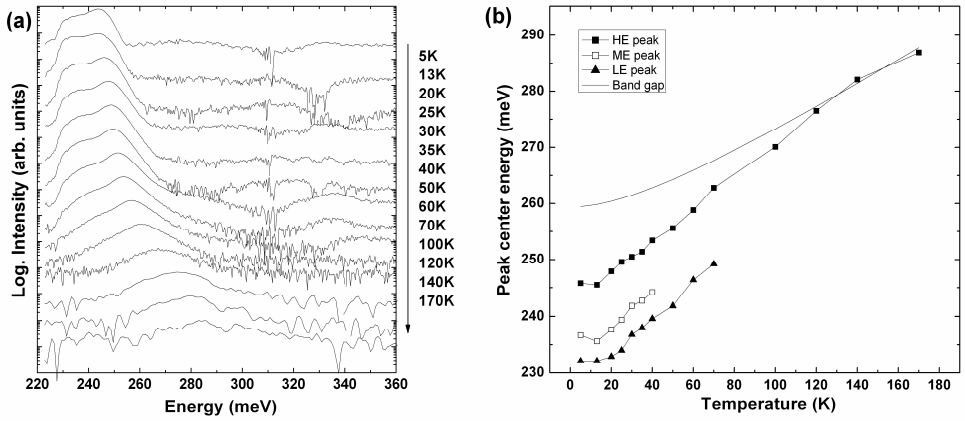

Figure 1.26: (a) PL spectra temperature dependence and (b) temperature dependence of the peak center energies after p plus n annealing.

the as-grown sample, the LE peak is related to Hg vacancies and the ME energy peak is due to As2Te3; after n-type annealing, the Hg vacancies being filled, the LE peak becomes AsHg related. This is the reason why a shift of the LE peak is observed. N-type annealing also seems to activate the As_2Te_3 donor complex as the relative intensity of the ME peak strongly increases. After p annealing, the As2Te3 donor complex is dissociated, the AsHg acceptor complex is strengthened and the donor AsHg is activated. This explains the strong increase of the relative intensity of the AsHg-related LE peak. After p-annealing, the ME peak is AsHg-related, which explains the energy shift of the ME peak after p annealing.

To summarize, for the as-grown sample, the LE peak is Hg vacancies related and the ME peak is As_2Te_3 related. After n-type annealing, the LE peak is AsHg-related and the ME peak is As_2Te_3 related. After p-type annealing, the LE peak is AsHg-related and the ME peak is AsHg-related. The ME peaks probably correspond to D^o-h transitions and the LE peaks to e-A^o transitions. These tentative assignments imply ionization energies of about 15 meV for the Hg vacancy acceptors, 12.8 meV for the acceptor complex AsHg, 5.5 meV for the donor complex As2Te3 and 7.8 meV for the donor AsHg. The ionization energies found for the Hg vacancy is close to the one of the two activation energies found in paragraph 2.1.1. It is also close to the reported values, measured by temperature Hall measurements [85]. The AsHg complex acceptor ionization energy is close to the reported values of the arsenic acceptor level ionization energies [86].

In Fig. 1.25, we notice that the D^o-h (ME) peaks show the same energy shift versus the excitation density as the HE band to band transitions. Thus the energy shifts observed are probably due to a valence band filling effect. This band filling effect is not seen after p-type annealing. We also note that the LE e-A ^{o} transition energies are constant as a function of the excitation density. Those energy shifts are related to the density of donor and acceptor states. Before p-type annealing, the density of acceptor states is low. Thus, the photo-generated holes saturate those acceptor states for a relatively low excitation density. For higher excitation densities they fill the valence band, leading to an increase of the band to band and D^o-h transition energies. After p-annealing, this band filling effect is not seen anymore because of a higher density of acceptor states. It seems that the density of donor states is always high enough not to observe the conduction band filling effect on the e-A^o transition Fig. 3(a) shows the PL spectra temperature dependence after p-type plus n-type annealing and Fig. 3(b) the peak energies and the theoretical band gap temperature dependence [87]. The HE peak, corresponding to the band to band emission is lower than the theoretical band gap energy between 2K and 130 K. This is certainly due to localization in Urbach tail states due to alloy fluctuations [88]. At higher temperatures, the peak energy follows the bandgap evolution. This confirms the attribution of this peak to the band to band transition. The ME peak attributed to a D^o-h transition disappears above 40 K, probably because of the ionization of the donor. The LE peak attributed to an e-A^o transition disappears at higher temperature, around 80 K, probably because of the ionization of the acceptor which has higher ionization energy than that of the donor. Similar behaviour is found for the as-grown and n-type annealed samples confirming the peak assignments.

This work on the optical signatures in MCT layers is being continued. As it will be seen in the next chapter, the Hg vacancy is being studied in detail by photoluminescence. The evolution of the arsenic complexes optical signatures with alloy composition is also being studied. A detailed characterization of those optical signatures will allow a better understanding of the dopant incorporation during different process under study such as

implantation, annealing,..

In this chapter I showed that I had the opportunity to study a large variety of material systems for light emission and light detection. In many cases those studies allowed a deep understanding of the relations between growth procedures and physical properties. I am now going to expose the projects I will be working on during the next few years. The main one is very device oriented. Indeed, my experience in the field of wide band-gap semiconductors led me to imagine new structures using field effect to improve solid state UV emission.

Chapter 2

Dopants Optical Characterizations and new design of UV LEDs

I am going to present in this chapter the main projects I am planning to work on in the next few years. The first one is the continuation of what was begun with the optical characterizations of the HgCdTe epilayers. In this project, various types of materials used for solar cells or IR detectors will be characterized. The goal is to find clear optical signatures of defects or dopants, to understand the conditions for the apparition of those defects and to correlate it with the detector performances. The approach consisting in studying the optical properties evolution of each material allows an understanding of how changes are likely to occur during the device fabrication. This work started with the PhD thesis of Frédérique Gemain. It will concern HgCdTe epilayers but also dopant optical signatures in CdS layers grown by Chemical bath deposition (CBD) and close space sublimation (CSS) as well as dopants optical signatures in CIGS (CuInGaSe) layers grown by CBD for solar cells fabrication.

The second project proposes an entirely new solution to cope with this problem of UV LEDS fabrication. The idea is to bypass the problem of p-type doping of wide band-gap semiconductors. My approach mainly relies on field effect carrier injection towards the active region through the use of a gate. This project was selected to get the "Challenge Innovation" grant of the CEA-Leti.

2.1 Optical signatures studies of dopants in HgCdTe and CdS

I am first going to present the projects concerning the optical signatures in HgCdTe. I will then present the preliminary results obtained on CdS polycrystalline films used for solar cells fabrications. Those studies show the interest of this approach for the optimization of the technological steps in device fabrication.

2.1.1 Photoluminescence studies of Hg vacancies-doped $Hg_{1-x}Cd_xTe$ epilayers

As seen in paragraph 1.4.2, we already studied the optical signatures of arsenic complexes in HgCdTe for a cadmium composition of about 30%. We are currently studing the evolution of those optical signatures with cadmium composition. Indeed, new generation of devices based

on P/N junction requires a better knowledge of doping properties, particularly extrinsic p-type doping [89].

However, the control of extrinsic p-type doping is made difficult by native defects in the material like mercury (Hg) vacancies. The concentration of these intrinsic acceptor impurities in as-grown liquid phase epitaxy (LPE) samples was found to be of about 10^{18}cm^{-3} by Vydyanath et al. [90, 91] at T$\succ$300^{o}C. Nevertheless, the energy levels related to those acceptors are still not well known. The Hg vacancy is a double acceptor defect with two levels at different ionization energies. However, up to date, only one emission peak at about 15 meV lower than the band to band emission was seen in literature by PL measurements and identified to be potentially related to Hg vacancies [92, 93, 94]. Also, only one acceptor activation energy of about 15 meV is usually measured in literature by temperature-dependent Hall measurements [85, 95].

To illustrate the kind of studies that are under way I present here preliminary results we obtained with Frédérique Gemain on non intentionally doped HgCdTe epilayers grown by liquid phase epitaxy (LPE). These films were post annealed under different conditions: a p-type annealing was used to reinforce the mercury vacancy concentration and a n-type annealing under saturated Hg atmosphere was used to fill the mercury vacancies. We try to use comparisons between the PL and Hall effect measurements to identify the mercury vacancy optical signature.

Temperature-dependent Hall data from vacancy-doped HgCdTe with 0.2-0.3 mole fraction Cd typically shows hole freeze out dominated by a single ionization energy of about 15 meV [85, 96, 95]. Hunter et al. also identified an emission peak about 15 meV lower than the band-to-band emission in PL measurements, potentially related to Hg vacancies [92].

The vacancy is created by removing the cation with its two bonding electrons. This leaves place for two electrons in the dangling bond orbitals surrounding the vacancy, so the vacancy should be a double acceptor with two levels at different ionization energies. Cooper et al. [97] propose that the vacancies are negative-U centers with inverted energy levels as shown in figure 2.2. This would be due to the fact that Jahn-Teller stabilization overcomes the repulsive interaction between electrons. Cooper et al. [97] propose in the conclusion of their article the use of Photo-Deep level transient spectroscopy (DLTS) to reveal the second acceptor level by creating a non-equilibrium population. Our PL measurements on LPE grown samples show that we possibly identified the optical signatures related to the two acceptor levels related to Hg vacancies.

The density of the Hg vacancies in HgCdTe is easily adjusted by annealing at various temperatures in vaccum. The concentration of these intrinsic acceptor impurities in samples grown by liquid phase epitaxy (LPE) at 480^{o}C is supposed to be of about 5.10^{17}cm^{-3} according to Vydyanath et al. [90]. We measure for as-grown samples a hole concentration of 8.10^{16}cm^{-3} (cf. Table 2.1). The hole concentrations measured by Hall effect at 77 K after different annealing temperatures are summed up in table 2.1.

For PL measurements, the studied MCT layer was grown by liquid phase epitaxy (LPE) at 480^{o}C. The active layer is 9 μm thick with a cadmium concentration of 32.7% corresponding to a cut-off wavelength of 3.75 μm at room temperature. Our p-type annealing is a 4 hour annealing in vaccum at a given temperature. To see the effect of the annealing temperature, three pieces of the same sample were p-type annealed at 270^{o}C, 300^{o}C or 330^{o}C. Another piece was n-type annealed. For n-type annealing, the layer is heated under a saturated mercury atmosphere for 5 days at 200^{o}C.

Modulated PL measurements with a continuous-scan FTIR spectrometer between 2K

and 300K were carried out at the CNRS laboratory in Meudon. The setup is the same one as the one described in paragraph 1.4.2.

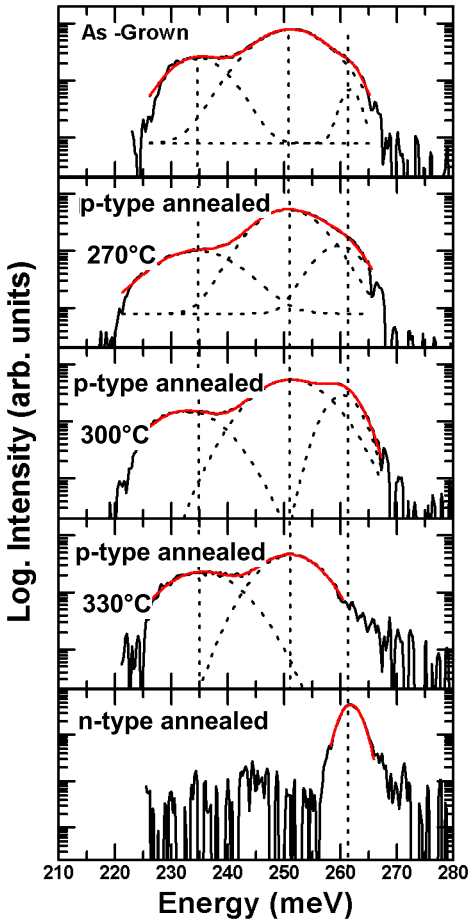

Figure 2.1: Comparison of the PL spectra at 2K for an excitation density of 20 W/cm^2 between the as grown sample, after p-type annealing (270^o, 300^{o}C, 330^{o}C), and after n-type annealing

Figure 2.1 shows the PL spectra of the MCT layer, as-grown, after the p-type annealings and after the n-type annealing. The measurements were done at 5K for an excitation density of 20 W/cm^2. The spectra were fitted using Gaussian curves to identify the different contributions. The PL spectrum of the as-grown sample is composed of three emission peaks at 261.8 meV, 251.1 meV and 234.5 meV respectively. Those three peaks will be named High-Energy (HE) peak, Medium-Energy (ME) peak and Low-Energy (LE) peak. The HE peak remaining after n-anneling and bearly visible for the as-grown sample and after a p-type annealing at 330^{o}C is attributed to the band to band recombination. This will be confirmed by the temperature dependent PL measurements shown later. The energy difference between the HE and the ME peak is of 10.5 meV. The energy difference between the HE and the LE peak is of 27.3 meV. In addition, the LE peak relative intensity increases with p-type annealing, whereas this peak disappears after n-type annealing together with

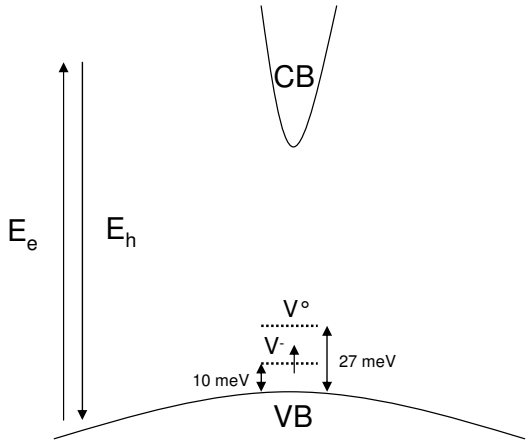

Figure 2.2: Energy levels of the mercury vacancies for a model where the Jahn-Teller stabilization in the V^- configuration overcomes the repulsive interaction between electrons.

the ME peak. Thus, the LE peak is attributed to an eA^o recombination between an electron in the conduction band and the V^o state of the mercury vacancies. The ME peak can be attributed to an eA^- recombination between an electron in the conduction band and the V^- state of the mercury vacancies. The eA^- recombination would lie at a higher energy than the eA^o recombination because the V^- state of the mercury vacancies would lie at a lower energy (closer to the valence band) than the V^o state of the mercury vacancies because of the negative-U properties of the Hg vacancies described in ref [97] and discussed earlier (cf. Fig. 2.2). Thus it would be possible to measure the energy level of the V^- state by PL measurements whereas it is not seen by temperature dependent Hall effect. Indeed, this state can be photogenerated in the case of PL measurements.

Figure 2.3 presents the temperature dependence of the peak energies between 2K and 300K for the as grown sample, the 330^{o}C p-type annealed sample and the n-type annealed sample. The HE peaks located at 261.8 meV at low temperature presents the same temperature-dependent behavior for the as-grown sample, the p-type annealed sample and the n-type annealed sample. The PL emission of this HE peak is lower than the theoretical band gap energy between 2K and 80K because of localization in Urbach tail states due to alloy fluctuations [88]. For higher temperatures, the temperature dependence of the PL peaks follows the variation of the theoretical band gap. This confirms the attribution of this emission to a band-to-band transition.

Note that in the case of the p-annealed sample at 330^{o}C, the HE peak is not seen below 40K (as seen in figure 2.1). This is certainly due to a transfer of all the photo-generated carriers towards the Vacancy levels. Above 40K, part of the vacancies being ionized, the band to band transition can be seen.

Our PL measurements tend to show that the V^o state and the V^- states could be identified. In our sample, the V^o state would have a 27 meV activation energy and the V^- state a 10 meV activation energy. This would explain why the V^- activation energy activation energy is never measured by Hall effect temperature dependence. However an activation energy of 15 meV of the V^o state is usually measured in literature [96, 95, 98]. Thus we need to confirm our PL results by temperature dependent Hall effect measurements. The difference in ionization energies compared to what is found in literature could be due

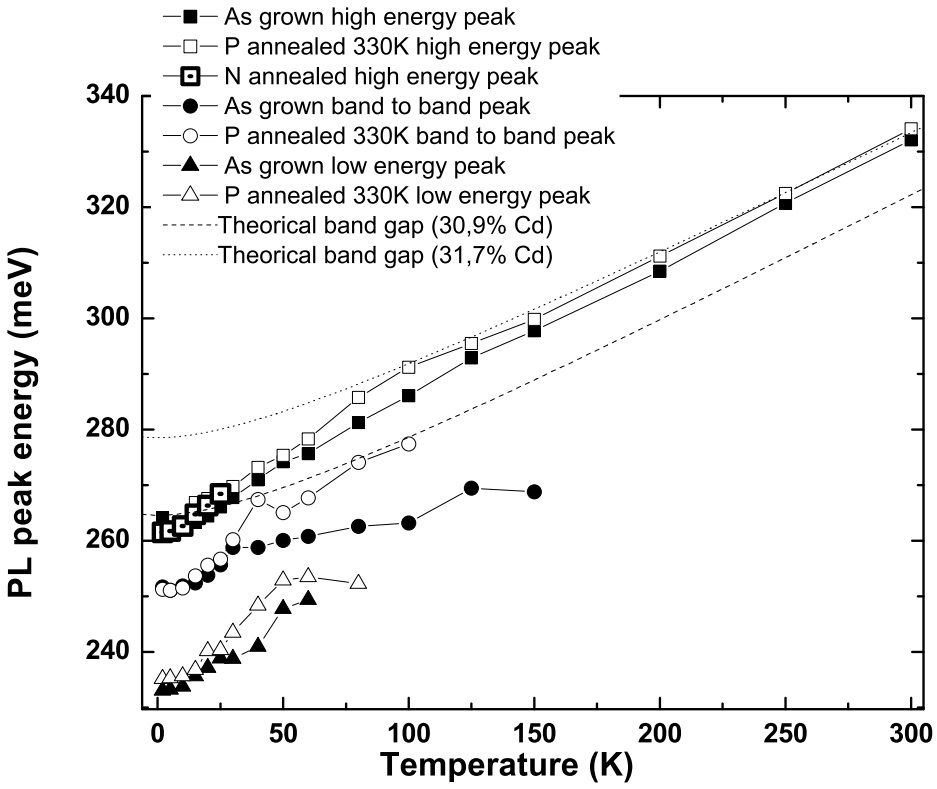

Figure 2.3: Temperature dependence of the PL peak energies of the as-grown sample, after p-type annealing at 330^oC and after n-type annealing.

to a higher cadmium content in our case (33%) whereas samples with a cadmium content with 0.2-0.3 mole fraction were mostly measured. Indeed we are also planning to do the same measurements on samples with different composition. Our studies could lead to a clear identification of the Hg vacancies related acceptor states.

A detailed comparison with temperature dependent Hall measurements is also under way.

Other studies with arsenic doped and indium doped samples are also under way. The identification of the optical signature of the Hg vacancies in HgCdTe will also help for the identification of optical signatures in intentionally doped samples. Those studies will contribute to the optimization of the technological steps of the IR detectors.

2.1.2 Photoluminescence studies of CdS layers for solar cells

Polycrystalline CdS films are used as n-type window layers in p-type CdTe/n-type CdS thin film heterojunction solar cells. A range of CdS deposition methods have been used for the preparation of efficient devices. However, two thin film preparation techniques dominate in this context: chemical bath deposition (CBD) and close-spaced sublimation (CSS). The highest efficiency small area solar cell devices have been achieved using n-type CdS layers grown by CBD and p-type CdTe grown by CBD having record conversion efficiencies of 16.5%. [99]. The CSS technique allows large area deposition of CdS and CdTe films using

Sample	Doping level (cm^{-3})
As-grown	$p = 8.05 \cdot 10^{16}$
p-type annealed 270^{o}C 4h	$p = 1.5 \cdot 10^{16}$
p-type annealed 300^{o}C 4h	$p = 2.3 \cdot 10^{16}$
p-type annealed 330^{o}C 4h	$p = 3.6 \cdot 10^{16}$
n-type annealed 200^{o}C 5d	$n = 1.05 \cdot 10^{16}$

Table 2.1: Doping measurements by Hall effect of the as-grown sample, after p-type annealing at different temperatures and after n-type annealing.

high deposition rates.

CdS and CdTe are grown at the laboratory by CBD and CSS for solar applications. Other materials are also studied such as CIGS (CuInGaSe) to fabricate solar cells using p-type CIGS/n-type CdS heterojunctions. Photoluminescence studies of those materials would be very useful for the optimization of the growth of the heterojunction. We started to study the changes in CdS optical properties of CSS and CBD grown layers subsequently treated by annealing in air, in Argon or under vaccum. PL probes optically active recombination centers in CdS. Some of these will contribute to losses in photocurrent of solar cell devices due to optical absorption in the CdS window layer. PL can also provide information about impurity and defect centers which act as recombination centers for charge carriers which also reduces the PV conversion efficiency. It is known that the CdS material is highly compensated with comparable densities of shallow donor and deep acceptor states. Therefore, a portion of carriers, photogenerated in the n-CdS window layer, does not create photocurrent due to radiative and nonradiative recombination. In many cases solar cell device optimization is done empirically rather than systematically. Typically, this involves thinning the CdS in order to minimize absorption, reducing pin hole,.. The approach consisting in studying the optical properties changes of each material allows an understanding of how changes are likely to occur during solar cell preparation.

CdS layers can be grown at the laboratory under various conditions using CBD or CSS. In our preliminary work, we focused on PL measurement performed on polycrystalline CdS films and tried to observe the evolution of PL features according to deposition technique and postdeposition treatments. CdS is naturally n-type because of the presence of sulfur vacancies (Vs^{2-}). In most of the observed samples a DAP involving the sulfur vacancies could be identified. It also seems that annealing of CBD samples in Argon atmosphere favors the occurrence of interstitial cadmium defects (I^+_{Cd})and annealing in air favors interstitial sulfur defects (I^-_S). The comparison of CBD samples annealed in air and CSS samples grown under oxygen pressure suggests the identification of the optical signature of interstitial oxygen (O^-_S).

CdS film deposition

CdS CBD growth uses the following reaction:

$$Cd(NH_3)_4^{2+} + SC(NH_2)_2 + 2OH^- = CdS + CH_2N_2 + 4NH_3 + 2H_2O$$

The bath is held at a temperature of about 80^{o}C for a deposition time of about 45 min and the growth is done on a borosilicate glass.

For CdS CSS growth, the growth is done with a substrate temperature T_{sub}=450^{o}C and

a source temperature T_{source}=650°C. The distance between the source and the substrate is of 6mm. The growth can occur under argon or oxygen pressure.

Preliminary results

Figure 2.4 compares the PL spectra for a CBD grown sample as-grown and after annealing under Argon atmosphere (≈250 mbar) at 450°C for 30 min. The large band around 1.6 eV and related to sulfur vacancies [100, 101, 102] is seen for both samples. For the as-grown samples, a band centered at 2.3 eV certainly related to the presence of interstitial sulfur [100, 101] atoms is seen whereas a band at about 2 eV related to interstitial cadmium atoms [103, 104] is seen in the annealed sample under argon pressure. The disappearance of the interstitial sulfur related emission could be due to the evaporation of sulfur atoms during annealing as suggested by Aguilar-Hernandez et al. [100].

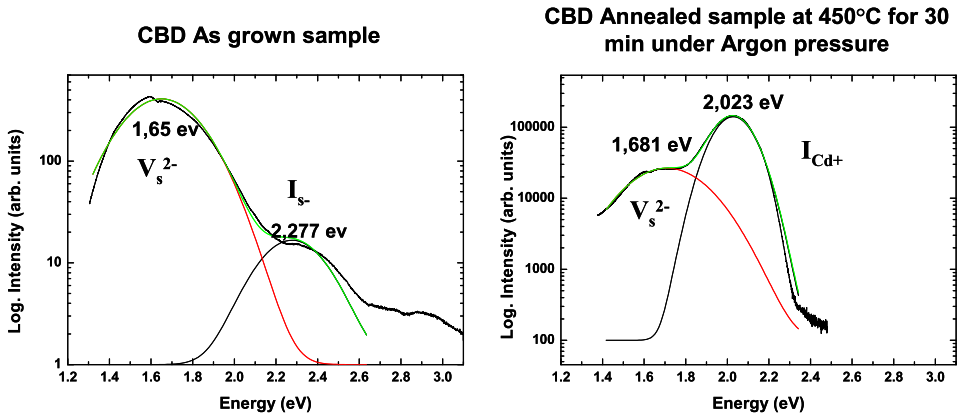

Figure 2.4: Comparison of the PL spectra between the CBD as-grown CdS sample and after annealing at 450°C under Argon atmosphere (≈250 mbar) for 30 minutes.

Figure 2.5 presents the temperature dependence of the PL peaks of the annealed CBD sample under argon atmosphere. The high energy (HE) peak possibly related to interstitial cadmium atoms follows the CdS gap dependence. This peak is probably an eA^o transition between an electron in the conduction band and the acceptor I^+_{Cd} [104].

The low energy (LE) peak attributed to a DAP transition with sulfur vacancies as donors [100, 101, 102] follows the band gap evolution between 4K and 150K. Above 170K the LE peak follows again the band gap evolution but at 69 meV higher than the initial evolution. Thus we possibly observe here a transition from a DAP transition to an eA^o transition. The ionization energy of the Vs^{2-} states would be of 69 meV. Note that this temperature dependence of the Vs^{2-} peak center energy is systematically observed for the CDB grown samples (also for the as grown sample and for the sample annealed in air).

Figure 2.6 compares the PL spectra between the CBD as-grown CdS sample and after annealing in air at 450° for 1 hour. The evolution of the PL features are considerably different compared to annealing under Argon pressure: the main PL peak after annealing in air is the peak at 2.3 eV, certainly related to interstitial sulfur atoms [100, 101]. The peak

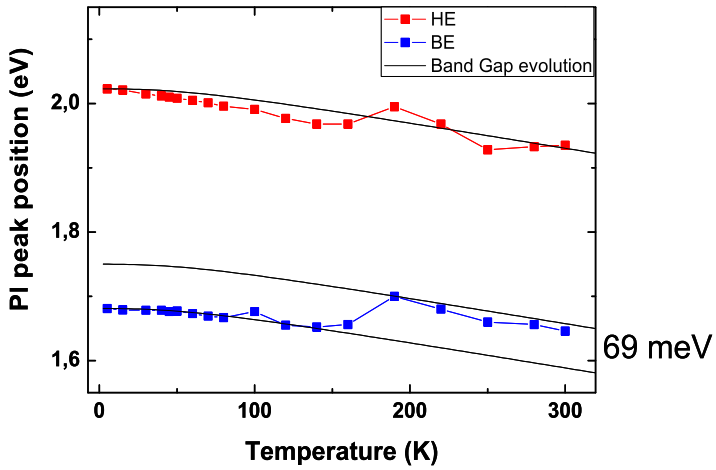

Figure 2.5: Evolution of the PL peak energies with temperature for the CBD sample annealed under Argon pressure.

related to sulfur vacancies Vs^{2-} is also seen. A peak is also needed at 2.22 eV to correctly fit the data. This peak is also seen for the CSS grown sample under oxygen atmosphere (cf. Fig. 2.7). As this peak is close in energy to the one attributed to interstitial sulfur and as oxygen is just above sulfur in the periodical table, we suggest that this peak at 2.22 eV is related to interstitial oxygen.

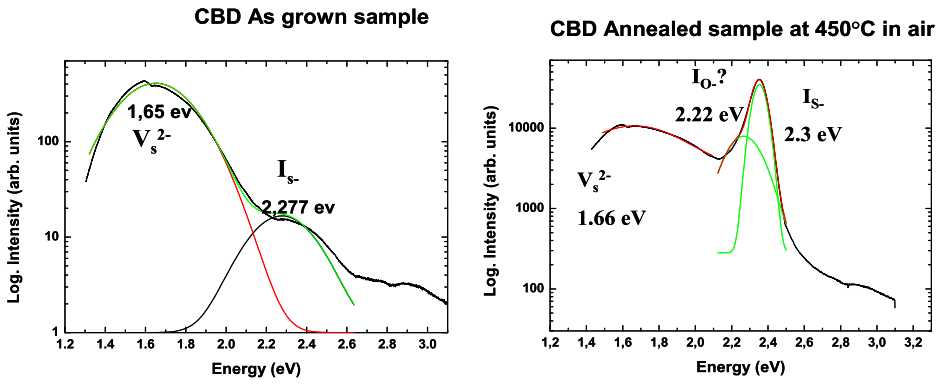

Figure 2.6: Comparison of the PL spectra between the CBD as-grown CdS sample and after annealing in air at 450^o for 1 hour.

Figure 2.7 compares the PL spectra between the CSS CdS samples grown under vacuum and under oxygen atmosphere. An excitonic D^oX peak is seen for the CSS sample grown

under vacuum. This accesses the better quality of the material grown by CSS compared to CBD growth. In the case of the sample grown under vacuum, the main feature is the peak at 2.02 eV certainly due to interstitial cadmium atoms. In the case of CSS growth under oxygen pressure, the main feature is the peak at 2.215 eV. Thus the comparison of the PL spectra between CSS grown samples under vacuum and under oxygen pressure seems to confirm our attribution of the peak around 2.22 eV to the presence of interstitial oxygen defects.

Another peak is also needed at 2.15 eV to correctly fit the data. The energy difference of this peak with the presumed I_O^- peak is of 70 meV which is the donor energy of the sulfur vacancies we determined from the temperature dependent study presented in figure 2.5. Thus the peak at 2.15 eV is possibly a DAP transition involving the sulfur vacancies as donors and the interstitial oxygen as acceptors.

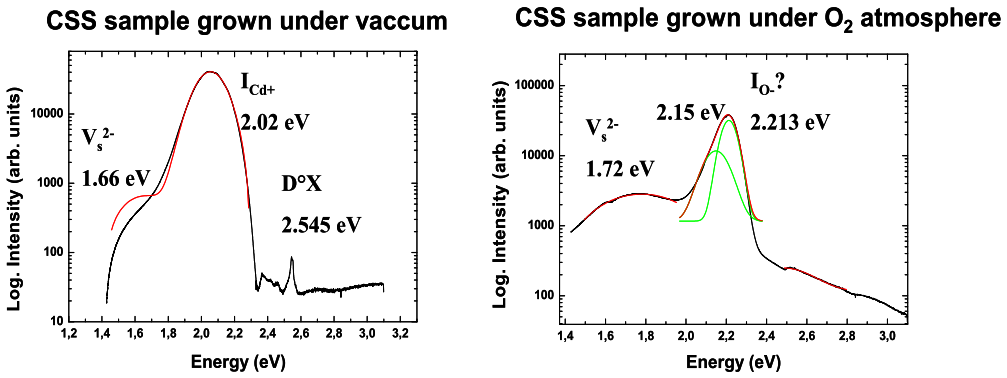

Figure 2.7: Comparison of the PL spectra between the CSS CdS samples grown under vacuum and under oxygen atmosphere.

For the moment the presented PL studies are preliminary results that need more studies for confirmation. However, those studies show the interest of PL studies for a deeper understanding of defect formation processes during growth annealing procedures in the CdS layers used for solar cells fabrication.

I would like to enlarge this approach to the different material systems used for solar cells fabrication. The goal would be to correlate the defects optical signatures with the device performances.

2.2 Field Effect UV Optical Emitters

The main problem in fabricating a ZnO UV emitter remains the difficulty of achieving reliable p-type doping, which is necessary for the formation of p-n homojunctions. For GaN, even if p-type doping has been achieved, allowing for the fabrication of blue LEDs based on this material, any improvement would certainly boost their efficiency for solid state lighting applications. For UV LEDs, $Al_{1-x}Ga_xN$ alloys are necessary as confinement barriers and the difficulty to p-dope the alloy increases with Al composition.

In this project I propose an entirely new solution to cope with this problem. My approach relies on

1. devising "hybrid" junctions associating different wide band gap semiconductors acting separately as efficient hole and electron injectors, and,

2. field effect carrier injection towards the active region through the use of a gate in order to achieve efficient solid state UV emission.

Among the available wide band gap materials, different "hybrid" semiconductor couples will be tested, with a focus on III-V nitrides and oxides based compounds. Currently, the III-V nitrides offer the most viable approach towards the realization of high-efficiency UV optical emitters based on semiconductors; but these require $Al_{1-x}Ga_xN$ alloy layers to reach shorter wavelengths and p-type doping of the alloys has proved to be quasi impossible. ZnO and related alloys have very strong excitonic emission and, as such, are also promising materials for UV light emission. Here as well, $Zn_{1-x}Mg_xO$ alloys are required to reach shorter emission wavelength and it has not yet been proved that these alloys could be doped p-type. Since in these materials p-type doping is the problem, I propose to use a gate to perform field effect hole injection from a p-type semiconductor into a different n-type material. The selection of adequate materials will be done according to their band offset as measured by means of X-ray photoelectron spectroscopy (XPS). Different gate geometries will be tried to optimize the output of the device. In particular the possibility of injecting holes by means of p-type NWS or the possibility of achieving field effect injection into n-type NWs will also be tested. This approach based on entirely new physical and technological concepts will lead to solid state sources emitting deeper in the UV than the presently available LEDs, with greater efficiencies compatible with a wide range of applications.

2.2.1 State of the Art

The direct band-gap III-V nitride semiconductor family and its alloys are currently the most promising semiconductors for solid state lighting through the visible and ultra-violet (UV) range[105]. High efficiency light-emitting diodes (LEDs) [106, 107], and even short-wavelength lasers were fabricated [107, 108]. Those device fabrications are possible in the case of III-V nitride based semiconductors, because efficient p-type doping of GaN and GaInN was realized in the early 1990s using Mg doping [109]. However in the case of III-V nitrides materials, a problem that has persisted since the early 1990s and is becoming increasingly troublesome when going to shorter wavelengths is the high resistivity of p-type GaN and AlGaN layers. The activation energy E_A of the most commonly used acceptor dopant (Mg) in GaN is $\approx$ 200 meV [110], several times the thermal energy k_BT at room temperature (where k_B is the Bolzmann constant, and T is temperature). The activation energy of acceptors increases with the band gap, reaching $E_A \approx 630$ meV in AlN [107]. Thus, the thermal activation of holes is highly inefficient at room temperature for GaN and becomes increasingly problematic for higher-band-gap AlGaN and AlN layers.

ZnO based materials would be another interesting family for UV and deep UV solid state emission: ZnO has a direct band gap of 3.37 eV at room temperature and a high free-exciton binding energy of 60 meV as well as high likelihood of efficient excitonic optical transitions at elevated temperature [111]. Compared to AlGaInN systems, ZnO is another high potential system for UV emission because of its resistance to high-energy radiation, availability of high-quality substrates (leading to simple vertical LEDs geometries), and the ability to

use wet chemical etching for mesa formation if other substrates are employed. Moreover, by alloing with the dielectric MgO, $Zn_{1-x}Mg_xO$ compounds can be formed with larger band gaps, but the amount of Mg incorporated is limited in practice by phase separation [112, 113]. The main difficulty in fabricating an all-ZnO UV emitter remains the lack of a process to achieve reliable p-type doping, which is necessary for the formation of homojunction p-n diodes [114, 115, 116, 117]. Tsukazaki et al. studied nitrogen-doped ZnO p-i-n homojunction structure on (0 0 0 1) $ScAlMgO_4$ grown by laser molecular epitaxy [118]. Ryu et al. demonstrated electroluminescence (EL) in (Zn,Be)O/ZnO-based heterostructures in which the p-type layer was doped with arsenic [119]. Lim et al. have made a phosphorus-doped p-n homojunction ZnO LED on sapphire by RF sputtering [120]. Jiao et al. have demonstrated a ZnO p-n junction LED on a-plane Al_2O_3 substrate by plasma-assisted molecular beam epitaxy [121]. Ip et al. showed rectifying behavior in pulsed-laser-deposited ZnO/ZnMgO heterojunctions in which the p-type ZnMgO was doped with phosphorus [122]. However, much more research is needed on all aspects of ZnO device and material technology. In addition, in the case of ZnO based LEDs, it is important to ensure that the observed band edge emission is actually due to p-n junction carrier injection. There is a long history of observation of small band-edge peaks in the EL spectra of ZnO material-insulator-(n type) semiconductor structures due to holes created by impact ionization during biasing [123].

To overcome the limitations of p-type doping in ZnO, p/n hybrid junctions were recently envisaged. Mostly p-type GaN/n-type ZnO hybrid junctions were realized [124, 125, 126, 127, 128]. Recently, ZnO nanopillars were used to improve the light outcoupling from the LED structures [129]; p/n hybrid junctions were also realized using p-type NiO/ n-type ZnO [130, 131, 132, 133] or p-type Cu_2O/n-type ZnO [134] . A NiO/ZnO light emitting diode could even be realized [130]. I think that ZnTe could also be an interesting candidate to realize p/n hybrid junctions using n-type ZnO: ZnTe has a wide band gap of 2.3 eV at room temperature and it is possible to p-dope it to a level of 10^{20} acceptors/cm^3 [135]. Fabrication of n-native oxide/p-ZnTe Heterojunctions were realized [136] as well as ZnO/ZnTe nanocone heterojunctions [137]. However, the potential of this kind of heterojunction for solid-state UV emission was not fully explored.

Regarding the other above cited heterojunctions, some interesting results have been obtained regarding UV emission. However, the fabrication of efficient hybrid junctions has not been demonstrated yet. Thus the most efficient LEDs remain the blue GaInN nitride-based structures and there is a lack of structures for deeper UV emission.

Field effect hole injection. As efficient p-type doing of wide band gap semiconductors is not possible yet I propose to use field effect for hole injection. This is a totally new way for injecting carriers in a wide band-gap semiconductor. To my knowledge, the only successful contribution where an electric field was used for carrier injection was recently reported by Simon et al. [52]. They performed Polarization-Induced Hole Doping in wide-bandgap uniaxial semiconductor heterostructures. They use the fact that AlGaN alloy has higher polarization than GaN, so that the dipole strength increases with the Al composition. When the composition of a layer is graded with an increasing Al mole fraction, a net unbalanced bound polarization appears creating a built in electric field. This electric field ionizes the deep acceptors. This is an illustration that shows how an internal electric field could be used to induce hole injection. In this project an electric field will also be used to induce hole injection. However in this approach the electric field is used to extract the holes from another semiconductor. This electric field will be produced and controlled by a gate voltage.

It will induce a depleted region in the wide band gap n-type material. The holes will be injected in this depleted region from a p-type material.

2.2.2 Proposed Structures and Objectives.

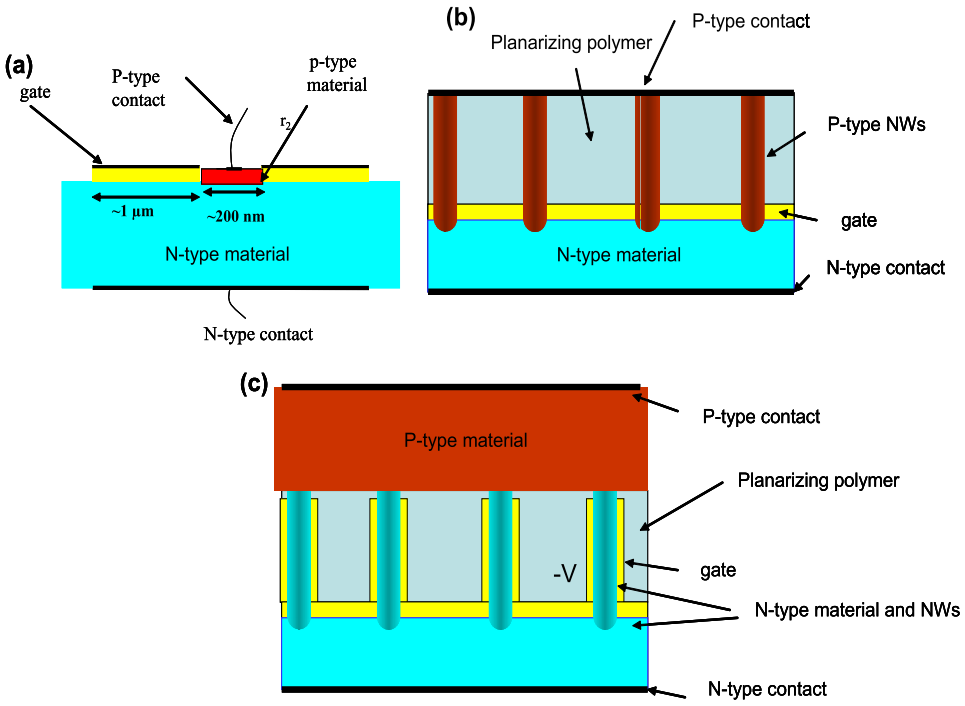

Figure 2.8: Different proposed structures for field effect hole injection into a wide band-gap semiconductor. (a) processed 2D p/n hybrid junction (b) p-type NWs used as hole injectors (c) Field effect injection into n-type NWs.

To achieve field effect hole injection into a wide band-gap n-type semiconductor, structures based on p/n hybrid junctions will be designed. Two approaches are proposed. The first approach (top-down) is based on the growth and subsequent processing 2D p/n heterojunctions. A second approach (bottom-up), relying on NWs offers the possibility to fabricate optimized structures from the point of view of light extraction as well as from the point of view of field effect geometry. In this second approach, p-type NWs can be used as hole injectors into a wide band-gap n-type 2D layer (Fig. 2.8(b)) or field-effect hole injection can be induced into n-type wide band-gap NWs (Fig. 2.8(c)).

Fig. 2.9 presents a scheme of a structure illustrating the proposed mechanism for hole injection in a wide band-gap n-type semiconductor. The structure presented in Fig. 2.9 corresponds to the one that was simulated to evaluate the pertinence of this approach. For this structure, a ring shaped gate of 1μm diameter with a center opening of about 200 nm is deposited on a n-type wide band gap semiconductor (ZnO, ZnMgO, GaAlN) and around a p-type material. Thus, into the gate aperture, there is a p-type material and a p-type

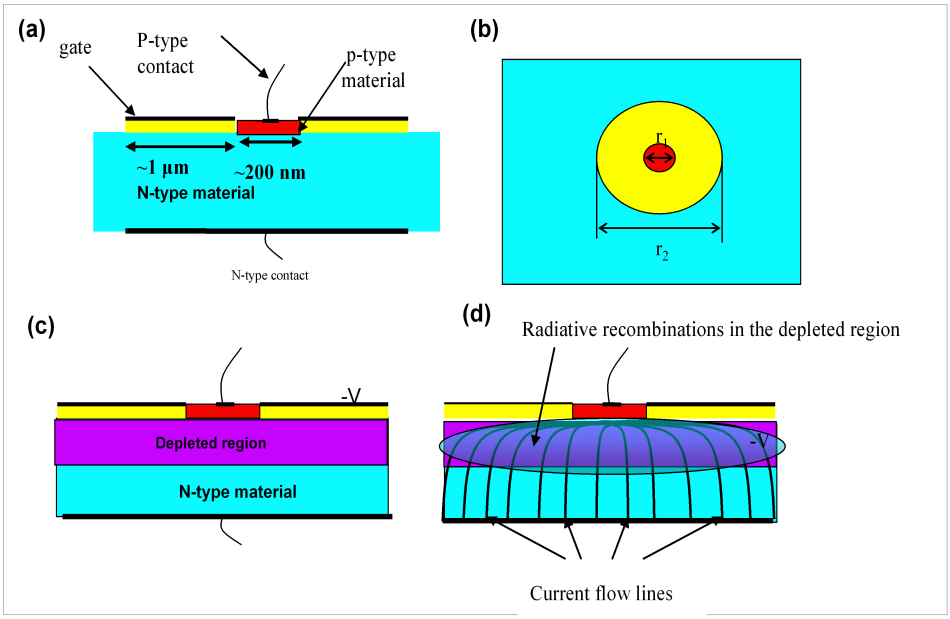

Figure 2.9: (a) Side view of a field effect structure. (b) Top view of the structure. (c) Formation of a depleted region when applying a negative tension on the gate. (d) Radiative recombinations in the depleted region when applying a tension between the anode and the cathode.

contact taken on this material. An n-type contact is taken on the back side or into the n-type material at a certain depth below the surface. The p-type material is just a hole injector and the radiative recombinations will be forced to occur into the n-type material because of the field effect injection. Indeed, when a negative tension is applied to the gate (Fig. 2.9(c)), a depleted region is formed below the surface. If the doping level in the n-type material is low and the gate voltage high enough, this depleted region can even be an inverted region into which holes can be injected when a tension is applied between the anode and the cathode. Radiative recombinations occur in this depleted region (Fig. 2.9(d)) and the energy of the emitted photons correspond to the n-type material band-gap energy.

This structure was simulated (Fig. 2.10). The detail of the structure used for this simulation is presented in Fig. 2.10(a). Axial revolution symmetry was used. The p-type material under the anode is p-doped GaN with a hole concentration of $5.10^{17}/cm^3$. The n-type material is ZnO with an electron concentration of $10^{18}/cm^2$. ZnO and GaN were used because their properties and band alignment are well known [138]. Figure 2.10(b) shows the band energies below the surface and Fig. 2.10(c) a cartography of the radiative recombination rate in the structure when a gate voltage of -5 V is applied and a tension of 5V is applied between the anode and the cathode. Quantum internal efficiency up to 30% is calculated in this configuration. The effect of gate voltage is seen in figure 2.10(d)

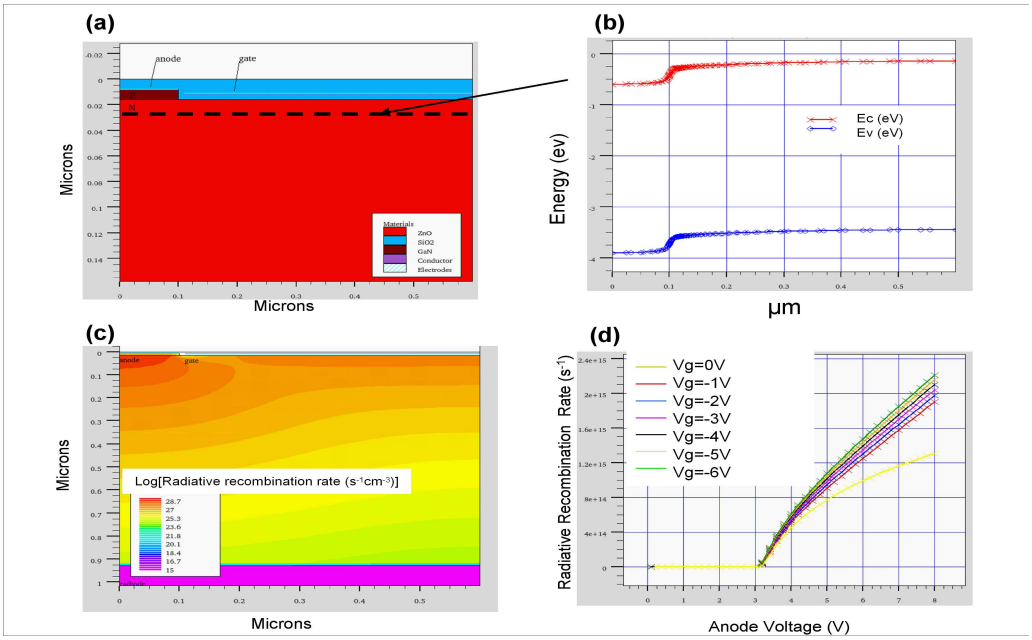

Figure 2.10: (a) Scheme of the structure used for simulation. The p-type material is GaN with a hole concentration of 5. $10^{17}/\text{cm}^3$. The n-type material is ZnO with an electron concentration of $10^{18}/\text{cm}^3$. The ZnO thickness is of 1μm but for clarity reasons in this representation we zoomed close to the surface. The p-type contact (anode) is taken on top of the p-type material. The n-type contact (cathode) is taken on the back side. (b) Conduction band energy (Ec) and valence band energy (Ev) below the surface, along the doted line in scheme (a). (c) Radiative recombination rate in the structure when a tension of -5 V is applied to the gate and when a tension of 5V is applied.
(d) Radiative recombination rate *vs* anode voltage for different gate voltages.

where an increase of the radiative recombination rate is clearly seen when the gate voltage is increased. If this simulation can be experimentally verified, this approach opens the way to deep UV emission with the use of ZnMgO or AlGaN alloys instead of ZnO as n-type materials.

However the fabrication of a planar structure as in Fig. 2.8(a) is complex. In addition to the challenging task of growing a high quality p/n planar hybrid junction, the process involves many steps as shown in figure 2.11 where an exemple of processing steps is given for a ZnTe/ZnO hybrid junction.

The 2D structure could be optimized by the use of NWs. In addition to the complex processing steps, in the 2D structure, the difficulty in this structure is to extend the depleted region below the p-type material. If the p-type material is directly superimposed on a n-type NW, and a gate deposited directly around the n-type NWs as shown in Fig. 2.12, the depleted region is directly below the p-type material when a tension is applied to the gate

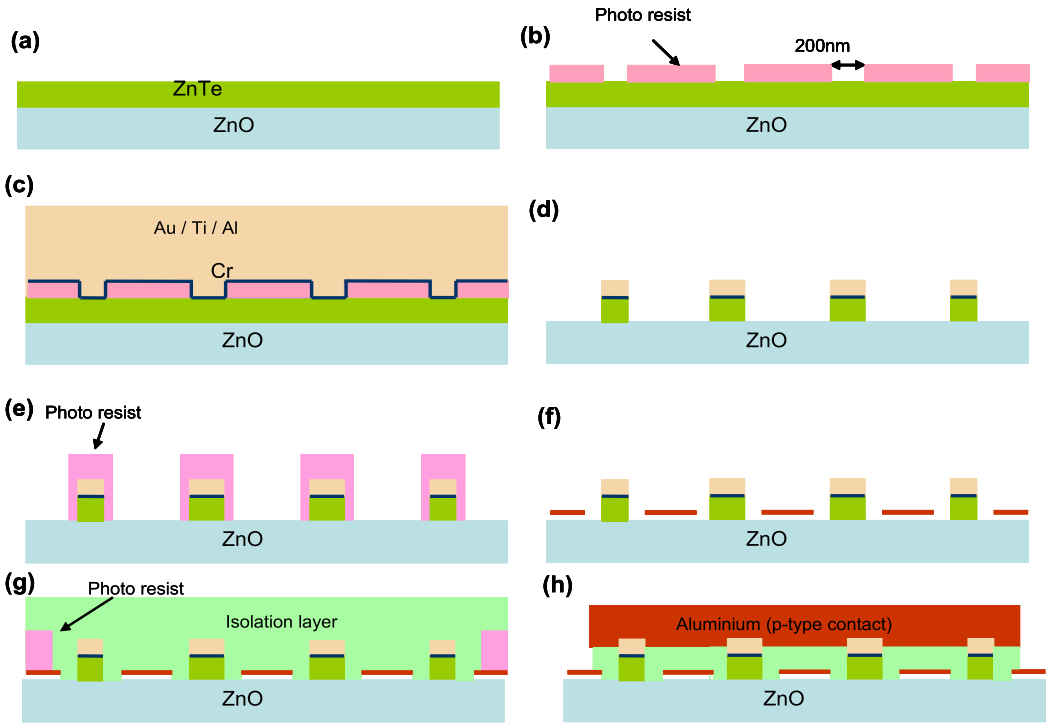

Figure 2.11: Process flow summary of a 2D hybrid junction processing. In this example the p-type material is ZnTe and the n-type material is ZnO. (a) 2D hybrid junction. (b) Photo resist deposition. (c) p-type contact deposition (d) lift-off and etching of the ZnTe layer. (e) photo resist deposition. (f) gate deposition and lift off (f) planarization with an isolation layer: spin on glass (SOG) and protection with a photo resist of some of the gate areas. (h) Aluminium deposition for the p-type contact, and lift-off to be able to take contacts on the gate.

(as shown in Fig.2.12(c)). This would increase the field effect hole injection in the NWs when applying a potential difference between the anode and the cathode.

Another interesting approach would also be to grow p-type NWs on top of a n-type template as shown in Fig. 2.13(a). A gate would be deposited between the NWs and a p-type contact could be taken on top of the NWs after planarization (as shown in Fig. 2.13(c)). This would avoid some lithography steps for the processing of a p-type layer. In addition, growing NWs could avoid strain relaxation in the p-type material through misfit dislocation formation. The fabrication of those structures entails the study of NWs growth on various type of substrates and the development of the proper processing. The Leti institute offers the perfect environment for the realization of this challenging project.

Several tasks will have to be tackled. The main ones are **the growth of p/n planar hybrid junctions, the NWs growth studies, the processing of the samples**

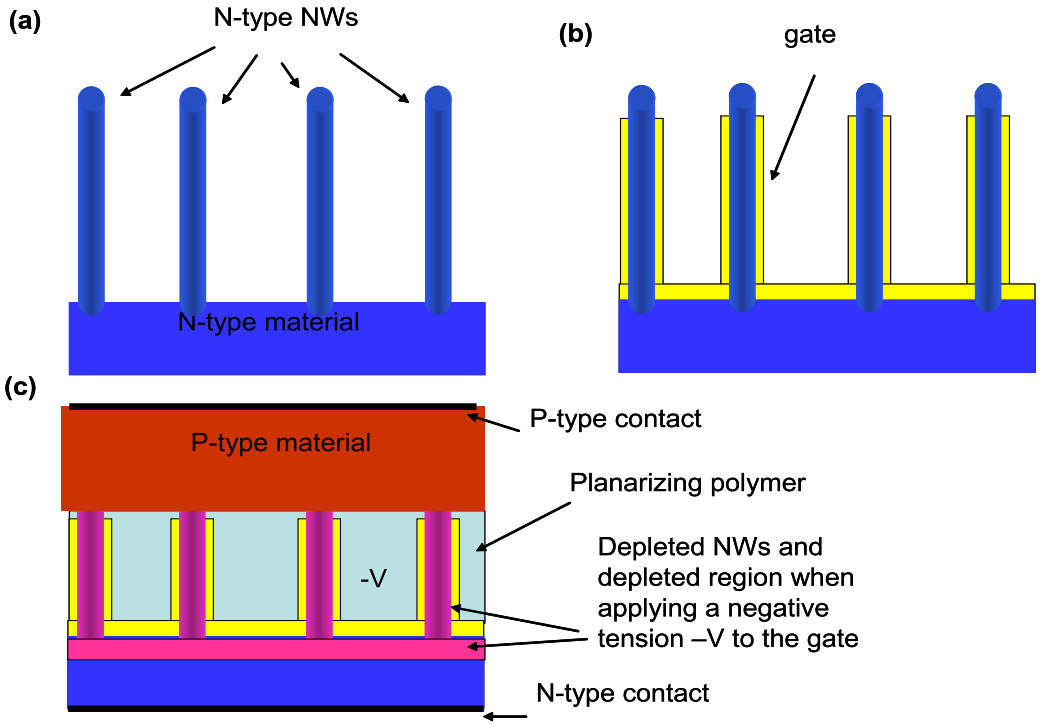

Figure 2.12: Field effect structure fabrication steps using n-type NWs. (a) Growth of the NWs. (b) Gate deposition (c) Planarization, p-type material over growth and contacts deposition.

2.2.3 Growth of p/n planar hybrid junctions

This is a challenging task as p-type materials will be grown on n-type materials of different nature. However the crystalline quality of the p-type material might not be crucial. The most important point is to obtain a highly doped p-type material. For the growth of those p/n hybrid junctions, (Al,Ga)N (Nitrides) and (Zn,Mg)O alloys will be used as n-type materials and ZnTe, ZnSe, GaN, NiO as p-type materials. The wide band-gap semiconductors chosen for the n-type materials feature a very strong excitonic binding energy (20meV and 60meV, respectively vs. 4.2meV in Arsenide-based compounds), therefore capable of sustaining excitonic emission at temperatures up to 300K. To begin with the growths will be performed on ZnO as ZnO substrates and 2-D templates are available. Those structures on ZnO will allow to prove the interest of field effect hole injection for solid state emission. Then, the growth of those p-type materials will be also studied on ZnMgO and AlGaN templates to go towards deeper UV emission. To obtain those templates I envisage collaborations with the GEMAC CNRS group in Meudon, the CRHEA CNRS group in Sophia Antipolis and the Bransweg University in Germany which are groups in Europe who are currently optimizing the growth of those materials. For the growth of p-type GaN on ZnO, there is a strong experience in ZnO and GaN growth at the laboratory. The growth of p-type GaN on ZnO is a new growth challenge that needs to be addressed. To realize p-type doping of GaN, oxygen diffusion from ZnO into GaN needs to be avoided and low

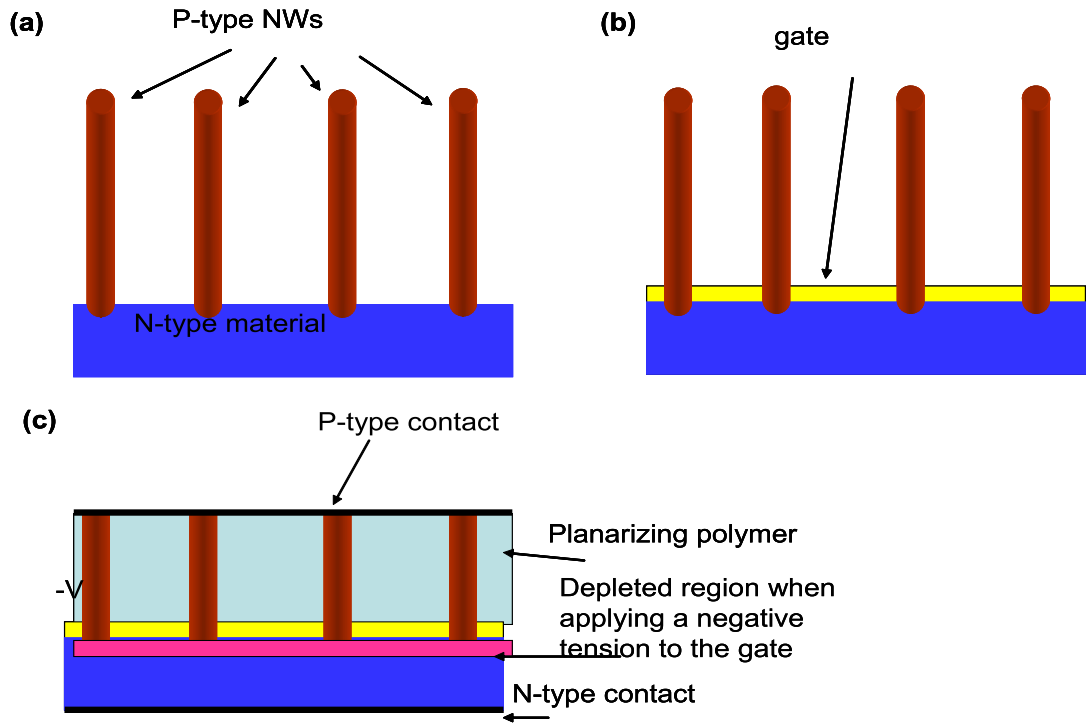

Figure 2.13: Field effect structure fabrication steps using p-type NWs. (a) Growth of the p-NWs on n-type material. (b) Gate deposition between the NWs (c) Planarization and contact deposition.

temperature growth needs to be performed. This will be done by MBE.

ZnTe and ZnSe MBE growth facility also exists at the INAC institute of CEA Grenoble. In particular efficient p-type doping of ZnTe can be achieved [135]. P-type ZnTe growth will be studied on ZnO. As ZnTe has a cubic lattice and ZnO an hexagonal one, the growth of ZnTe might be challenging. This approach could be very promising, as ZnO/ZnTe nanocone heterojuctions were already fabricated [137]. In addition, tellurium seems to favour p-type doping ZnO [139]. The growth and characterization of p-type ZnSe will also be performed using the same MBE machine. Indeed ZnSe is also a II-VI semiconductor and can be p-doped using nitrogen doping during MBE growth [140, 141]. In addition ZnSe has a larger band gap (of 2.7 eV at room temperature) than ZnTe which should favour hole injection into ZnO. NiO can also be grown at the CEA Grenoble by reactive pulverization. As said before, NiO is a p-type semiconductor with a large bandgap. Some group already fabricated p-NiO/n-ZnO hybrid junctions for LEDs applications [131]. Those junctions seems to be promising and could be used for field effect hole injection. A detail study of the NiO/ZnO growth and properties would be fruitfull, in particular, the study of the intermixing at the interface between the two oxides. To characterize the grown layers, Hall effect, time integrated and time resolved PL can be performed at the laboratory. I also plan to measure the ZnTe/ZnO, GaN/ZnO, NiO/ZnO valence band offsets by means of x-ray photoelectron spectroscopy (XPS).

2.2.4 NWs growth studies

As described in the first part of this manuscript, ZnO NWs were already grown at the laboratory and I already studied their optical properties [4, 142, 143]. To fabricate the structure described in figure 2.12, those NWs can be used. To go towards shorter wavelengths, the growth study of ZnMgO NWs will be needed.

ZnTe and ZnSe NWs were also already successfully grown at the INAC institute of CEA Grenoble [144]. The growth of those NWs is commonly done on GaAs, Si or ZnTe substrates. For the fabrication of the stucture of figure 2.13, the growth of those NWs on wide band gap semiconductors will have to be studied as well as the p-type doping of those NWs. If p-type NWs are grown on a n-type buffer, this would allow shortcutting a processing step which is etching a p-type 2D semiconductor layer.

2.2.5 Processing

The technology steps described in Fig. 2.11, Fig. 2.12 and 2.13 will have to be developed. In particular this will involve the study of etching steps for the fabrication of the 2D structure, the conformal deposition of a gate and the planarization for the fabrication of the NWs structures.

For the NWs processing, there is already a strong knowledge at the laboratory in the domain of NWs integration [145]. For gate deposition around the NWs, conformal oxide deposition can be achieved by chemical vapor deposition. Spin on Glass (SOG) can be used as filling material for planarization before taking the contacts on top of the NWs. Of course many studies need to be done for the control of those technological steps.

In this project each task corresponds to a specific research field in which major advances are required for the success of the project. During the project, the team will addresses major challenges using novel and unconventional steps and the success of the tasks will bring new opportunities for science in many different research fields. The LETI institute and the Optronic Department at the CEA Grenoble offer the perfect environment as many growth an characterization facilities are available. It can be seen that this project would give me the possibility to supervise several PhD students working on the different tasks.

Conclusion

During the beginning of my carrier I got the opportunity to work on a large variety of semiconductor materials ranging from very small band gap semiconductors for IR detectors to wide band gap semiconductors for UV emission. I tackled the growth and characterization aspects. I especially studied the correlation between the growth and post-growth treatments and the optical properties. Those studies will continued to take place for materials used in IR detectors and solar cells.

In parallel I will use the knowledge I gained in material systems to lead a challenging and completely new project to shortcut the problems linked to the p-type doping of wide bandgap semiconductors. This project based on field effect hole injection addresses a major challenge which is the fabrication efficient deep UV emitters.

Therefore I think I am now able to supervise PhD students who will work on the different projects I am planning to develop.

Bibliography

[1] I. C. Robin, R. andré, and J. M. Gérard. *Relation Between Growth Procedure and Confinement Properties of CdSe/ZnSe Quantum Dots*. Phys. Rev. B **74**, 155318 (2006).

[2] I. C. Robin, R. andré, A. Balocchi, S. Carayon, S. Moehl, J. M. Gérard, and L. Ferlazzo. *Purcell Effect for CdSe/ZnSe Quantum Dots Placed Into Hybrid Micropillars*. Appl. Phys. Lett. **87**, 233114 (2005).

[3] I. C. Robin, R. Kumaran, S. Penson, S. E. Webster, T. Tiedje, and A. Oleinik. *Structure and Photoluminescence of Nd:Y_2O_3 Grown By Molecular Beam Epitaxy*. Optical Materials **30**, 835 (2008).

[4] I. C. Robin, B. Gauron, P. Ferret, C. Tavares, G. Feuillet, Le Si Dang, B. Gayral, and J. M. Gérard. *Evidence For Low Density of Nonradiative Defects in ZnO Nanowires Grown By Metal Organic Vapor-phase Epitaxy*. Appl. Phys. Lett. **91**, 143120 (2007).

[5] I. C. Robin, M. Taupin, R. Derone, A. Solignac, P. Ballet, and A. Lusson. *Photoluminescence Studies of Arsenic-doped HgCdTe Epilayers*. Appl. Phys. Lett. **95**, 202104 (2009).

[6] F. Gemain, I. C. Robin, S. Brochen, M. D. Vita, and A. Lusson. *Identification of the Double Acceptor Levels of the Mercury Vacancies in HgCdTe*. Appl. Phys. Lett., to be published (2011).

[7] T. Aichele, V. Zwiller, O. Benson I. Akimov, and F. Henneberger. *Single CdSe Quantum Dots For High-bandwidth Single-photon Generation*. J. Opt. Soc. Am. B **20**, 2189 (2003).

[8] K. Sebald, P. Michler, T. Passow, D. Hommel, G. Bacher, and A. Forchel. *Single-photon Emission of CdSe Quantum Dots at Temperatures Up To 200 K*. Appl. Phys. Lett. **81**, 2920 (2002).

[9] H. Lohmeyer, C. Kruse K., Sebald, J. Gutowski, and D. Hommel. *Enhanced Spontaneous Emission of CdSe Quantum Dots in Monolithic II-VI Pillar Microcavities*. Appl. Phys. Lett. **89**, 091107 (2006).

[10] I. C. Robin, R. andré, H. Mariette, S. Tatarenko, L. Si Dang, J. M. Gérard, and E. Bellet Amalric. *New Method To Induce 2D-3D Transition of Strained CdSe/ZnSe Layers*. Physica E **26**, 119 (2005).

[11] I. C. Robin, R. andré, C. Bougerol, T. Aichele, and S. Tatarenko. *Elastic and Surface Energies: Two Key Parameters For CdSe Quantum Dot Formation*. Appl. Phys. Lett. **88**, 233103 (2006).

[12] I. C. Robin, T. Aichele, C. Bougerol, R. andré, S. Tatarenko, E. Bellet Amalric, B. VanDaele, and G. Van Tendeloo. *CdSe Quantum Dot Formation: Alternative Paths to Relaxation of a Strained CdSe Layer and Influence of the Capping Conditions*. Nanotechnology **18**, 265701 (2007).

[13] I. C. Robin, R. andré, A. Balocchi, S. Carayon, J. M. Gérard, K. Kheng, Le Si Dang, H. Mariette, S. Moehl, and F. Tinjod. *Purcell Effect on CdSe/ZnSe Quantum Dots Em Bedded in Pillar Microcavities*. physica Status Solidi (c) **2**, 3829 (2005).

[14] C. L. Bonner, C. T. A. Brown, D. P. Shepherd, W. A. Clarkson, A. C. Troper, D. C. Hanna, and B. Ferrand. *Diode-bar End-pumped High-power Nd:$Y_3Al_5O_{12}$ Planar Waveguide Laser*. Opt. Lett. **23**, 942 (1998).

[15] T. C. May Smith, C. Grivas, D. P. Shepherd, R. W. Eason, and M. J. F. Healy. *Thick Film Growth of High Optical Quality Low Loss (0.1 DB Cm^{-1}) Nd:$Gd_3Ga_5O_{12}$ on $Y_3Al_5O_{12}$ By Pulsed Laser Deposition*. Appl. Surf. Sci. **223**, 361 (2004).

[16] A. A. Kaminskii. *Modern Developments in the Physics of Crystalline Laser Materials*. Phys. Stat. Sol. A **200**, 215 (2003).

[17] P. H. Klein and W. J. Croft. *Thermal Conductivity, Diffusivity, and Expansion of Y_2O_3, $Y_3Al_5O_{12}$, and LaF_3 in the Range 77^o-300^oK*. J. Appl. Phys. **38**, 1603 (1967).

[18] K. T. J. Lu, J. Lu, T. Murai, K. Takaichi, T. Uematsu, K. I. Ueda, H. Yagi, T. Yanagitani, and A. A. Kaminskii. *Nd:Y_2o_3 Ceramic Laser*. Jpn. J. Appl. Phys. **40**, L1277 (2001).

[19] M. H. Cho, D. H. Ko, K. Jeong, S. W. Whangbo, C. Whang, S. Choi, and S. J. Cho. *Growth Stage of Crystalline Y_2O_3 Film on Si(100) Grown By An Ionized Cluster Beam Deposition*. J. Appl. Phys. **85**, 2909 (1999).

[20] A. Dimoulas, A. Travlos, G. Vellianitis, N. Boukos, and K. Argyropoulos. *Direct Heteroepitaxy of Crystalline Y_2O_3 on Si (001) For High-k Gate Dielectric Applications*. J. Appl. Phys. **90**, 4224 (2001).

[21] G. Apostolopoulos, G. Vellianitis, A. Dimoulas, M. Alexe, R. Scholz, M. Fanciulli, D. T. Dekadjevi, and C. Wiemer. *High Epitaxial Quality Y_2O_3 High-k Dielectric on Vicinal Si(001) Surfaces*. Appl. Phys. Lett. **81**, 3549 (2002).

[22] J. Kwo, M. Hong, A. R. Kortan, K. L. Queeney, Y. J. Chabal, J. R. L. Opila, D. A. Muller, S. N. G. Chu, B. J. Sapjeta, T. S. Lay, T. B. J. P. Mannaerts, H. W. Krautter, J. J. Krajewski, A. M. Sergnt, and J. M. Rosamilia. *Properties of High K Gate Dielectrics Gd_2O_3 and Y_2O_3 For Si*. J. Appl. Phys. **89**, 3920 (2001).

[23] B. M. Walsh, J. M. McMahon, W. C. Edwards, N. P. Barnes, R. W. Equall, and R. L. Hutcheson. *Spectroscopic Characterization of Nd:Y_2O_3: Application Toward a Differential Absorption Lidar System For Remote Sensing of Ozone*. J. Opt. Soc. Am. B **19**, 2893 (2002).

[24] H. G. Danielmeyer, M. Blatte, and P. Balmer. *Fluorescence Quenching in Nd:YAG*. Appl. Phys. A **1**, 269 (1973).

[25] V. Lupei, A. Lupei, S. Georgescu, T. Taira, Y. Sato, and I. Ikesue. *The Effect of Nd Concentration on the Spectroscopic and Emission Decay Properties of Highly Doped Nd:YAG Ceramics*. Phys. Rev. B **64**, 092102 (2001).

[26] R. KUMARAN, S. PENSON, I. C. ROBIN, T. TIEDJE, S. WEBSTER, and Z. A. FAOUYZI. *Methods of Making Optical Waveguide Structures By Way of Molecular Beam Epitaxy*. WO/2008/047240 (2008).

[27] R. Kumaran, S. E. Webster, S. Penson, Wei Li, and T. Tiedje. *Molecular Beam Epitaxy Growth of Neodymium-doped Yttrium Aluminum Perovskite*. Journal of Crystal Growth **311**, 2191 (2009).

[28] W. Li, S. E. Webster, R. Kumaran, S. Penson, and T. Tiedje. *Optical Wave Propagation in Epitaxial Nd:Y_2O_3 Planar Waveguides*. Journal of Crystal Growth **311**, 2191 (2009).

[29] S. E. Webster, R. Kumaran, S. Penson, and T. Tiedje. *Structural Analysis of Thin Epitaxial Y_2O_3 Films on Sapphire*. J. Vac. Sci. Technol. B **28**, 10.1116/1.3368608 (2010).

[30] C. Jagadish and S. J. Pearton. *Zinc Oxide Bulk, Thin Films and Nanostructures Processing, Properties and Applications*.

[31] T. Makino, C. H. Chia, N. T. Tuan, Y. Segawa, M. Kawasaki, A. Ohtomo, K. Tamura, and H. Koinumac. *Exciton Spectra of ZnO Epitaxial Layers on Lattice-Matched Substrates Grown With Laser-Molecular-Beam Epitaxy*. Appl. Phys. Lett. **76**, 3549 (2000).

[32] B. Xiang, P. Wang, X. Zhang, S. A. Dayeh, D. P. R. Aplin, C. Soci, D. Yu, and D. Wang. *Rational Synthesis of P-type Zinc Oxide Nanowire Arrays Using Simple Chemical Vapor Deposition*. Nano Lett. **7**, 323 (2007).

[33] W. Shan, W. Walukiewicz, K. M. Yu, Y. Zhang, S. S. Mao, R. Kling, C. Kirchner, and A. Waag. *Nature of Room-Temperature Photoluminescence in ZnO*. Appl. Phys. Lett. **86**, 153117 (2005).

[34] K. A. Jeon, H. J. Son, C. E. Kim, J. H. Kim, and S. Y. Lee. *Photoluminescence of ZnO Nanowires Grown on Sapphire (1 1 2) Substrates*. Physica E **37**, 222 (2007).

[35] P. C. Chang, C. J. Chien, D. Stichtenoth, C. Ronning, and J. G. Lu. *Finite Size Effect in ZnO Nanowires*. Appl. Phys. Lett. **90**, 113101 (2007).

[36] L. J. Wang and N. C. Giles. *Temperature Dependence of the Free-exciton Transition Energy in Zinc Oxide By Photoluminescence Excitation Spectroscopy*. J. Appl. Phys. **94**, 973 (2003).

[37] B. K. Meyer, H. Alves, D. M. Hofmann, W. Kriegseis, D. Forster, F. Bertram, J. Christen, A. Hoffmann, M. Strassburg, M. Dworzak, U. Haboeck, and A. V. Rodina. *Bound Exciton and Donor-Acceptor Pair Recombinations in ZnO*. Phys. Status Solidi B **241**, 227 (2004).

[38] C. Neumann, S. Lautenschlager, S. Graubner, J. Sann, N. Volbers, B. K. Meyer, J. Blasing, A. Krost, F. Bertram, and J. Christen. *Homoepitaxy of ZnO: From the Substrates to Doping*. Phys. Status Solidi B **244**, 1451 (2007).

[39] S. A. Studenikin and M. Cocivera. *Time-resolved Luminescence and Photoconductivity of Polycrystalline ZnO Films*. J. Appl. Phys. **91**, 5060 (2002).

[40] D. W. Hamby, D. A. Lucca, M. J. Klopstein, and G. Cantwell. *Temperature Dependent Exciton Photoluminescence of Bulk ZnO*. J. Appl. Phys. **93**, 3214 (2003).

[41] M. Gurioli, A. Vinattieri, M. Colocci, C. Deparis, J. Massies, G. Neu, A. Bosachi, and S. Franchi. *Temperature Dependance of the Radiative and Nonradiative Recombination Time in $GaAs/Al_xGa_{1-x}As$ Quantum-well Structures*. Phys. Rev. B **44**, 3115 (1991).

[42] K. Hazu, T. Sota, S. Adachi, S. Chichibu, G. Cantwell, D. C. Reynolds, and C. W. Litton. *Phonon Scattering of Excitons and Biexcitons in ZnO*. Appl. Phys. Lett. **96**, 1270 (2004).

[43] M. C. Jeong, B. Y. Oh, M. H. Ham, and J. M. Myoung. *Electroluminescence From ZnO Nanowires in N-ZnO Film/ZnO Nanowire Array/p-GaN Film Heterojunction Light-Emitting Diodes*. Appl. Phys. Lett. **88**, 202105 (2006).

[44] D. C. Kim, W. S. Han, B. H. Kong, H. K. Cho, and C. H. Hong. *Fabrication of the Hybrid ZnO LED Structure Grown on P-type GaN By Metal Organic Chemical Vapor Deposition*. Physica B **401-402**, 386 (2007).

[45] W. Gotz, N. M. Johnson, J. Walker, D. P. Bour, and R. A. Street. *Activation of Acceptors in Mg-doped GaN Grown By Metalorganic Chemical Vapor Deposition*. Appl. Phys. Lett. **68**, 667 (1996).

[46] H. J. Ko, Y. F. Chen, S. K. Hong, H. Wenisch, T. Yao, and D. C. Look. *Ga-doped ZnO Films Grown on GaN Templates By Plasma-assisted Molecular-beam Epitaxy*. Appl. Phys. Lett. **77**, 3761 (2000).

[47] D. W. Hamby, D. A. Lucca, M. J. Klopstein, and G. Cantwell. *Temperature Dependent Exciton Photoluminescence of Bulk ZnO*. J. Appl. Phys. **93**, 3214 (2003).

[48] I. C. Robin, A. Ribeaud, S. Brochen, G. Feuillet, P. Ferret, H. Mariette, D. Ehrentraut, and T. Fukuda. *Low Residual Doping Level in Homoepitaxially Grown ZnO Layers*. Appl. Phys. Lett. **92**, 141101 (2008).

[49] H. Von Wenckstern, H. Schmidt, M. Grundmann, M. W. Allen, P. Miller, R. J. Reeves, and S. M. Durbin. *Defects in Hydrothermally Grown Bulk ZnO*. Appl. Phys. Lett. **91**, 022913 (2007).

[50] A. B. M. A. Ashrafi, N. T. Binh, B. P. Zhang, and Y. Segawa. *Temperature-dependent Photoluminescence of ZnO Layers Grown on 6H-SiC Substrates*. J. Appl. Phys. **95**, 7738 (2004).

[51] H. C. Park, D. Byun, B. Angadi, D. Hee Park, W. K. Choi, J. W. Choi, and Y. S. Jung. *Photoluminescence of Ga-doped ZnO Film Grown on C-Al_2O_3 (0001) By Plasma-assisted Molecular Beam Epitaxy*. J. Appl. Phys. **102**, 073114 (2007).

[52] J. Simon, V. Protasenko, C. Lian, H. Xing, and D. Jena. *Polarization-Induced Hole Doping in Wide–Band-Gap Uniaxial Semiconductor Heterostructures*. Science **327**, 60 (2010).

[53] K. Vanheusden, C. H. Seager, W. L. Warren, D. R. Tallant, and J. A. Voigt. *Correlation Between Photoluminescence and Oxygen Vacancies in ZnO Phosphors*. Appl. Phys. Lett. **68**, 403 (1996).

[54] K. Vanheusden, C. H. Seager, W. L. Warren, D. R. Tallant, and J. A. Voigt. *ZnO Nanowire UV Photodetectors with High Internal Gain*. Nano Lett. **7**, 1003 (2007).

[55] D. Ehrentraut, Hideto Sato, Yuji Kagamitani, Hiroki Sato, Akira Yoshikawa, and Tsuguo Fukuda. *Solvothermal Growth of ZnO*. Prog. Cryst. Growth Charact. Mater. **52**, 280 (2006).

[56] S. Graubner, C. Neumann, N. Volbers, B. K. Meyer, J. Bläsing, and A. Krost. *Preparation of ZnO Substrates For Epitaxy: Structural, Surface, and Electrical Properties*. Appl. Phys. Lett. **90**, 042103 (2007).

[57] H. Xu, K. Ohtani, M. Yamao, , and H. Ohno. *Surface Morphologies of Homoepitaxial ZnO on Zn- and O-polar Substrates By Plasma Assisted Molecular Beam Epitaxy*. Appl. Phys. Lett. **89**, 071918 (2006).

[58] S. Heinze, A. Krtschil, J. Bläsing, T. Hempel, P. Veit, A. Dadgar, J. Christen, and A. Krost. *Homoepitaxial Growth of ZnO By Metalorganic Vapor Phase Epitaxy in Two-dimensional Growth Mode*. J. Cryst. Growth **308**, 170 (2007).

[59] I. S. Kim, S. H. Jeong, and B. T. Lee. *Growth and Characterization of High Quality Homoepitaxial ZnO Films By RF Magnetron Sputtering*. Semicond. Sci. Technol. **22**, 683 (2007).

[60] H. Von Wenckstern, H. Schmidt, C. Hanisch, M. Brandt, C. Czekalla, G. Benndorf, G. Biehne, A. Rahm, H. Hochmuth, M. Lorenz, and M. Grundmann. *Homoepitaxy of ZnO By Pulsed-laser Deposition*. Phys. Status Solidi (RRL) **1**, 129 (2007).

[61] R. Yakimova, G. R. Yazdi, N. T. Son, I. Ivanov, M. Syväjärvi, S. Sun, G. Tompa, A. Kuznetsov, and B. Svensson. *Optical and Morphological Features of Bulk and Homoepitaxial ZnO*. Superlattices Microstruct. **39**, 247 (2006).

[62] T. Koida, S. F. Chichibu, A. Uedono, A. Tsukazaki, M. Kawasaki, T. Sota, Y. Segawa, and H. Koinuma. *Correlation Between the Photoluminescence Lifetime and Defect Density in Bulk and Epitaxial ZnO*. Appl. Phys. Lett. **80**, 532 (2003).

[63] D. Ehrentraut, H. Sato, M. Miyamoto, T. Fukuda, M. Nikl, K. Maeda, and I. Niikura. *Fabrication of Homoepitaxial ZnO Films By Low-temperature Liquid-phase Epitaxy*. J. Cryst. Growth **287**, 367 (2006).

[64] A. Bakin, A. El Shaer, A. Che Mofor, M. Kreye, A. Waag, F. Bertram, J. Christen, M. Heuken, and J. Stoemenos. *MBE Growth of ZnO Layers on Sapphire Employing Hydrogen Peroxide As An Oxidant*. J. Cryst. Growth **287**, 7 (2006).

[65] B. Pécz, A. El Shaer, A. Bakin, A.-C. Mofor, A. Waag, and J. Stoemenos. *Structural Characterization of ZnO Films Grown By Molecular Beam Epitaxy on Sapphire With MgO Buffer*. J. Appl. Phys. **100**, 103506 (2006).

[66] F. Bertram, D. Forster, J. Christen, N. Oleynik, A. Dadgar, and A. Krost. *Direct Evidence For Selective Impurity Incorporation at the Crystal Domain Boundaries in Epitaxial ZnO Layers*. Appl. Phys. Lett. **85**, 1076 (2004).

[67] R. Sporken, S. Sivananthan, K. K. Mahavadi, G. Monfroy, M. Boukerche, and J. P. Faurie. *Molecular Beam Epitaxial Growth of CdTe and HgCdTe on Si (100)*. Appl. Phys. Lett. **55**, 1879 (1989).

[68] A. I. DSouza, L. C. Dawson, E. J. anderson, A. D. Markum, W. E. Tennant, L. O. Bubulac, M. Zandian, J. G. Pasko, W. V. McLevige, D. D. Edwall, J. W. Derr, and J. E. Jandik. *Molecular Beam Epitaxial Growth of CdTe and HgCdTe on Si (100)*. Journal of Electronic Materials **26**, 656 (1997).

[69] Y. Chang, C. R. Becker, C. H. Grein, J. Zhao, C. Fulk, T. Casselman, R. Kiran, X. J. Wang, E. Robinson, S. Y. An, S. Mallick, S. Sivananthan, T. Aoki, C. Z. Wang, D. J. Smith, S. Velicu, J. Zhao, J. Crocco, Y.Chen, G. Brill, P. S. Wijewarnasuriya, N. Dhar, R. Sporken, and V. Nathan. *Surface Morphology and Defect Formation Mechanisms For HgCdTe (211)b Grown By Molecular Beam Epitaxy*. Journal of Electronic Materials **37**, 1171 (2008).

[70] E. Selvig, C. R. Tonheim, T. Lorentzen, K. O. Kongshaug, T. Skauli, and R. Haakenaasen. *Defects in HgTe and CdHgTe Grown By Molecular Beam Epitaxy*. Journal of Electronic Materials **37**, 1444 (2008).

[71] J. P. Faurie and A. Million. *Molecular Beam Epitaxy of II–VI Compounds: CdHgTe*. J. Crystal Growth **54**, 582 (1981).

[72] J. Baylet, P. Ballet, P. Castelein, F. Rothan, O. Gravrand, M. Fendler, E. Lafosse, J. P. Zanatta, J. P. Chamonal, A. Million, and G. Destefanis. *TV/4 Dual-band HgCdTe Infrared Focal Plane Arrays With a 25-mm Pitch and Spatial Coherence*. J. Electron. Mater. **35**, 1153 (2006).

[73] H. F. Schaake, M. A. Kinch, D. Chandra, F. Aqariden, P. K. Liao, D. F. Weirauch, C. F. Wan, R. E. Scritchfield, W. W. Sullivan, J. T. Teherani, and H. D. Shih. *High-Operating-Temperature MWIR Detector Diodes*. J. Electron. Mater. **37**, 1401 (2008).

[74] J. Rothman, G. Perrays, P. Ballet, L. Mollard, S. Gout, and J. P. Chamonal. *Latest Developments of HgCdTe E-APDs at CEA LETI-Minatec*. J. Electron. Mater. **37**, 1303 (2008).

[75] J. D. Beck, C. F. Wan, M. A. Kinch, J. E. Robinson, P. Mitra, R. Scritchfield, F. Ma, and J. Campbell. *The HgCdTe Electron Avalanche Photodiode*. Proc. SPIE **5564**, 44 (2004).

[76] M. Zandian, A. C. Chen, D. D. Edwall, J. G. Pasko, and J. M. Arias. *p-type Arsenic Doping of HgCdTe By Molecular Beam Epitaxy*. Appl. Phys. Lett. **71**, 2815 (1997).

[77] A. C. Chen, M. Zandian, D. D. Edwall, R. E. De Wames, P. S. Wijewarnasuriya, J. M. Arias, S. Sivanathan, M. Berding, and A. Sher. *MBE Growth and Characterization of in Situ Arsenic Doped HgCdTe*. J. Electron. Mater. **27**, 595 (1998).

[78] M. A. Berding and A. Sher. *Amphoteric Behavior of Arsenic in HgCdTe*. Appl. Phys. Lett. **74**, 685 (1999).

[79] H. R. Vydyanath. *Amphoteric Behaviour of Group V Dopants in (Hg, Cd)Te*. Semicond. Sci. Technol. **5**, S213 (1990).

[80] H. F. Schaake. *On the Kinetics of the Activation of Arsenic As a P-type Dopant in $Hg_{1x}Cd_xTe$.*. J. Electron. Mater. **30**, 789 (2001).

[81] D. Chandra, H. F. Schaake, M. A. Kinch, F. Aguariden, C. F. Wan, D. F. Weirauch, and H. D. Shih. *Activation of Arsenic As An Acceptor in HgCdTe Under Equilibrium Conditions*. J. Electron. Mater. **31**, 715 (2002).

[82] D. Shaw. *The Incorporation and Diffusivity of As in $Hg_0,8Cd_0,2Te$*. Semicond. Sci. Technol. **15**, 911 (2000).

[83] F. Yue, J. Chu, J. Wu, Z. Hu, Y. Li, and P. Yang. *Modulated Photoluminescence of Shallow Levels in Arsenic-doped $Hg_{1-x}Cd_xTe$ ($x \approx 0.3$) Grown By Molecular Beam Epitaxy*. Appl. Phys. Lett. **92**, 121916 (2008).

[84] P. Ballet, B. Polge, X. Biquard, and I. Alliot. *Extended X-ray Absorption Fine Structure Investigation of Arsenic in HgCdTe: the Effect of the Activation Anneal*. J. Electron. Mater. **38**, 1726 (2009).

[85] I. Kenworthy, P. Capper, C. L. Jones, J. J. G. Gosney, and W. G. Coates. *Determination of Acceptor Ionisation Energies in CdHgTe*. Semicond. Sci. Technol. **5**, 854 (1990).

[86] Y. Selamet, C. H. Grein, T. S. Lee, and S. Sivananthan. *Electrical Properties of in Situ As Doped HgCdTe Epilayers Grown By Molecular Beam Epitaxy*. J. Vac. Sci. Technol. B **19**, 1488 (2001).

[87] R. Legros and R. Triboulet. *Photoluminescence of Cd-rich HgCdTe Alloys.*. J. Cryst. Growth **72**, 264 (1985).

[88] A. Lusson, F. Fuchs, and J. Y. Marfaing. *Systematic Photoluminescence Study of CdHgTe Alloys in a Wide Composition Range.*. J. Cryst. Growth **101**, 673 (1990).

[89] J. B. O. Gravrand, P. Ballet and N. Baier. *HgCdTe P-on-n Focal-Plane Array Fabrication Using Arsenic Incorporation During MBE Growth*. J. Elec. Mater. **38**, 1684 (2009).

[90] H. A. Vydyanath and C. H. Hiner. *Annealing Behavior of Undoped $Hg_{0.8}Cd_{0.2}Te$ Epitaxial Films at Low Temperatures*. J. Appl. Phys. **65**, 3080 (1989).

[91] H. R. Vydyanath. *Incorporation of Dopants and Native Defects in Bulk HgCdTe Crystals and Epitaxial Layers*. J. Cryst. Growth **161**, 64 (1996).

[92] A. T. Hunter and T. C. Mc Gill. *Luminescence From HgCdTe Alloys*. J. Appl. Phys. **52**, 5779 (1981).

[93] F. Yue, J. Chu, J. Wu, Z. Hu, Y. Li, and P. Yang. *Modulated Photoluminescence of Shallow Levels in Arsenic-doped HgCdTe Grown By Molecular Beam Epitaxy*. Appl. Phys. Lett. **92**, 121916 (2008).

[94] N. Dai, Y. Chang, X. G. Wang, B. Li, and J. H. Chu. *Photo-electronic Phenomena in Narrow Gap HgCdTe*. Cur. Appl. Phys. **2**, 365 (2002).

[95] E. Finkman and Y. Nemirovsky. *Electrical Properties of Shallow Levels in P-type HgCdTe*. J. Appl. Phys. **59**, 1205 (1986).

[96] W. Scott, E. L. Stelzer, and R. J. Hager. *Electrical and Far-infrared Optical Properties of P-type $Hg_{1-x}Cd_xTe$*. J. Appl. Phys. **47**, 1408 (1976).

[97] D. E. Cooper and W. A. Harrison. *Possible Negative-u Properties of the Cation Vacancy in Hgcdte*. J. Vac. Sci. Technol. A **8**, 1112 (1990).

[98] R. Fastow and Y. Nemirovsky. *The Excess Carrier Lifetime in P-type HgCdTe Measured By Photoconductive Decay*. J. Appl. Phys. **66**, 1705 (1989).

[99] X. Wu. *High-efficiency Polycrystalline CdTe Thin-film Solar Cells*. Sol. Energy **77**, 803 (2004).

[100] J. Aguilar Hernandez, J. Sastre Hernandez, N. Ximello Quiebras, R. Mendoza Perez, O. Vigil Galan, G. Contreras Puente, and M. Cardenas Garcya. *Photoluminescence Studies on CdS-CBD Films Grown By Using Different S/Cd Ratios*. Thin Solid Films **511 − 512**, 143 (2006).

[101] O. Vigil, I. Riech, M. Garcia Rocha, and O. Zelaya Angel. *Characterization of Defect Levels in Chemically Deposited CdS Films in the Cubic-to-hexagonal Phase Transition*. J. Vac. Sci. Technol. A **15**, 2282 (1997).

[102] . De Melo, L. Hernbdez, . Zelaya Angel, R. Lozada Morales, M. Becerril, and E. Vasco. *Low Resistivity Cubic Phase CdS Films By Chemical Bath Deposition*. Appl. Phys. Lett. **65**, 1278 (1994).

[103] K. Mochizuki, M. Satoh, and K. Igaki. *Orange Luminescence In CdS*. Jpn. J. Appl. Phys. **22**, 1414 (1983).

[104] K. S. Ramaiah, R. Pilkington, A. E. Hill, R. D. Tomlinson, and A. K. Bhatnagar. *Structural and Optical Investigations on Cds Thin Films Grown By Chemical Bath Technique*. Mater. Chem. Phys. **68**, 22 (2001).

[105] O. Brandt and K. H. Ploog. *The Benefit of Disorder*. Nat. Mater. **5**, 769 (2006).

[106] D. A. Steigerwald, J. C. Bhat, D. Collins, R. M. Fletcher, M. O. Holcomb, M. J. Ludowise, P. S. Martin, and S. L. Rudaz. *Illumination With Solid State Lighting Technology*. IEEE J. Sel. Top. Quantum Electron **8**, 310 (2002).

[107] Y. Taniyasu, M. Kasu, and T. Makimoto. *An Aluminium Nitride Light-Emitting Diode With a Wavelength of 210 Nanometres*. Nature **441**, 325 (2006).

[108] A. Khan, K. Balakrishnan, and T. Katona. *Ultraviolet Light-Emitting Diodes Based on Group Three Nitrides*. Nat. Photonics **2**, 77 (2008).

[109] S. Nakamura, N. Iwasa, M. Senoh, and T. Mukai. *Hole Compensation Mechanism of P-type GaN Films*. Jpn. J. Appl. Phys. **31**, 1258 (1992).

[110] P. Kozodoy, H. Xing, S. P. DenBaars, U. K. Mishra, A. Saxler, R. Perrin, S. Elhamri, and W. C. Mitchel. *Heavy Doping Effects in Mg-doped GaN*. J. Appl. Phys. **87**, 1832 (2000).

[111] D. P. Norton, Y. W. Heo, M. P. Ivill, K. Ip, S. J. Pearton, M. F. Chisholm, and T. Steiner. *ZnO: Growth, Doping and Processing*. Materials Today **7**, 34 (2004).

[112] S. Choopun, R. D. Vispute, W. Yang, R. P. Sharma, T. Venkatesan, and H. Shen. *Realization of Band Gap Above 5.0 Ev in Metastable Cubic-phase $Mg_xZn_{1-x}O$ Alloy Films*. Appl. Phys. Lett. **80**, 1529 (2002).

[113] W. Yang, R. D. Vispute, S. Choopun, R. P. Sharma, T. Venkatesana, and H. Shen. *Ultraviolet Photoconductive Detector Based on Epitaxial $Mg_{0.34}Zn_{0.66}O$ Thin Films*. Appl. Phys. Lett. **78**, 2787 (2001).

[114] D. C. Look, G. M. Renlund, R. H. Burgener, and J. R. Sizelove. *As-doped P-type ZnO Produced By An Evaporation/sputtering Process*. Appl. Phys. Lett. **85**, 5269 (2004).

[115] A. B. M. A. Ashrafi, I. Suemune, H. Kumano, and S. Tanaka. *Nitrogen-doped P-type ZnO Layers Prepared With H_2O Vapor-assisted Metalorganic Molecular-beam Epitaxy*. Jpn. J. Appl. Phys. **41**, L1281 (2002).

[116] A. V. Singh, R. M. Mehra, A. Wakahara, and A. Yoshida. *p-type Conduction in Codoped ZnO Thin Films*. J. Appl. Phys. **93**, 396 (2003).

[117] T. M. Barnes, K. Olson, and C. A. Woldena. *On the Formation and Stability of P-type Conductivity in Nitrogen-doped Zinc Oxide*. Appl. Phys. Lett. **86**, 112112 (2005).

[118] A. Tsukazaki, A. Ohtomo, T. Onuma, M. Ohtani, T. Makino, M. Sumiya, K. Ohtani, S. F. Chichibu, S. Fuke, Y. Segawa, H. Ohno, H. Koinuma, and M. Kawasaki. *Repeated Temperature Modulation Epitaxy For P-type Doping and Light-Emitting Diode Based on ZnO*. Nat. Mater. **4**, 42 (2005).

[119] Y. R. Ryu, T. S. Lee, J. A. Lubguban, A. B. Corman, H. W. White, J. H. Leem, M. S. Han, Y. S. Park, C. J. Youn, and W. J. Kim. *Wide-band Gap Oxide Alloy: BeZnO*. Appl. Phys. Lett. **88**, 052103 (2006).

[120] J. H. Lim, C. K. Kang, K. K. Kim, I. K. Park, D. K. Hwang, and S. J. Park. *UV Electroluminescence Emission From ZnO Light-Emitting Diodes Grown By High-temperature Radiofrequency Sputtering*. Adv. Mater. **18**, 2720 (2006).

[121] S. J. Jiao, Z. Z. Zhang, Y. M. Lu, D. Z. Shen, B. Yao, J. Y. Zhang, B. H. Li, D. X. Zhao, X. W. Fan, and Z. K. Tang. *ZnO p-n Junction Light-Emitting Diodes Fabricated on Sapphire Substrates*. Appl. Phys. Lett. **88**, 031911 (2006).

[122] K. Ip, Y. W. Heo, D. P. Norton, , S. J. Peartona, J. R. LaRoche, and F. Ren. *$Zn_{0.9}Mg_{0.1O}$/ZnO p–n Junctions Grown By Pulsed-laser Deposition*. Appl. Phys. Lett. **85**, 1169 (2004).

[123] G. E. Pike, S. R. Kurtz, P. L. Gourley, H. R. Philipp, and L. M. Levinson. *Electroluminescence in ZnO Varistors: Evidence For Hore Contributions to the Breakdown Mechanism*. J. Appl. Phys. **57**, 5512 (1985).

[124] D. J. Rogers, F. H.Teherani, A. Yasan, K. Minder, P. Kung, and M. Razeghi. *Electroluminescence at 375 Nm From a ZnO/GaN:Mg/c-Al_2O_3 Heterojunction Light Emitting Diode*. Appl. Phys. Lett. **88**, 141918 (2006).

[125] Y. I. Alivov, J. E. Van Nostrand, D. C. Look, M. V. Chukichev, and B. M. Ataev. *Observation of 430 Nm Electroluminescence From ZnO/GaN Heterojunction Light-Emitting Diodes*. Appl. Phys. Lett. **83**, 2943 (2003).

[126] A. Bakin, A. Behrends, A. Waag, H. J. Lugauer, A. Laubsch, and K. Streubel. *ZnO GaN Hybrid Heterostructures As Potential Cost-Efficient LED Technology*. Proceedings of the IEEE **98**, 1281 (2010).

[127] K. A. Bulashevich, I. Y. Evstratov, and S. Y. Karpov. *Hybrid ZnO/III-nitride Light-Emitting Diodes: Modelling Analysis of Operation*. Phys. Status. Solidi (a) **204**, 241 (2007).

[128] X. M. Zhang, M. Y. Lu, Y. Zhang, L. Chen, and Z. L. Wang. *Fabrication of a High-Brightness Blue-Light-Emitting Diode Using a ZnO-Nanowire Array Grown on P-GaN Thin Film*. Adv. Mater. **21**, 2767 (2009).

[129] K. K. Kim, S. D. Lee, H. Kim, J. C. Park, S. N. Lee, Y. Park, S. J. Park, and S. W. Kim. *Enhanced Light Extraction Efficiency of GaN-based Light-Emitting Diodes With ZnO Nanorod Arrays Grown Using Aqueous Solution*. Appl. Phys. Lett. **94**, 071118 (2009).

[130] H. Ohta, M. Hirano, K. Nakahara, H. Maruta, T. Tanabe, M. Kamiya, T. Kamiya, and H. Hosono. *Fabrication and Photoresponse of a p-n-heterojunction Diode Composed of Transparent Oxide Semiconductors, P-NiO and N-ZnO*. Appl. Phys. Lett. **83**, 1029 (2003).

[131] Y. Y. Xi, Y. F. Hsu, A. B. Djurišic, A. M. C. Ng, W. K. Chan, H. L. Tam, and K. W. Cheah. *NiO/ZnO Light Emitting Diodes By Solution-based Growth*. Appl. Phys. Lett. **92**, 113505 (2008).

[132] Y. Vygranenko, K. Wang, and A. Nathan. *Low Leakage p-NiO/ I-ZnO/n-ITO Heterostructure Ultraviolet Sensor*. Appl. Phys. Lett. **89**, 172105 (2006).

[133] J. Y. Wang, C. Y. Lee, Y. T. Chen, C. T. Chen, Y. L. Chen, C. F. Lin, and Y. F. Chen. *Double Side Electroluminescence From P-NiO/n-ZnO Nanowire Heterojunctions*. Appl. Phys. Lett. **95**, 131117 (2009).

[134] C. L. Kuo, R. C. Wang, J. L. Huang, C. P. Liu, C. K. Wang, S. P. Chang, W. H. Chu, C. H. Wang, and C. H. Tu. *The Synthesis and Electrical Characterization of Cu2O/Al:ZnO Radial p–n Junction Nanowire Arrays*. Nanotechnology **20**, 365609 (2009).

[135] T. Baron, K. Saminadayar, and N. Magnea. *Nitrogen Doping of Te-based II–VI Compounds During Growth By Molecular Beam Epitaxy*. J. Appl. Phys. **83**, 1354 (1998).

[136] A. Sher R. D. Feldman, R. F. Austin, R. L. Opila, R. L. Masaitis, J. L. Zyskind, and J. W. Sulhoff. *Fabrication of N-Native Oxide/p-ZnTe Heterojunctions the Anodic Oxidation of ZnTe MBE Layers*. J. Electron. Mater. **21**, 653 (1992).

[137] S. H. Lee, X. G. Zhang, B. Smith, S. S. A. Seo, Z. W. Bell, and Jun Xu. *ZnO–ZnTe Nanocone Heterojunctions*. Appl. Phys. Lett. **96**, 193116 (2010).

[138] S. K. Hong, T. Hanada, H. Makino, Y. Chen, H. J. Ko, T. Yao, A. Tanaka, H. Sasaki, and Shigeru Sato. *Band Alignment at a ZnO/GaN (0001) Heterointerface*. Appl. Phys. Lett. **78**, 3349 (2001).

[139] S. K. Hong, T. Hanada, H. Makino, Y. Chen, H. J. Ko, T. Yao, A. Tanaka, H. Sasaki, and Shigeru Sato. *Tellurium Assisted Realization of P-type N-doped ZnO*. Appl. Phys. Lett. **96**, 242101 (2010).

[140] R. M. Park, M. Troffer, C. M. Rouleau, J. M. DePuydt, and M. A. Haase. *p-type ZnSe By Nitrogen Atom Beam Doping During Molecular Beam Epitaxial Growth*. Appl. Phys. Lett. **57**, 2127 (1990).

[141] J. Qiu, J. M. DePuydt, H. Cheng, and M. A. Haase. *Heavily Doped P-ZnSe:N Grown By Molecular Beam Epitaxy*. Appl. Phys. Lett. **59**, 2992 (1991).

[142] I. C. Robin, P. Marotel, A. H. El Shaer, V. Petukhov, A. Bakin, A. Waag, M. Lafossas, J. Garcia, M. Rosina, A. Ribeaud, S. Brochen, P. Ferret, and G. Feuillet. *Compared Optical Properties of ZnO Heteroepitaxial, Homoepitaxial 2D Layers and Nanowires*. Journal of Crystal Growth **311**, 2172 (2009).

[143] I. C. Robin, M. Lafossas, J. Garcia, M. Rosina, E. Latu Romain, P. Ferret, P. Gilet, A. Tchelnokov, M. Azize, J. Eymery, and G. Feuillet. *Growth and Characterization of ZnO Nanowires on P-type GaN*. Microelectron. J. **40**, 250 (2009).

[144] E. Bellet Amalric, M. Elouneg Jamroz, C. Bougerol, M. Den Hertog, Y. Genuist, S. Bounouar, J. P. Poizat, K. Kheng, R. andré, and S. Tatarenko. *Epitaxial Growth of ZnSe and ZnSe/CdSe Nanowires on ZnSe*. Phys. Status. Solidi (c). **7**, 1526 (2010).

[145] E. Latu Romain, P. Gilet, P. Noel, J. Garcia, P. Ferret, M. Rosina, G. Feuillet, F. Lévy, and A. Chelnokov. *A Generic Approach For Vertical Integration of Nanowires*. Nanotechnlogy **19**, 345304 (2008).